2013

Recent Advances in Vapor Chamber Transport Characterization for High Heat Flux Applications

J. A. Weibel
Purdue University, jaweibel@purdue.edu

S V. Garimella
Purdue University, sureshg@purdue.edu

Weibel, J. A. and Garimella, S V., "Recent Advances in Vapor Chamber Transport Characterization for High Heat Flux Applications" (2013). *CTRC Research Publications.* Paper 228.
http://dx.doi.org/http://dx.doi.org/10.1016/B978-0-12-407819-2.00004-9

Recent Advances in Vapor Chamber Transport Characterization for High Heat Flux Applications

Justin A. Weibel and Suresh V. Garimella[§]

Cooling Technologies Research Center, an NSF IUCRC

School of Mechanical Engineering and Birck Nanotechnology Center

Purdue University

West Lafayette, IN 47907-2088 USA

Abstract

Owing to their high reliability, simplicity of manufacture, passive operation, and effective heat transport, flat heat pipes and vapor chambers are used extensively in the thermal management of electronic devices. The need for concurrent size, weight, and performance improvements in high-performance electronics systems, without resort to active liquid-cooling strategies, demands passive heat spreading technologies that can dissipate extremely high heat fluxes from small hot spots. In response to these daunting application-driven trends, a number of recent investigations have focused on the design, characterization, and fabrication of ultra-thin vapor chambers for proximate heat spreading away from these hot spots. The predominant transport mechanisms and operational limits have been found to be different under these conditions relative to conventional low-power heat pipes. Noteworthy advances in the fundamental understanding of evaporation and boiling from porous microstructures fed by capillary action, and improvements in vapor chamber characterization, modeling, design, and fabrication techniques are reviewed. Characterization of evaporation and boiling from idealized and realistic wick structures, observation of vapor formation regimes as a function of operating conditions, assessment of fluid dryout limitations, design of novel multi-scale and nanostructured wicks for enhanced transport, and incorporation of these high heat flux transport phenomena into device-level models are discussed. These recent developments have successfully extended the maximum operating heat flux limits of vapor chambers.

[§] Corresponding author: email: sureshg@purdue.edu; Telephone: (+1) 765-494-5621

Keywords

Flat heat pipe, ultra-thin vapor chamber, thermal ground plane, electronics cooling, porous media, nanostructured wick, evaporation, boiling incipience, capillary dryout

1 Introduction

The high effective thermal conductance offered by heat pipes and other passively driven multiphase fluid loop heat transport devices has spurred their utilization across a range of thermal management applications for purposes of heat conveying and spreading, temperature control and equalization, and energy harvesting and storage. The advantageous device heat transport characteristics in all such applications stem from the thermodynamic cycle of vaporization and condensation of an enclosed working fluid that serves as the primary energy carrier.

Such devices are evacuated and charged with an internal working fluid as part of the assembly process. During operation, the working fluid is vaporized via evaporation at the location of heat input, which results in a local increase in the vapor pressure. The elevated internal pressure forces vapor to travel toward the condenser region where heat is rejected via condensation. By taking advantage of the highly effective phase-change heat transfer across the liquid-vapor interfaces, this heat transport process can occur under near-isothermal conditions at a small saturation pressure gradient. Continuous cyclical operation is passively achieved since the condensed liquid is returned to the heat input section by capillary action in a porous wick material that connects the vaporization and condensation interfaces, by gravity, or by other means. The capillary pressure generated by the pores of a wick material must overcome the cumulative viscous and inertial pressure drops along the vapor and liquid flow paths to sustain operation at any given heat transport rate. When this condition and several other operating limits are satisfied, such as avoiding entrainment of liquid into the vapor flow and choking at sonic vapor velocities, order-of-magnitude gains in overall effective thermal conductance can be realized compared to solid heat spreading materials of the same shape.

The term thermosyphon typically refers to devices where the liquid return occurs by gravity, while the term heat pipe is used to refer to other liquid-return schemes. The most common heat pipe configuration is a sealed cylindrical tube with axial capillary grooves or porous wick material lining the inner wall, and is intended for bulk transport of heat along the device length. A wide variety of non-conventional heat pipe types have been developed due to the need for different operational characteristics and form factors. Examples including variable conductance gas-loaded heat pipes for constant temperature control, capillary pumped loops for wickless transport over long working distances, rotating heat pipes in which liquid return occurs by centrifugal force, micro heat pipes, thermal diodes, oscillating heat pipes, and others are described in detail in [1-4]. Recent reviews summarize research on emerging heat pipe applications [5,6], novel working fluid developments [7], advances in modeling approaches [8,9], and

performance of archetypal device geometries, such as loop heat pipes [10,11], micro heat pipes [12], and oscillating heat pipes [13]. A comprehensive summary of all such device types, applications, and analysis methodologies is outside the scope of the current review; instead, the focus is on the burgeoning interest and developments in heat pipes targeted at spreading of very high heat fluxes in ultra-thin form factors, as discussed in the following section

1.1 Ultra-Thin Vapor Chambers for Thermal Management of Electronics

The most widespread application of heat pipes is in the thermal management of electronics. Heat pipes for this application are typically mass produced for integration into consumer devices such that heat may be dissipated efficiently from integrated circuits that must be kept below specified temperature limits. In most conventional low-power configurations, the primary purpose is efficient transport of heat to a remote location where a larger, more effective heat sink can be accommodated, resulting in a net reduction of junction-to-ambient thermal resistance.; however, the need for concurrent size, weight, and performance improvement in high-performance commercial and military electronics over the last decade has given rise to an increasing number of thermally limited systems which demand low thermal resistance ultra-thin heat spreaders (< 1 mm thick) that can dissipate extremely high heat fluxes (> 500 W/cm^2) from small areas (< 1 cm^2). The thermal packaging infrastructure of electronics systems such as radar power amplifiers, engine digital control systems, and high-performance graphics processing units requires passive heat removal directly from microelectronic devices, typically achieved by die attach to moderate-conductivity copper alloy substrates. Their proven reliability, hermetic packaging, passive operation, and high effective conductance offer heat pipe devices as a potential solution for these applications.

A vapor chamber is a flat heat pipe with rectangular cross-section employed for heat spreading (Figure 1). While flat heat pipes have long been utilized in electronics cooling applications, and are often produced simply by pressing a cylindrical heat pipe into a flat shape, the development of ultra-thin vapor chambers for high heat flux applications requires a paradigm shift in terms of the transport mechanisms coming into play at this different form factor. In relative terms, conventional heat pipes are thicker devices intended to transport heat over longer working distances from larger, lower heat flux sources. This mode of operation results in low surface superheat temperatures, and evaporation occurs from a continually receding meniscus up to the capillary limited heat input level. The dominant system thermal resistance is conduction between the external surfaces and the liquid-vapor interfaces [14]; figures of merit for working fluid selection (see Merit Number in [4]) are established based on this capillary operating limit. Conversely, ultra-thin vapor chamber heat spreaders have a comparatively small working length and total input

power, albeit at a high local heat flux. Therefore, a capillary limit is not expected to be encountered until the total heat input gives rise to an extremely high local heat flux, large surface superheat, and potential incipience of boiling in the wick structure. Accurate quantification of the pressure drop in the vapor space at ultra-thin form factors and the temperature differential associated with internal phase-change processes at high heat fluxes is necessary for prediction of overall device thermal resistance.

[Insert Fig1.tif here full-page width]

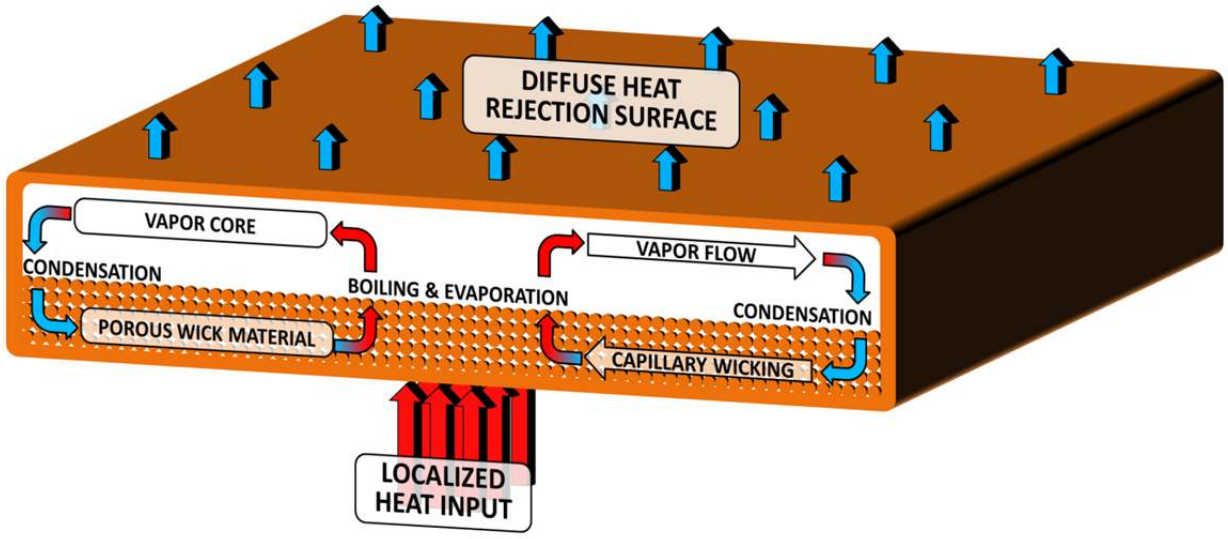

Figure 1. Schematic diagram of the operation and form factor of a flat heat pipe or vapor chamber heat spreader (scale in the thickness direction magnified to show details of operation).

1.2 Nucleate Boiling in Porous Wick Structures

Conventional wisdom calls for nucleate boiling to be avoided in heat pipes having longitudinal groove wick structures. In these wicks, nucleation of vapor bubbles completely obstructs the non-communicating individual paths of capillary liquid return to the evaporator section; a boiling limit is imposed in this case based on the conventional nucleation incipience superheat criterion. Alternatively, sintered screen mesh, sintered powder, and fibrous wick structures affixed to the wall of a heat pipe can continue to feed liquid to the heat source during boiling via the inherently stochastic network of interconnected pores. While it is commonly accepted that these structures may support nucleate boiling, conventional heat pipe applications discussed in Section 1.1 have not necessitated comprehensive assessment of the boiling behavior from wick structures during heat pipe operation. The recent development of ultra-thin vapor chambers for high heat flux dissipation has altered this perspective.

Submerged pool boiling from porous surfaces has been extensively characterized for a number of surface geometries, working fluids, and flooded porous wick structures often found in heat pipes [15-28]. The fundamental mechanism of heat transfer during boiling from a porous surface submerged in a liquid pool differs from that from a wick that is passively fed by capillary action. The schematic diagram in Figure 2 illustrates the primary differences in heat transfer regimes between capillary-fed and pool boiling. In pool boiling, heat transport initially occurs by natural convection at low heat fluxes, and is followed by nucleate boiling until the critical heat flux (CHF) is reached. In contrast, a liquid-vapor free surface exists at the top layer of the liquid-saturated porous structure in a heat pipe, and heat transport first occurs in an evaporation regime prior to boiling incipience. Also, during capillary-fed boiling, the liquid-vapor free surface boundary in the pore layer causes drastic differences in the bubble departure characteristics. The observed heat transfer regimes (*e.g.*, natural convection versus evaporation at low heat fluxes), vapor formation characteristics, and transition criteria for incipience/dryout are all different under capillary-feeding conditions, and require targeted investigation under representative conditions that is different from pool boiling.

[Insert Fig2.tif here 3/4-page width]

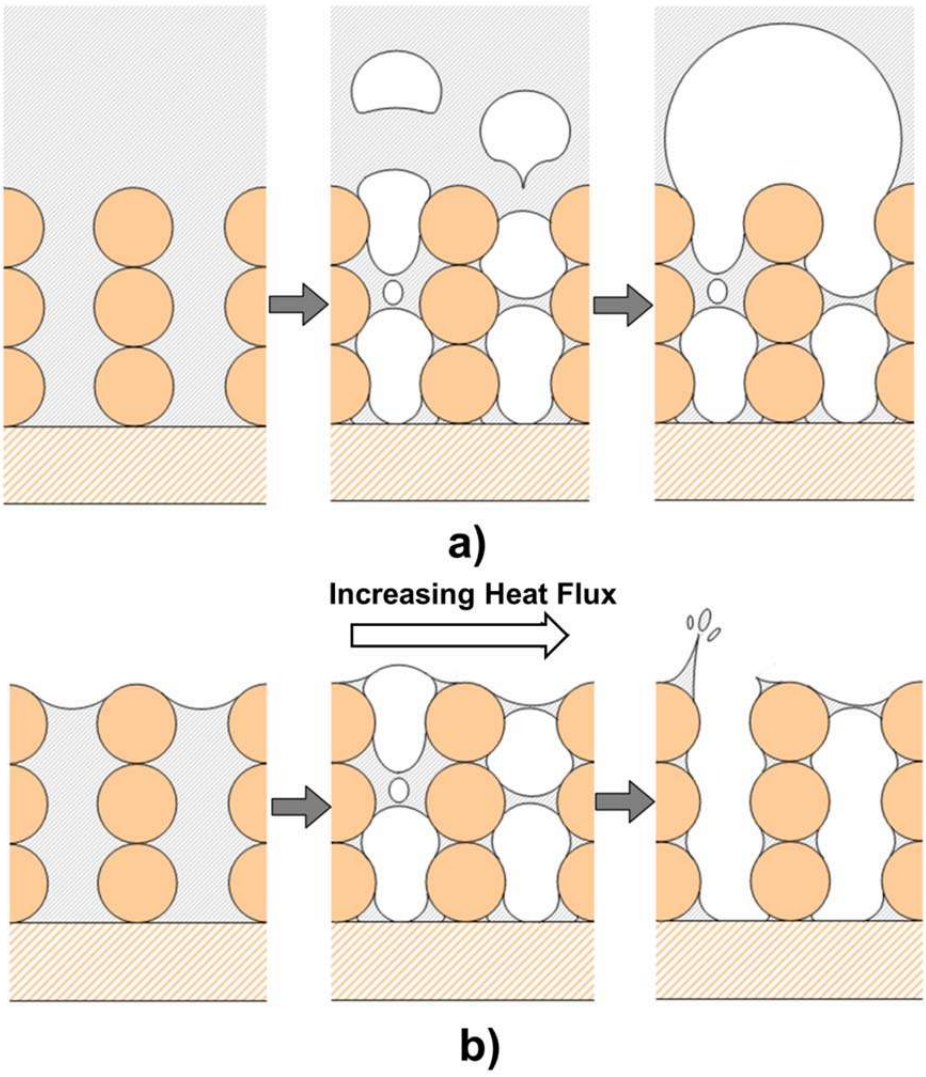

Figure 2. Schematic representation of the vapor formation characteristics for (a) submerged pool boiling, and (b) capillary-fed boiling conditions.

1.3 Recent Advances

In response to the application-driven demands on vapor chamber design and functionality, a number of recent studies have developed testing and analysis capabilities intended specifically for investigation of capillary-fed evaporation and boiling phenomena for a variety of porous wick structures. Recent experimental investigations that isolate the capillary-fed evaporation/boiling process for dedicated characterization are presented in Table 1.

Recent advances in the experimental investigation and analysis of ultra-thin vapor chambers for high heat flux applications are reviewed in this Chapter. The discussion focuses on:

1. Observation of capillary-fed boiling regimes, visualization of vapor formation characteristics, and parametric performance quantification of vapor chamber wick structures subjected to high heat fluxes (Section 2.1)

2. Development and fabrication of novel heterogeneously structured and patterned vapor chamber wicks for reduced capillary-fed boiling thermal resistance (Section 2.2)

3. Prediction of heat transfer coefficients, exploration of incipience transition criteria, and assessment of heat input area dependencies of dryout mechanisms for capillary-fed boiling (Section 2.3-2.5)

4. Vapor chamber modeling developments, *viz.* wick microstructure characterization and methodologies for incorporation into device-level models, implementation of boiling in models at high heat fluxes, and optimization for ultra-thin form factors (Section 3.1-3.3)

5. Comparison of capillary-fed boiling experiments to, and validation of transport models against, ultra-thin vapor chamber device-level tests (Section 3.4)

6. Analytical and experimental assessment of nanostructures for improved capillary wicking/wetting behavior and enhancement of capillary-fed evaporation/boiling (Section 4)

Table 1. Summary of recent experimental investigations on capillary-fed evaporation/boiling.

Homogeneous Wick Structures					
Authors	**Wick Structure**	**Wick Thickness**	**Test Fluid**	**Heat Source Details**	**Maximum Heat Flux**
Brautsch, Kew, 2002 [29]	Clamped 304L Stainless Steel Screen Mesh Wire Dia. 40-190 μm Porosity 0.313-.469	1-5 Layers	Water (T_{sat} = 100 °C)	Variable Area (not reported) Vertical Rise Height 55-79 mm	8.24-21.39 W/cm^2
Hanlon, Ma, 2003 [30]	Monoporous Sintered Copper Powder Particle Dia. 635 μm Porosity 0.43	1.9-5.7 mm	Water (T_{sat} = 100 °C)	10 × 20 mm^2 Horizontal	~35-55 W/cm^2
Davis, Garimella, 2008 [31]	Monoporous Sintered Copper Powder Particle Dia. 45-355 μm Porosity 0.46-0.60	1 mm	Water (T_{sat} = 47-52 °C)	384 mm^2 Horizontal	~30-33 W/cm^2
Li, Peterson, Wang, 2006 [32]	Sintered Copper Screen Mesh Wire Dia. 56 μm Porosity 0.693-0.737	0.21-0.74 mm	Water (T_{sat} = 100 °C)	8 × 8 mm^2 Horizontal	150-367.9 W/cm^2
Li, Peterson, 2006 [33]	Sintered Copper Screen Mesh Wire Dia. 56-191 μm Pore Size 119.3-232.8 μm Porosity 0.409-0.692	0.37 mm	Water (T_{sat} = 100 °C)	8 × 8 mm^2 Horizontal	150-367.9 W/cm^2
North, Rosenfeld,	Biporous Sintered Copper Powder	0.64 mm	Water (T_{sat} = 20 °C)	30 × 8 mm^2 Horizontal	27-70 W/cm^2

Shaubach, 1995 [34]	Particle Dia. 66-89 μm Cluster Dia. 250-710 μm Porosity ~0.70				
Semenic, Lin, Catton, Sarraf, 2008 [35]	Monoporous Sintered Copper Powder Particle Dia. 53-710 μm Porosity 0.318-0.371	1 mm	Water (T_{sat} = 40-48 °C)	70.9 mm^2 Horizontal	209.5-223 W/cm^2
Semenic, Lin, Catton, Sarraf, 2008 [35]	Biporous Sintered Copper Powder Particle Dia. 29-63 μm Cluster Dia. 250-710 μm Porosity 0.597-0.631	1-4 mm	Water (T_{sat} = 40-48 °C for 1 mm thick)	70.9 mm^2 Horizontal	150-494 W/cm^2
Semenic, Catton, 2009 [36]	Biporous Sintered Copper Powder Particle Dia. 41-83 μm Cluster Dia. 302-892 μm Porosity 0.51-0.68	0.8-3 mm	Water (T_{sat} = 36-46 °C)	32.2 mm^2 Horizontal	244-990 W/cm^2
Weibel, Garimella, North, 2010 [37]	Monoporous Sintered Copper Powder Particle Dia. 60-302.5 μm Porosity 0.635-0.657	0.6-1.2 mm	Water (T_{sat} = 100 °C)	5 × 5 mm^2 Vertical Rise Height 8.25 mm	500-596.5 W/cm^2
Weibel, 2012 [38]	Monoporous Sintered Copper Powder Particle Dia. 100 μm Porosity 0.5	0.2 mm	Water (T_{sat} = 100 °C)	25-100 mm^2 Vertical Rise Height 8.25 mm	160-430 W/cm^2

Heterogeneous and Patterned Wick Structures

Authors	Wick Structure	Wick Thickness	Test Fluid	Heater Details	Maximum Heat Flux
Zhao, Chen, 2006 [39]	Sintered Copper Powder with Vertical Microgrooves Particle Dia. 50 μm Groove Width 150-500 μm Bank Width 250-500 μm	2 mm	Water (T_{sat} = 100 °C)	5 × 5 mm^2 Vertical Rise Height 7-20 mm	~200-350 W/cm^2
Hwang *et al.*, 2010 [40]	Oxidized Sintered Copper Powder with Capillary Artery Posts Particle Dia. 60 μm Artery Pitch 3.52 mm	0.06 mm	Water (T_{sat} = ~40 °C)	10 × 10 mm^2 Distributed Liquid Return	387 W/cm^2
Hwang *et al.*, 2011 [41]	Sintered Copper Powder with Converging Lateral Arteries Particle Dia. 60 μm	0.06 mm	Water (T_{sat} = ~40 °C)	10 × 10 mm^2 Vertical Rise Height ~45 mm	580 W/cm^2
Ju *et al.*, 2013 [42]	Sintered Copper Powder with Converging Lateral Arteries Particle Dia. 60 μm 16-32 1 mm Wide Arteries	0.06 mm Artery 1.5 mm	Water (T_{sat} = ~40 °C)	10 × 10 mm^2 Vertical Rise Height ~45 mm	~350-400 W/cm^2
Weibel, Garimella, 2012 [43]	Sintered Copper Powder with Radial and Square Grid Converging Arteries Particle Dia. 100 μm Porosity 0.5 0.5 mm Wide Arteries	1 mm	Water (T_{sat} = 100 °C)	5 × 5 mm^2 Vertical Rise Height 8.25 mm	437-558 W/cm^2
Coso *et al.*, 2012 [44]	Biporous Silicon Pin Fins with Vertical Micrgrooves Pin Dia 3.1-29 μm Pin Pitch 49.-28 μm Groove Width 30-61 μm Pin Cluster Width 156-288 μm	0.135-0.243 mm	Water (T_{sat} = 100 °C)	6.25-100 mm^2 Vertical Rise Height 5 mm	73.6- 733.1 W/cm^2

Nanostructured Wicks

Authors	Wick Structure	Wick Thickness	Test Fluid	Heater Details	Maximum Heat Flux
Cai, Chen, 2010 [45]	Carbon Nanotube (CNT) Biwick With Vertical Microgrooves	0.250 mm	Water (T_{sat} = 50-100	2 × 2 mm^2 Vertical Rise	~600 W/cm^2

	CNT Dia. <20 nm Groove Width 50 μm CNT Cluster Width 100 μm		°C)	Height ~5 mm	
Cai, Bhunia, 2012 [46]	CNT Biwick With Vertical Microgrooves or Pillar Clusters CNT Dia. <20 nm Groove Width 50 μm CNT Cluster Width 100-250 μm	0.250 mm	Water (T_{sat} = 100 °C)	4 – 100 mm^2 Vertical Rise Height 9-10 mm	130-770 W/cm^2
Cai, Chen, 2012 [47]	CNT Biwick With Microgrooves or Pillar Clusters Groove Width 50 μm CNT Cluster Width 100-150 μm	0.210-0.300 mm	Water	4 – 100 mm^2 Vertical Height ~2-3 mm	195-938 W/cm^2
Nam, Sharratt, Cha, Ju, 2011 [48]	Copper Oxide (CuO) Nanostructured Copper Microposts Post Dia 50 μm Post Pitch 20-50 μm Details in [49]	0.100 mm	Water (T_{sat} = 44 °C)	4 – 25 mm^2 Vertical Height 15 mm	~125-800 W/cm^2
Weibel and Coworkers, 2012 [43,50]	Cu-Functionalized CNT-Coated Sintered Copper Powder with Square Grid Converging Arteries CNT Dia. ~100 nm Particle Dia. 100 μm Porosity 0.5	0.2-1 mm	Water (T_{sat} = 100 °C)	5 × 5 mm^2 Vertical Rise Height 8.25 mm	~450-530 W/cm^2
Kousalya, Weibel, Garimella, Fisher, 2013 [51]	Cu-Functionalized CNT-Coated Sintered Copper Powder Cu-Coated CNT Dia. ~85-275 nm Particle Dia. 100 μm Porosity 0.5	0.2 mm	Water (T_{sat} = 100 °C)	5 × 5 mm^2 Vertical Rise Height 8.25 mm	~350-450 W/cm^2

2 Experimental Evaluation of Capillary-Fed Evaporation and Boiling

It is well-known that the overall effective thermal resistance of a heat pipe is impacted by the response of the wick structure to the evaporator heat load and the internal pressure distribution, which in turn dictate the liquid-vapor interface shape, level of recession into the porous structure, and mechanism by which phase change occurs at the location of heat input. One approach to deducing the impact of these phenomena is by testing actual heat pipe devices and measuring external heat loads and temperatures, according to the procedures reviewed in [2] and [3]; however, the ability to infer detailed information about the phase-change mechanisms by this means, and to quantify the local thermal resistance across only the evaporator section, is limited.

Several studies have devised novel testing approaches that attempt to characterize the thermal resistance across a wick structure under simulated heat pipe operating conditions [29-31,52-54]. The form factors (working length, wick thickness) and operating conditions (heat input area, heat flux) investigated are not strictly applicable to thin vapor chamber heat spreaders; however, these studies represent the first sets of such investigations that offered measurement approaches that informed subsequent studies.

Mughal and Plumb [52] and Williams and Harris [53] both placed an open heat pipe (*i.e.*, a porous wick layer attached to a surface that provided heated, adiabatic, and condenser sections) into a large vapor containment vessel for the purpose of measuring the capillary limit as a function of wick properties, independent of vapor-domain confinement effects. The saturated vapor temperature was measured just above the wick surface, and provided a temperature differential for direct assessment of the evaporation/boiling thermal resistance as a function of heat input. Even though differing working lengths, wick structures, and test fluids were considered, similar trends were observed in both studies. At low heat inputs, the slope of the boiling curve (heat flux versus excess temperature) was linear, consistent with the dominance of the conduction thermal resistance through the saturated wick layer. It was presumed that the evaporation resistance at the liquid-vapor interface was comparatively small, and the measured resistance represented the saturated-wick effective thermal conductivity [53]. The heat flux was slowly increased until a large surface temperature excursion associated with wick dryout and the capillary limit was observed; however, in both studies a sharp reduction in the evaporator thermal resistance was measured prior to dryout. This is attributed to the onset of nucleate boiling, which provides significant improvement in performance, but simultaneously causes premature starvation of the porous structure for the effective working lengths (~100 mm) and heat input areas (>> 1 cm^2) tested. Channels cut into the porous wick structure (1.6 mm wide) reduced the thermal resistance during capillary-fed boiling and extended the maximum dryout heat flux by providing a low resistance path for vapor escape from the surface [52].

An alternative approach for measuring the capillary limit and effective evaporator thermal resistance was developed by Brautsch and Kew [29], who placed a screen mesh wick sample vertically into a large sealed vapor containment vessel. The lower edge of the sample was submerged into a liquid pool, and the working fluid was wicked up the sample surface a distance of 55-79 mm by capillary action to the location of the heat input. The evaporator thermal resistance was directly measured based on a temperature differential between the heated wick base and vapor space. The trend of variation in thermal resistance with respect to increasing wick thickness was reported, and conduction through the saturated wick layer was found to dominate the thermal resistance in an evaporation mode, consistent with the findings in [52] and [53]. Boiling was visually observed in the wick structure prior to complete dryout, but caused an increase in the thermal resistance in all cases. While the single-phase capillary limit and boiling limit have been previously described and treated as distinct phenomena in the literature, the critical conclusion was drawn that they are fundamentally interrelated [29]. The presence of vapor in the wick structure affected both the capillary

pressure generated in the pores as well as the overall pressure drop, resulting in an altered effective dryout heat flux that can not necessarily be predicted by either of the discrete limiting mechanisms.

More recently, the level of liquid charge in a heat pipe (a parameter that could not be varied in the studies discussed above) has been found to play a critical role in determining the evaporator resistance and the modes of phase change that occur. Studies by different groups of researchers – Wong and Kao [55] and Wong and coworkers [56,57] – fabricated heat pipe devices specifically intended for measuring the thermal resistance and visualizing the internal saturated wick structure at the evaporator section. Wong and Kao [55] tested a 150 mm long, 6 mm diameter heat pipe with various screen mesh wick sizes and levels of fluid charge. A range of regimes was observed within the evaporator as a function of heat load. These regimes included evaporation from a saturated wick layer, nucleate boiling in the wick structure, suppression of boiling by recession of the meniscus, and evaporation from a thin-liquid film at the base of the wick structure. While distinct operating conditions that resulted in each regime were not identified, finer mesh sizes and larger fluid charges tended to result in boiling in the wick structure. Wong and coworkers fabricated 120 mm long, 7 mm thick heat pipes with both screen mesh [56] and sintered powder wick structures [57]. For both wick structures boiling was never observed, even at heat fluxes >100 W/cm^2. The decreasing evaporator resistance measured with increasing heat flux was attributed to the meniscus recession observed within the porous structure, and the reduced conduction resistance offered by the portion of the wick that remains saturated with liquid.

Despite the observation of boiling incipience in simulated heat pipes in multiple studies, the occurrence of capillary-fed boiling in actual heat pipe devices remains a point of contention in the literature, as exemplified by the comments of Wong *et al.* [57]. They concluded that the absence of boiling in their studies, using <1 mm thick sintered powder and sintered screen mesh wick structures, proved that the conditions required for boiling are not relevant to electronics cooling applications, and that only overly thick wick structures, fluid overcharge, or fluids other that waterfluids other than water might lead to boiling [57]. The suppression of boiling in highly porous structures is indeed an important observation (as discussed further in Section 2.4), but these authors recognized [56] that conditions giving rise to a large evaporator superheat prior to dryout would undoubtedly result in boiling. While capillary-fed boiling may indeed not have occurred for the device geometry and wick thicknesses tested in [57], which reached a capillary limit at moderate heat fluxes, this conclusion does not consider vapor chamber heat

spreaders that feature very short working lengths (and do not suffer from capillary performance limitations) for which boiling has been shown to be prevalent (see Section 3.4).

In the studies described above [52,53,55-57], although the thermal resistance is measured across the evaporator wick structure, the performance is inextricably related to the test facility geometry and operating conditions. Specifically, the range of heat fluxes investigated was limited by the long capillary wicking length which gave rise to dryout at moderate heat fluxes (~100 W/cm^2). The experimental investigations reviewed in the rest of this section aim to decouple the evaporator performance from overall heat pipe performance. The capillary-fed evaporation/boiling regimes, conditions for transition, and thermal performance of a variety of porous wick structures are discussed.

2.1 Homogeneous Wick Structures: Morphological, Pore Size, Porosity, and Thickness Effects

Observing the capillary-fed evaporation/boiling regimes and determining the effect of parametric wick structure variations in response to a range of heat fluxes from small hot-spot heat sources (less than 1 cm^2) is critical to improved design and operation of ultra-thin vapor chamber heat spreader devices. To evaluate the behavior of specific components and regions of the vapor chambers, test facilities have been devised to feed a wick structure by capillary action under conditions where the effective wicking length is on the same order as the size of the heat input area. Capillary liquid supply is virtually unlimited under these conditions; the viscous pressure drop due to single-phase flow to the heat input area is negligible at all operating conditions investigated.

Several early efforts developed novel facilities of this type, but were targeted at studying the evaporation regime at lower heat fluxes and from larger heat input areas. Hanlon and Ma [30] oriented a sintered powder wick horizontally and maintained constant lateral capillary-feeding to the base of the wick by controlling the height of a separate, hydraulically coupled liquid reservoir. A model was developed to predict the thin-film evaporation performance as a function of wick thickness, but comparison to model predictions was limited due to the observation of boiling during a majority of the experimental data points. The incipience heat flux was described as a critical boiling limit (independent of the capillary limit) that starves the wick of liquid supply; however, the measured performance was only marginally reduced in the boiling regime, and the magnitude of heat transfer coefficients was not consistent with complete dryout. Davis and Garimella [31] investigated a copper powder layer wick sintered onto a pedestal with its top surface sitting just above a standing liquid pool at the base of a thermosyphon. The thin wick layer on top of the pedestal drew liquid on demand from the pool with negligible capillary resistance, and the thermal resistance was measured across the wick layer. Testing was limited to the evaporation regime.

The following subsections focus on similar studies in which the performance and vapor formation regimes are measured up to the point of wick dryout for small heat input areas. Most importantly, these comprehensive investigations considered multiple, independently varied wick parameters for three basic classes of homogeneous wick structures (Figure 3): sintered copper screen mesh, monoporous sintered copper powder, and biporous sintered copper powder (where two characteristic pore sizes are formed by sintering large clusters of small particles).

[Insert Fig3.tif here full-page width]

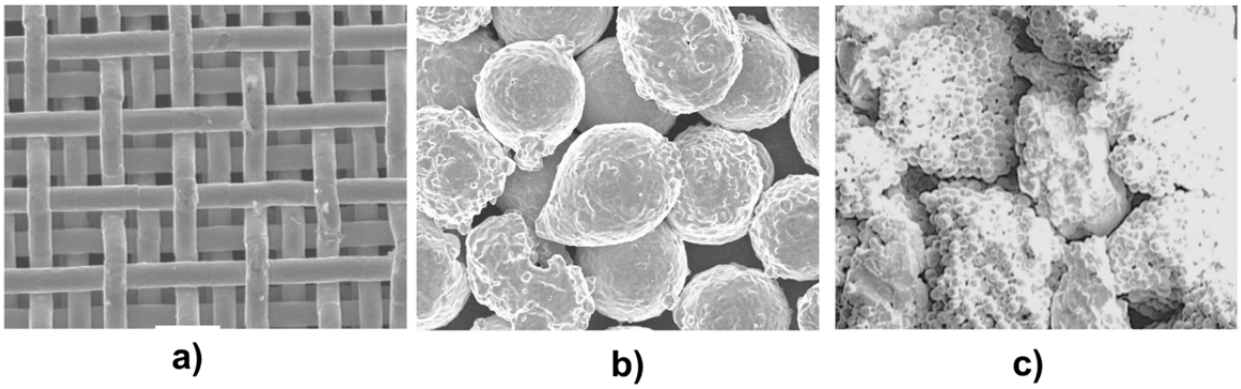

Figure 3. Scanning electron microscopy (SEM) images of (a) a 56 µm wire diameter sintered copper screen mesh [32], (b) 100 µm diameter sintered copper particles, and (c) a biporous wick with 600 µm diameter clusters of 60 µm diameter particles [34].

2.1.1 Sintered Screen Mesh

A series of studies by Peterson and coworkers [32,33,58] investigated the parameters affecting capillary-fed evaporation/boiling heat transfer and dryout heat flux for sintered copper screen meshes. The dependence on overall wick thickness, mesh size, and porosity was independently evaluated using consistent sample fabrication procedures. Based on the collective measurements and observations made, a new boiling curve was proposed for capillary wicking structures.

The range of wick thicknesses and mesh sizes investigated (see Table 1) was chosen based on critical length scales according to conventional bubble nucleation theory. The bubble departure diameter for a heated wall, based on the required buoyant forces required to overcome surface tension-driven adhesion to the surface, is on the order of millimeters for water [59]. Wick thicknesses from 0.21 to 0.82 mm were chosen under the hypothesis that this would prevent formation of discrete rising vapor bubbles within the porous structure. Therefore, bubbles formed in the

wick structure would condense at the liquid-vapor interface at an elevated frequency while being constantly replenished by capillary action, effectively increasing the heat transfer rate at a given superheat [32]. Direct sintering to the heated surface can interrupt and prevent formation of a large lateral vapor film that would induce critical heat flux. An 8 mm × 8 mm sample of the desired wick parameters was directly sintered to a copper heater block of the same dimensions for testing.

The experimental test facility used by Peterson and coworkers [32,33,58] is shown in Figure 4. Degassed water flows into a sealed chamber that contains the sample and heater block. The sample was fed only by capillary action (and did not become submerged) by controlling the liquid level with an outlet overflow system. A heated glass window enabled observation of the sample under test. The facility and data reduction procedures were validated by testing a polished copper surface in a pool boiling mode and comparing results against the literature.

[Insert Fig4.tif here 1/2-page width]

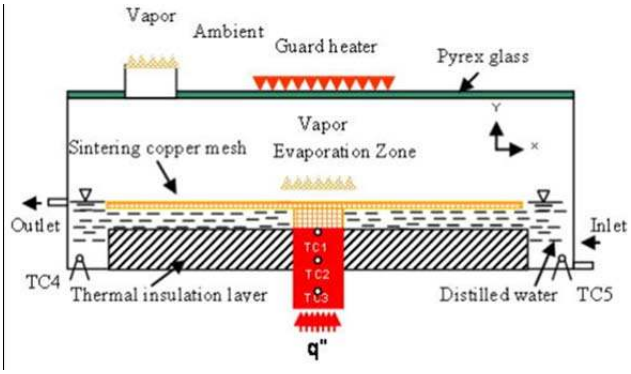

Figure 4. Schematic diagram of experimental capillary-fed evaporation/boiling facility used for testing sintered copper screen mesh [32].

The dependence on wick thickness was first evaluated in [32]. During testing, after a critical incipience superheat was reached, it was clearly observed that both evaporation and boiling occurred in the wick structure (in the form of small bubbles that easily escaped to the vapor space). In contrast to prior studies using thicker wicks [29,30], capillary-fed boiling in the thin wick structures yielded improved performance compared to an evaporation regime; weak dependence of the thermal resistance on the wick thickness suggests that the boiling process, which occurs at the base of the wick structure independent of thickness, governs overall performance (compared to the conduction dominated evaporation regimes described in [30] and [53]). In regards to the limiting heat input, it was noted that a critical heat flux was not induced by vapor blanketing of the surface, but dryout occurred at the center of the heat

source due to capillary starvation in the presence of departing vapor [32]. Hence, this could be considered a capillary limit that is strongly interdependent on the pore-scale vapor departure behavior, as previously concluded by Brautsch and Kew [29]. An increase in the wick thickness delayed dryout via an increase in the available flow area (Figure 5a).

Subsequent investigation [33] revealed the dependence of performance on mesh size, which controls the effective capillary pore size. For all pore sizes investigated from 119-232 μm, the superheat dependence on heat flux was linear in the boiling regime, as observed previously for pool boiling from porous surfaces [19]. A definitive decrease in the capillary-fed boiling thermal resistance was observed with decreasing pore size, and was attributed to an increase in the effective heat transfer area [33]. Conversely, a smaller pore size reduced the measured dryout heat flux (Figure 5b). The menisci were observed to recede to the lowest mesh layer prior to dryout; under this condition, a qualitative analysis of a single meniscus formed between a mesh wire and plane wall showed that larger pore sizes are favored by the tradeoff between capillary pressure and liquid permeability.

[Insert Fig5.tif here 1/2-page width]

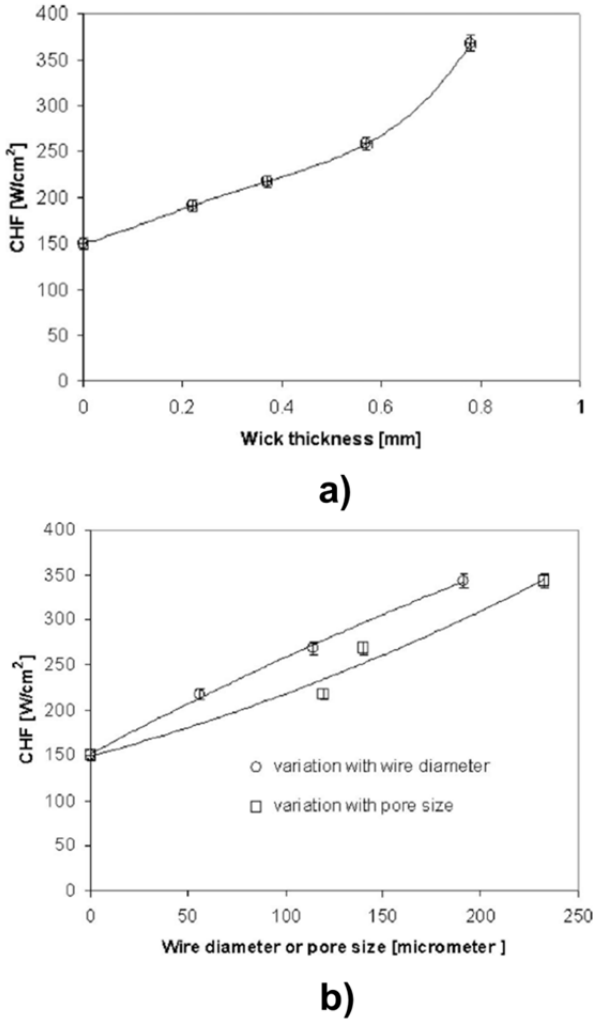

Figure 5. Dryout heat flux (CHF) as a function of (a) wick thickness [32], and (b) wire diameter or pore size [33] for sintered copper screen mesh.

From visualizations acquired for the samples investigated [58], and physical insights obtained from the parametric trends and conventional boiling theory, a new set of capillary-fed boiling curve regimes was proposed for sintered screen mesh wicks (Figure 6). At low heat fluxes, heat transfer primarily occurs by conduction/convection to the evaporating liquid meniscus at the top of the wick structure. Under capillary-fed conditions, a sharp reduction in the surface superheat is observed concurrent with boiling incipience. Performance is improved, and vapor formation does not block capillary supply, as pore-scale diameter bubbles break up and condense at a high frequency (~250 Hz) due to close proximity of the liquid-vapor interface [33, 58]. As the heat flux is increased further, the liquid meniscus recedes and the bubble departure frequency increases; at a critical transition point, the evaporating

meniscus becomes increasingly thin such that the available superheat cannot support nucleation, and boiling is suppressed [33]. The heat transfer coefficient is maximized in this thin-film evaporation regime just prior to dryout.

[Insert Fig6.tif here 1/2-page width]

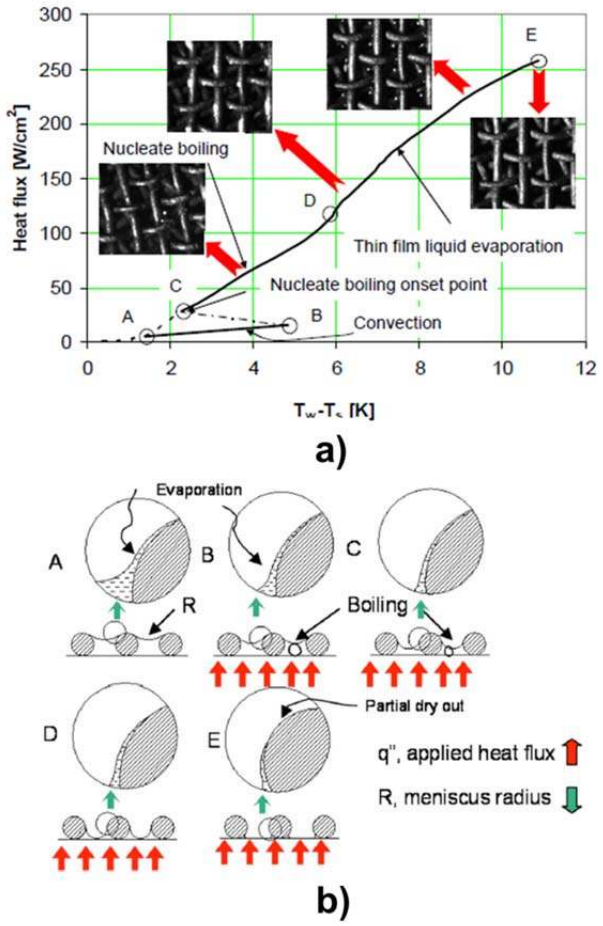

Figure 6. Typical (a) capillary-fed evaporation/boiling curve of heat flux versus wall superheat (T_w - T_s) for sintered copper screen mesh [33], and (b) local phase-change mechanisms as a function of heat transfer regime [58].

2.1.2 Monoporous Sintered Powder

The phase-change regimes, associated thermal resistances, and dependence of performance on wick parameters were investigated by Weibel *et al.* [37] for monoporous sintered copper wicks fed by capillary action. While a number of other studies had considered homogeneous sintered copper powder samples as a baseline for comparison against various enhancement structures, a robust evaluation of the evaporation and boiling processes from this foundational porous structure was lacking in the literature. Hence, a set of sintered powder wick samples were fabricated by

commercial sintering techniques for investigation. Three particle size distributions and three wick thicknesses (0.6, 0.9, and 1.2 mm) were selected for being commonly used in commercial heat pipes and vapor chambers.

A schematic diagram of the test facility used in [37], and in subsequent studies by Weibel and coworkers [43,50], is shown in Figure 7. Copper powder was sintered directly to the surface of a copper substrate to produce a uniform layer of the desired thickness. The back side of the copper substrate was then soldered directly to an insulated copper heater block with a heat input area of 5 mm × 5 mm. The porous sintered copper surface is sealed into a saturated vapor test chamber. Degassed water is continuously fed to the test chamber at the saturation temperature, and the liquid level in the chamber is maintained at a fixed height by means of an overflow drain on the side wall. To ensure liquid feeding exclusively by capillary action, the liquid level is chosen so that only the lower edge of the vertically oriented wick surface is submerged into the pool below. Unlike similar previous facilities [29], the results are independent of orientation and single-phase liquid pressure drop: the distance from the liquid free surface in the chamber to the center of the heat input area is only 8.25 mm and the liquid pressure drop was calculated to be negligible at this effective working length [37]. The thermal resistance and surface superheat were measured as a function of heat flux for each sample tested.

[Insert Fig7.tif here 1/2-page width]

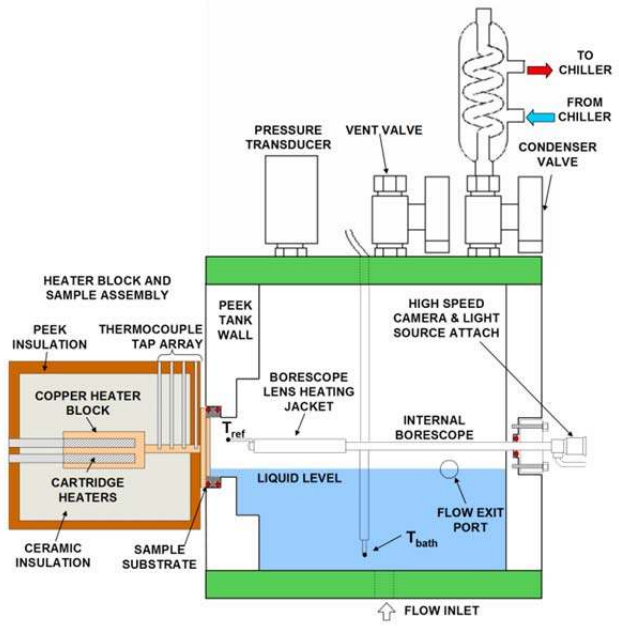

Figure 7. Schematic diagram of experimental capillary-fed evaporation/boiling facility used by Weibel and coworkers [37,43,50].

A test case was presented with fine resolution of heat flux data points and simultaneous *in situ* visualization to identify the boiling curve regimes and associated phase-change mechanisms for sintered powder wicks (Figure 8a). At low heat inputs, approximately less than 75 W/cm^2, visualization confirmed that heat transfer occurred by evaporation from the liquid meniscus at the top of the saturated wick structure [37]. As was found in previous studies [29,52,53], the superheat was linearly dependent on heat flux in this regime, dominated by conduction through the saturated wick layer. At a critical incipient heat flux and wall superheat, boiling in the wick structure caused a sudden transient drop in the surface superheat (in a manner analogous to pool boiling incipience, but at an elevated heat flux due to the low thermal resistance of the evaporation regime compared to natural convection). For the small heat input area investigated, boiling was sustained in the wick structure. Once boiling was initiated, a significant reduction in thermal resistance was measured, with the magnitude of reduction corresponding to the thermal conduction resistance through the wick layer. This reduction was attributed to a transition in the mode of heat transfer from evaporation at the free surface of a liquid-saturated wick to bubble nucleation at the substrate-wick interface, which effectively eliminated the wick conduction resistance (Figure 8b) [37]. This behavior is consistent with previous observations by Mughal and Plumb [52] and Williams and Harris [53], and illustrated the phenomenon more clearly without the confounding effects of a capillary limiting condition. As the heat flux was further increased in the capillary-fed boiling regime, the bubble departure rate increased dramatically (>500 Hz); however, unlike the observations for sintered screen meshes made by Li and Peterson [33], the liquid meniscus did not significantly recede into the wick structure; boiling was sustained at a relatively constant thermal resistance up to the maximum heat flux tested [37]. *Monoporous sintered powder wicks tested in [37] were able to support local heat fluxes of greater than 500 W/cm^2 without the occurrence of dryout.*

[Insert Fig8.tif here 3/4-page width]

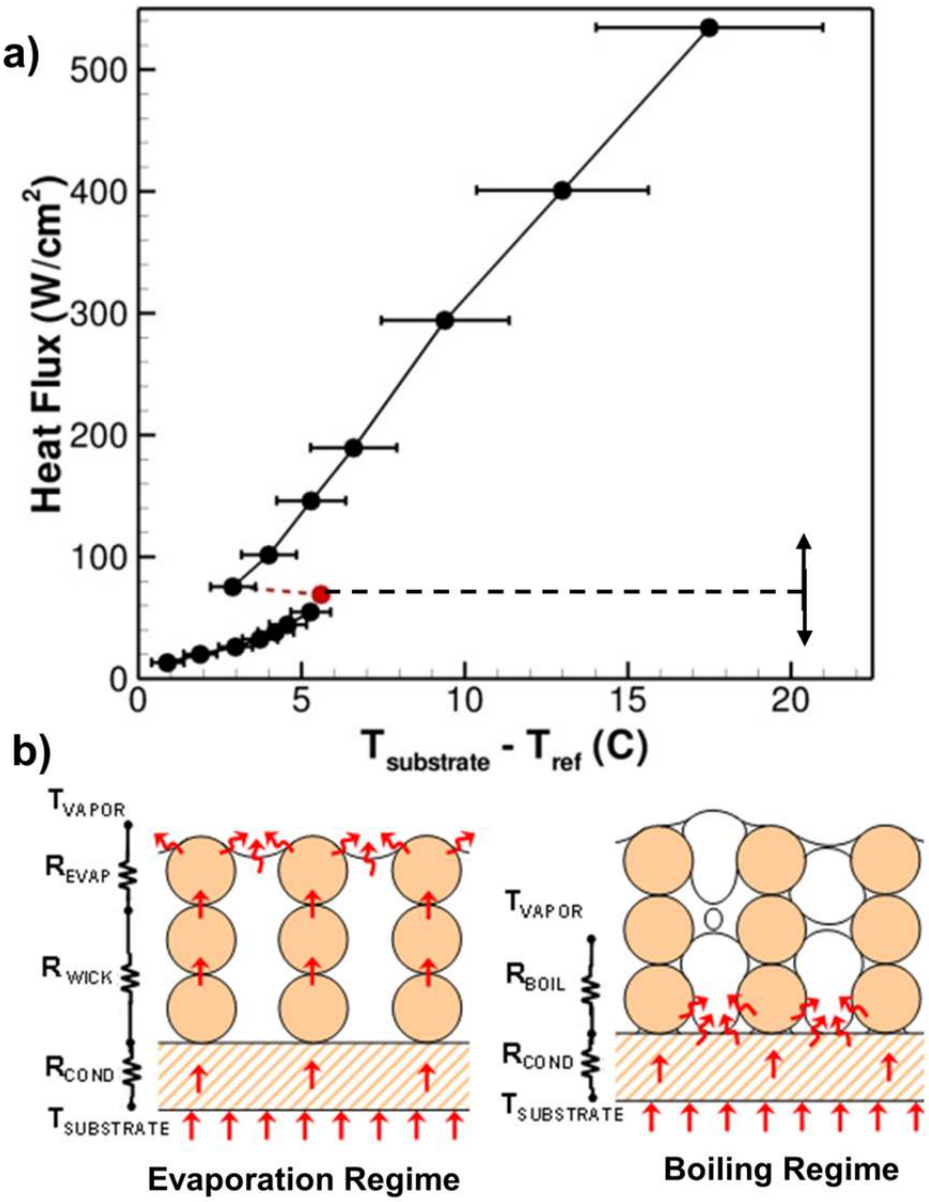

Figure 8. (a) Capillary-fed evaporation/boiling curve of heat flux versus substrate superheat ($T_{substrate}$ - T_{ref}) for a 0.6 mm thick sintered copper powder sample (250-355 µm), and (b) schematic illustrations of the visualized two-phase regimes.

The effect of particle size on the average thermal resistance within the capillary-fed boiling regime is shown in Figure 9. For the thicker wick samples, a minimum thermal resistance was achieved at an intermediate particle size, suggesting an inherent performance tradeoff with decreasing particle size. Li and Peterson [33] previously observed and argued that a decreasing particle size increased the effective surface area for heat transfer; however, Weibel *et al.* [37] observed a reversal in this performance trend for the smaller particle sizes. They attributed the thermal resistance increase at the lowest particle sizes to a reduction in wick permeability that caused an increased drag

resistance impeding vapor escape from the wick. This implies that the optimum size is dependent on wick thickness, and is consistent with reduced optimum particle size for the thinnest wick tested, which would pose the shortest path for vapor escape. Similar observations of optimum thickness-to-particle size ratio have been made in studies of submerged pool boiling from wick structures [60,61]. The observed influence of wick thickness on overall thermal resistance in the boiling regime was negligible. This agrees with the conclusions drawn in [33], and mechanistic arguments presented in Section 2.1.1.

[Insert Fig9.tif here 1/2-page width]

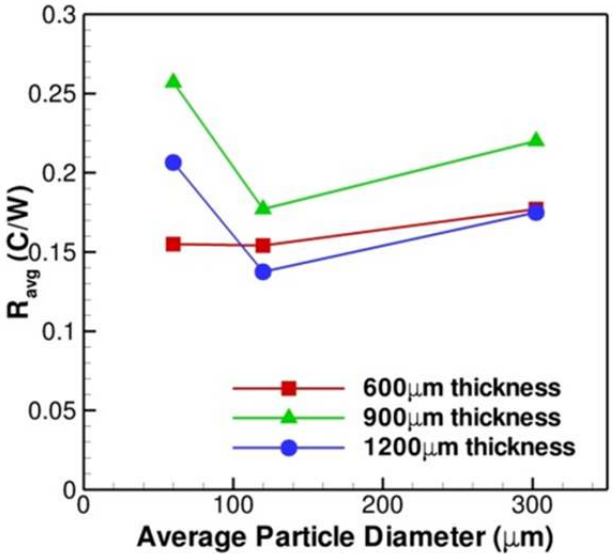

Figure 9. Average thermal resistance (R_{avg}) in the capillary-fed boiling regime (~200-500 W/cm^2) as a function of the average sintered copper powder particle size [37].

2.1.3 Biporous Sintered Powder

Unlike monoporous structures, a biporous (or bidisperse) wick is characterized by two principal pore sizes, and is typically homogeneously composed of large clusters of smaller size particles. Monoporous structures typically remain saturated with liquid and are limited by conduction to the liquid-vapor interface during evaporation. By contrast, the liquid meniscus preferentially recedes in the larger pores of the biporous structure at moderate heat fluxes, allowing increased area for thin-film evaporation from cluster surfaces. Further, during operation in the boiling regime, the large pores allow a path for vapor escape from the surface while liquid is pumped by the small capillary pores.

The capillary-fed evaporation/boiling performance of biporous wick structures was first measured by North *et al.* [34]. For the comparatively large heat input area (30 mm x 8 mm) and long working distance (17 mm) investigated, the menisci in the large pores were observed to continuously recede until dryout was observed at less than 100 W/cm^2. Later, Cao *et al.* [62] also measured the evaporation performance of biporous wick structures, but used a test facility that was intended to replicate the liquid feeding and vapor removal mechanisms that occur in a capillary pumped loop. In both cases, performance was augmented relative to monoporous structures.

Catton and coworkers [35,36,63] were the first to study the capillary-fed boiling process from a small hot spot source (<100 mm^2), independent of single-phase capillary wicking limits, in the test facility shown in Figure 10. A biporous wick sample was sintered to a horizontal copper pedestal that was fed by capillary action from a liquid pool below with minimal flow resistance. The sample sat in a sealed thermosyphon chamber and was heated via an insulated copper block (the size of the heat input area was reduced in successive studies as indicated in Table 1). This approach is similar to the experimental facility devised by Davis and Garimella [31], but incorporated an auxiliary charging port and sight glass to monitor and precisely control the liquid level [35]. The steady-state temperature drop across the wick structure was acquired as a function of heat input for a condenser temperature of 40 °C.

[Insert Fig10.tif here 1/2-page width]

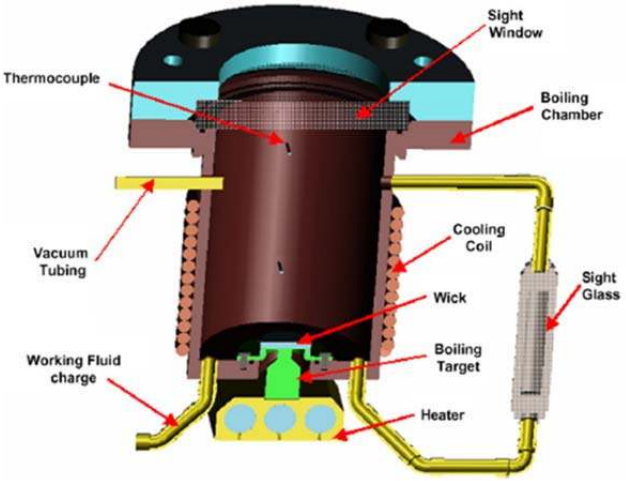

Figure 10. Experimental test rig used by Catton and coworkers for evaluation of capillary-fed evaporation/boiling from biporous sintered copper powder [35].

In the initial study by Semenic *et al.* [35], monoporous and biporous wicks were compared at a thickness of 1 mm. At a constant particle size of 60 μm, the maximum measured heat transfer coefficients were larger for the biporous wicks, demonstrating the effectiveness of the liquid-vapor flow separation mechanism. The relatively low dryout heat fluxes (< 200 W/cm^2) that were measured for monoporous wicks compared to the results of Weibel *et al.* [37] can be attributed to (1) the significantly lower porosity considered, which has been previously shown to reduce the maximum achievable heat flux [33], and (2) the larger heat input area (see Section 2.5).

The objective of a subsequent study by Semenic and Catton [36] was to manufacture copper biporous wicks with a range of different particle diameters, cluster diameters, and wick thicknesses, to inform the design of optimal biporous wick structures. A detailed description of the geometric and thermophysical properties of biporous wicks tested was presented in [64]. In [36], critical heat flux was defined as the heat flux at which the minimum thermal resistance was measured. Large measured critical superheats (> 50 °C) indicated that partial film boiling likely occurred in the wick structure at the minimum resistance value. Critical heat flux measurements from the data set did not reveal a clear mechanistic relationship between reduced thermal resistance and wick parameters. Correlation of the surface heat flux to wick structure yielded an optimum set of wick parameters at a constant surface superheat of 90 °C (Figure 11). This agrees with previous observations of optimal particle size for capillary-fed boiling in the literature [37]. An additional set of different thickness wick structures (0.8-3 mm) was tested at these optimal cluster and particle diameters; decreasing wick thickness led to a lowered thermal resistance at a constant dryout heat flux [36]. While this disagreed with earlier observations for thin monoporous wick layers, the overall biporous wick thicknesses investigated were all significantly larger than those tested in [32] and [37].

[Insert Fig11.tif here 1/2-page width]

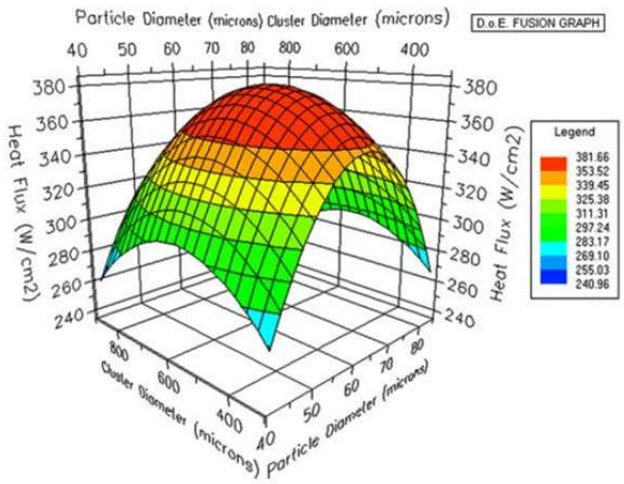

Figure 11. Empirical fit of the surface heat flux as a function of biporous wick parameters at 90 °C superheat[36].

The observed vapor formation regimes and mechanisms [36] associated with boiling from thin biporous layers (<1 mm) are consistent with the proposed analytical models [65]. The wick is initially saturated, and the menisci in the larger capillary pores recede with increasing heat flux, exposing additional liquid-vapor interfacial area. Performance in this regime is governed by the total area for thin-film evaporation from the menisci formed in the interstices of the smaller particles [36], as depicted in Figure 12. Dryout is induced when the smaller capillary pores cannot sustain liquid feeding in the presence of the departing vapor, and occured at heat fluxes in excess of 600 W/cm^2. In contrast, for thicker wick structures, bubble nucleation occurs at discrete sites to form vapor columns within the wick structure. A unique regime was observed to exist in which film boiling occurs in the base of the wick structure, but sufficient liquid is provided to the evaporating menisci above the vapor layer to achieve a minimum thermal resistance at heat fluxes up to 990 W/cm^2, albeit at a large critical superheat of 147 °C [36].

[Insert Fig12.tif here 1/2-page width]

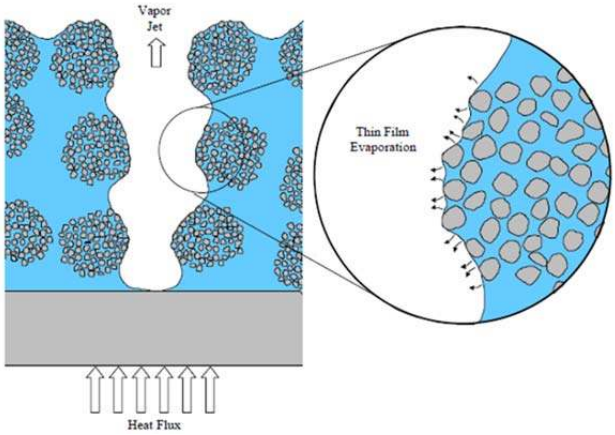

Figure 12. Schematic diagram of thin-film evaporation from the interstitial menisci within a biporous wick [66].

2.1.4 Summary

Comprehensive investigations have been performed for a variety of homogeneous wick structures that isolate and identify the mechanisms of capillary-fed evaporation/boiling from a small hot-spot heat source. Heat transfer regimes that have an increased liquid-vapor interfacial area for phase-change, due to the presence of a vapor phase within the wick structure, provide a reduced thermal resistance compared to conduction-dominated evaporation from the surface of a saturated wick layer. Such regimes may be manifested as pseudo-vapor columns above active nucleation sites with a high departure frequency, or as continuous vapor columns in comparatively larger pore spaces that cannot sustain capillary liquid supply at the given heat flux.

Due to similarities between the dominant heat transfer mechanisms of pseudo- and continuous vapor columns, a number of common enhancement mechanisms are identified. Optimized structures result from pore sizes, porosities, and wick thicknesses that promote efficient vapor removal from the wick structure (which in turn prevents vapor layer formation on the surface, allows for liquid replenishment, and reduces the effective saturation vapor temperature at the surface) as well as an increased area for interstitial phase-change via evaporation or boiling.

The remainder of this section focuses on enhancement and prediction of these common capillary-fed evaporation/boiling mechanisms, and reviews the following: wick structure modification techniques employed to reduce thermal resistance and extend dryout (Section 2.2); prediction of boiling regime thermal resistance as a function of wick parameters (Section 2.3); prediction of transition to boiling regimes (Section 2.4); and prediction of dryout (Section 2.5).

2.2 Efficient Liquid Feeding and Vapor Extraction Features

Improved heat transfer coefficients in capillary-fed evaporation/boiling were demonstrated to be closely linked to increased pore-scale interstitial evaporation area as discussed in Section 2.1; however, excess pressure drop in both the vapor leaving the structure and the liquid feeding the site of evaporation/boiling may increase the effective surface superheat and reduce the dryout heat flux, respectively. While homogeneous structures suffer from the inherent tradeoff between these effects, multi-scale heterogeneous wicks have been proposed to ease vapor escape from the structure with minimal effect on the liquid supply capacity. This multi-scale design approach is analogous to the incorporation of device-scale graded wick structures [4] for reduced liquid-phase pressure drop, but instead focuses on separation of the liquid feeding and vapor extraction flow paths to reduce the vapor-phase pressure drop during high-heat flux operation. Multiple recent studies have designed and tested patterned wick structures to explore potential performance enhancement (Figure 13).

[Insert Fig13.tif here 1/2-page width]

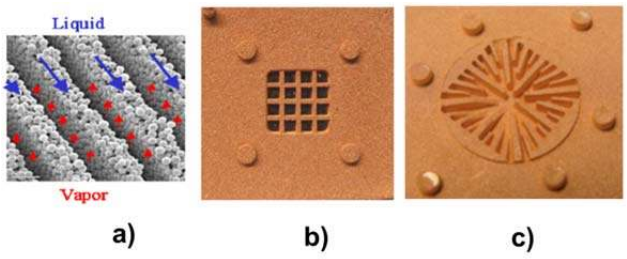

Figure 13. Images of (a) a microgrooved sintered powder wick [39], (b) a grid patterned sintered powder wick tested in [43], and (c) a copper particle monolayer fed by lateral converging arteries [42].

Zhao and Chen [39] investigated capillary-fed boiling from sintered powder structures with and without patterned microgrooves. The performance of the proposed structures was evaluated in a saturated chamber wherein the lower edge of the wick was submerged in a liquid pool set at a fixed working distance below a 5 mm × 5 mm heat source. The microgrooves were aligned in the direction of liquid feeding, and provided open areas to ease vapor escape during boiling. Due to this enhancement mechanism, a 3 mm thick microgrooved wick structure exhibited a dryout heat flux of 350 W/cm^2, compared to 0.5 mm and 3 mm thick monoporous wick structures that dried out soon after boiling incipience at or below 100 W/cm^2 [39]. This dryout heat flux of 100 W/cm^2 is lower than other monoporous sintered wicks in the literature [35,37] was likely due to the extremely small constituent particle size (13 μm effective pore radius). Further testing showed that 500 μm grooves outperform narrower 150 μm grooves that tend to

remain partially filled with liquid. This liquid poses an additional resistance to vapor removal, as evidenced by liquid expulsion from the wick structure observed at higher heat fluxes [39].

In a later study by Weibel and Garimella [43], patterns were fabricated into the sintered powder wick structures over the location of heat input to create a network of capillary feeding arteries; millimeter-scale gaps between the arteries provide increased permeability to vapor exiting the wick. The wick structures were experimentally evaluated in the capillary-fed evaporation/boiling facility described in [37]. High-speed *in situ* visualizations supported the explanation of the relative performance differences between the monolithic and patterned structures as a function of the prevalent heat transfer regime (*e.g.*, evaporation versus boiling) for 1 mm thick wicks, as summarized in Figure 14.

At low heat fluxes, even the largest millimeter-scale pores in the patterned wick structures generated the necessary capillary pressure to maintain liquid saturation. In this evaporation-dominant regime, the patterning replaced high-conductivity copper regions with water, and increased the conduction resistance between the substrate and the evaporating menisci, relative to the monolithic structure. At intermediate heat fluxes, the onset of boiling was observed. In the patterned structures, vapor preferentially departed the surface through the large pores, whereas it was forced to depart through the low-permeability smaller pores of the sintered powder in the monolithic structures. This reduced vapor-phase pressure drop due to the patterning yielded a performance enhancement throughout the boiling regime, and became more effective as the liquid menisci recede into the larger pores of the patterned structures [43]. As liquid in the patterned pores further receded, a thin film was formed over the exposed substrate and nucleation occurred primarily from the corners and sides of the patterned area. Film boiling in this regime was observed to provide the largest comparative enhancement (28.5% reduction in the boiling thermal resistance) versus monolithic structures [43]. It was later shown that patterning of thinner wicks of 200 μm thickness [50] did not provide enhancement due to their inherently lower total frictional resistance to vapor exiting through the structure. It may be inferred that the optimum pattern or groove size is dependent on the wick thickness.

[Insert Fig14.tif here full-page width]

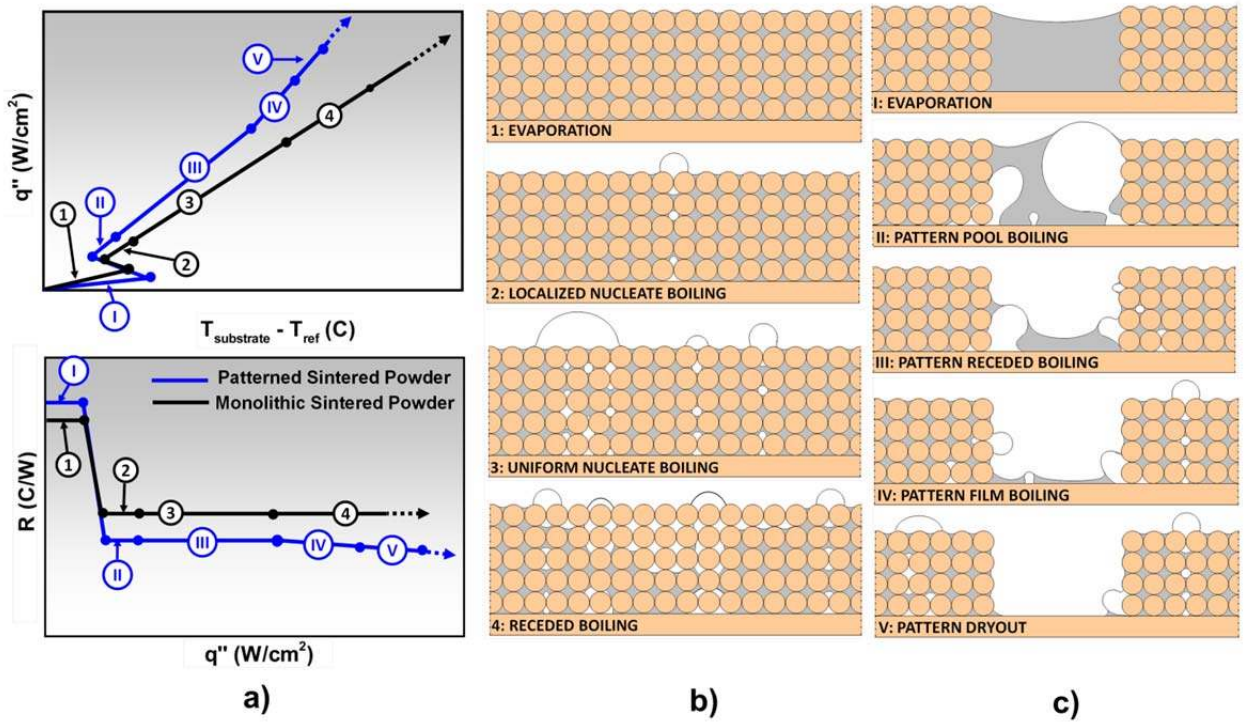

Figure 14. Schematic diagram of typical vapor formation regimes along the (a) boiling curve for (b) monolithic and (c) patterned sintered powder wicks.

A series of studies by Hwang *et al.* [40,41] investigated the use of novel liquid return structures to sustain evaporation from a thin monolayer of 60 μm particles for cooling a 10 mm × 10 mm hot spot. The proposed structures were tested in a vapor chamber device with a condenser surface temperature fixed at 40 °C. The first type of novel liquid return structures investigated were columnar cylindrical arteries distributed over the heated area that fed fluid directly from the opposing condenser surface [40]. The artery geometry tested was optimized using a fluid-thermal resistance network model [67]. While the columnar arteries act to provide local fluid delivery, the performance regimes are determined by evaporation from the thin monolayer of particles. The thermal resistance remained constant for a majority of the heat fluxes up to ~150 W/cm^2, in accordance with models assuming a constant saturated wick thickness. At higher heat fluxes, the thermal resistance varied as the meniscus receded, prior to complete dryout at 387 W/cm^2. Modeling efforts failed to capture the experimental performance, which was attributed to the use of an idealized liquid meniscus profile in the stochastic monolayer [40]. Nucleate boiling was suppressed in the 60 μm particle monolayer, and was not observed.

A second novel liquid-feeding geometry was evaluated by Hwang *et al.* [41]. Unlike the columnar arteries, a set of lateral arteries converged toward the center of the wick structure, again with the purpose of providing distributed liquid flow to increase the evaporation regime dryout limit of a thin sintered monolayer. For this feeding geometry, the thermal resistance was observed to be relatively constant up to a heat flux of ~350 W/cm^2, attributed to a relatively constant liquid level in the monolayer at which the meniscus shape provides maximum capillary pressure [41]. Unlike the columnar arteries, for which sudden dryout was observed, operation after partial dryout was maintained up to 580 W/cm^2 via lateral arteries (albeit at an increased thermal resistance). This was due to the increased lateral inlet flow area to the monolayer provided by the lateral arteries [41]. Further design iterations revealed that an increased number of distributed liquid arteries provided improved performance [42]. Ultimately, a significant increase in the dryout heat flux was obtained, greater than would otherwise be possible for a thin particle monolayer with low evaporative thermal resistance.

2.3 Prediction of Capillary-Fed Boiling Thermal Resistance

In a capillary-fed evaporation regime, it is well-known that the limiting thermal resistance is imposed by conduction through the saturated wick layer. The performance under these conditions is amenable to prediction by assuming an effective thermal conductivity of the wick structure, and depends on the ability to accurately characterize the porous properties. Despite the number of recent experimental studies, development of correlations and methods for predicting the thermal performance during capillary-fed boiling is less explored; however, the inherent similarities between the vapor formation regimes and the governing heat transfer mechanisms observed across a range of homogeneous wick morphologies (see Section 2.1.4) suggests that generalized correlations are possible.

Weibel and Garimella [43] first assessed correlations developed for pool boiling for their ability to predict capillary-fed boiling. Expectedly, because they do not account for enhancement by the porous surface, established smooth surface pool boiling correlations [68-71] over-predicted the surface superheat and failed to capture the boiling curve trends. While there are several existing correlations for pool boiling from porous surfaces [16,72, 73], the empirical dependence on the specific porous morphology, surface material, and test fluid prevented generalized evaluation against a range of wick structures. A semi-empirical method was identified in [43] that predicted boiling performance for generalized porous media, and was validated against experimental data. Smirnov [74] described capillary-fed boiling as evaporation heat transfer from an elementary unit cell of the porous structure represented by a fin coated with a thin-liquid film. The model was later verified against experimental data [75,76]. This model [74]

was shown to compare favorably against capillary-fed boiling data for the sintered powder particle size and porosity investigated by Weibel and Garimella [43].

The simplified conduction model postulated by Smirnov [74] is applicable for both pseudo-vapor columns above active nucleation sites and continuous vapor columns. The thin-liquid layer formed around a vapor column is depicted in Figure 15. Under an assumption that the liquid film thickness is smaller than the vapor column diameter, the saturated wick volume can be modeled as an extended surface. Solving for heat transfer by evaporation from this film-coated fin yields [74]

$$q'' = C\left(\frac{h_{lv}\sigma k_l^3}{\upsilon_l}\right)^{1/6}\left(1-\varepsilon_l\right)^{1/6} k_{eff}^{1/3}\left(\frac{\Delta T_{sl}-\Delta T^*}{L_e}\right)^{5/6} \quad (1)$$

A fitted empirical constant of C = 0.094 for water was recommended based on experimental data obtained using stainless steel meshes and monel balls. Measured experimental data fell within 50% of the predicted value [74].

[Insert Fig15.tif here 1/2-page width]

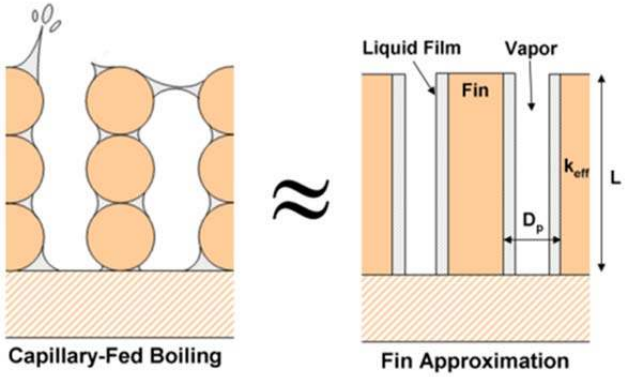

Figure 15. Illustration of the wetted-fin model proposed by Smirnov [74] for prediction of the heat transfer rate under capillary-fed boiling conditions from [38].

A survey of the available experimental data reveals that the studies by Weibel *et al.* [37,43], Li *et al.* [32,33], and Semenic and Catton [36] provide sufficient wick property data to apply Smirnov's correlation [74]. As recommended by the correlation, the effective thermal conductivity for all wick structures was assumed to be a function of the porosity according to

$$k_{eff} = k_{Cu} \frac{(1-\varepsilon)}{(1+\varepsilon/2)} \quad (2)$$

The pore size was assumed to be 40% of the average particle size for the monoporous sintered powder wicks, also as recommended by the correlation. The cluster diameter, which governs the wick permeability to exiting vapor [64], was used to estimate the approximate pore size for the biporous wick structures. The predicted heat flux for a given superheat is evaluated and compared against 428 experimental data points, as shown in Figure 16a. A single empirical constant of C = 0.127 fitted to the data set yields a mean average error (MAE) of 39.4% for the collective data set. Even with a simplified modeling approach, this suggests an improved error bound compared to the advertised correlation accuracy of 50% [74] over a broad range of wick parameters.

Interrogation of the predicted values obtained for each specific data set reveals several trends that are not captured by the model. The different particle sizes tested by Weibel *et al.* [37] fall into distinct groupings (Figure 16b). The correlation exaggerates the trend of increasing performance with decreasing particle size, thereby over-predicting performance for smaller particle sizes. This is likely due to the assumption that vapor columns are maintained in each individual pore. The observations presented in [43] show that the nucleation sites actually engulf multiple pores for small particles, reducing the actual liquid film area for evaporation. This discrepancy with varying pore/particle size is not observed for the sintered screen mesh [33] and biporous wick [36] data, for which pore-scale vapor columns are indeed observed.

For the data of Li *et al.* [32,33], the correlation over-predicts the heat flux at a given superheat for experimental values below ~100 W/cm^2 (Figure 16c). This heat flux coincides with transition to film boiling on the phase-change regime map proposed in [58]. Above this heat flux, liquid recedes into the wick structure and forms pore-scale vapor columns that are mechanistically similar to the proposed correlation; the data points begin to converge above 200 W/cm^2. The correlation best agrees with the experimental data of Semenic and Catton [36]. These data collapse into a single grouping (Figure 16d) with no obvious deviation for a particular cluster size or wick thickness. The relatively large cluster diameters in this work (300 μm - 800 μm) suit the model assumption that the pore size should be much larger than the film thickness. Additionally, the smaller diameter particles in the biporous wick are expected sustain a thin evaporating liquid film surrounding the vapor core.

[Insert Fig16.tif here full-page width]

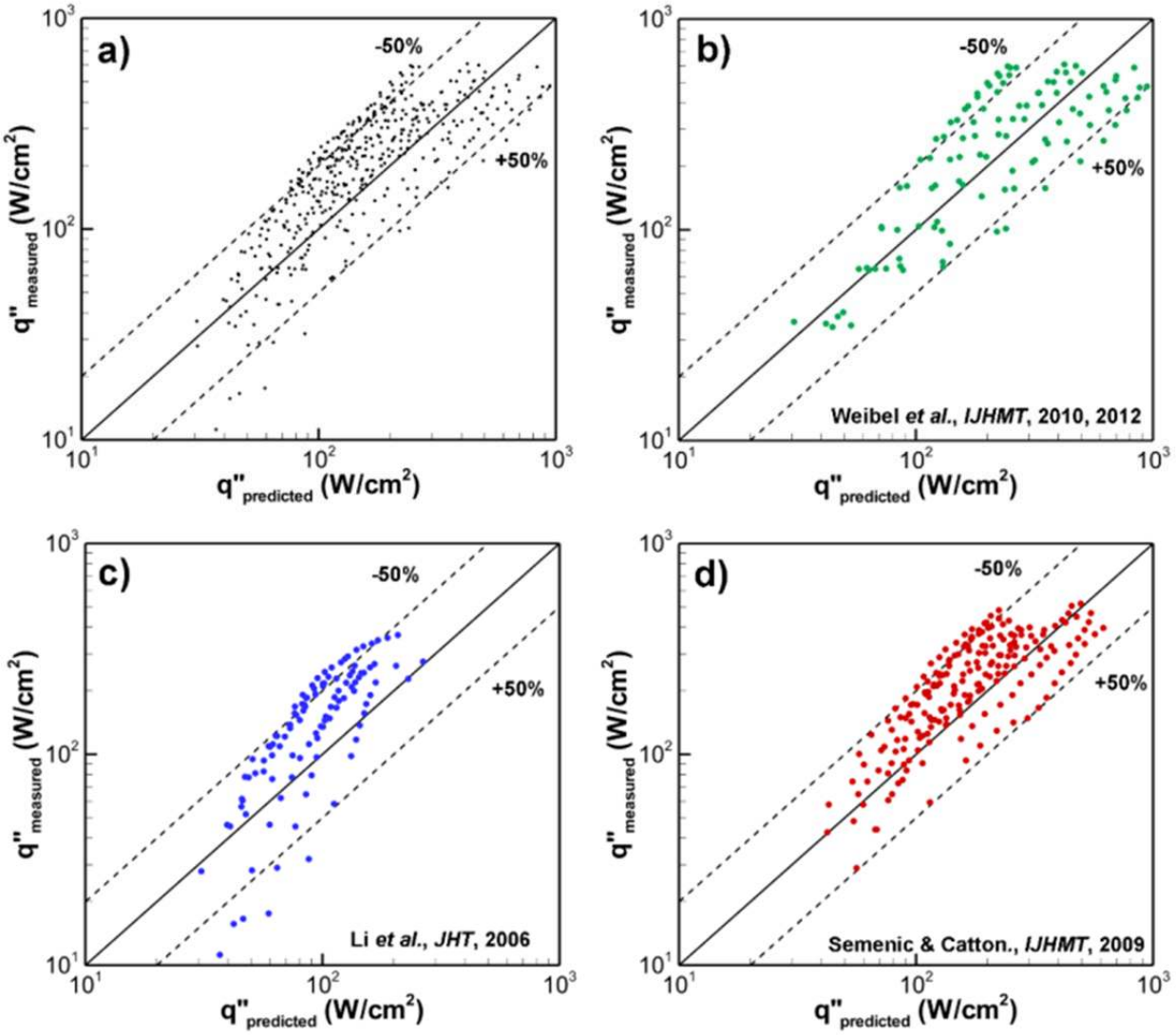

Figure 16. (a) Correlation accuracy of the wetted-fin model proposed by Smirnov [74] for data from the literature [32,33,36,37,43]. Detailed comparisons of the model predictions with data from (b) Weibel *et al.* [37,43], (c) Li *et al.* [32,33], and (d) Semenic and Catton [36] from [38].

The model for capillary-fed boiling proposed by Smirnov [74] is seen to match reasonably well with recent experimental data in the literature reviewed here; however, the density of the vapor columns formed in the wick structure, and the effective liquid film area surrounding the vapor columns, are expected (and observed) to vary uniquely as a function of wick morphology and input heat flux. This leads to the large error observed for some operating conditions in Figure 16. In order to more accurately predict the heat flux versus wall superheat for a given

wick structure, a more accurate representation of the vapor flow structures and interstitial liquid film thickness as a function of operating conditions is required.

2.4 Incipience of Boiling under Capillary-Fed Conditions

Understanding and predicting incipience of nucleate boiling in porous wick structures fed by capillary action is critical to the design of vapor chambers that are subjected to high heat fluxes. As is further explained in this section, bubble nucleation is suppressed under capillary-fed evaporation compared to pool boiling, and the sudden onset of nucleate boiling may cause a larger incipient overshoot in this case. Design of devices for sustained operation in evaporation or boiling regimes may serve to avoid such repeated fast thermal transients that may damage sensitive electronics.

It is well-documented that large incipience superheats are observed for pool boiling from smooth surfaces using highly wetting fluids due to the vapor embryo entrapment process [59]. Surface superheats for pool boiling of FC-72 have been observed in the range of 20-40 °C from platinum surfaces [77] and 10-20 °C from copper surfaces [78,79]. The incipience superheat may be reduced through creation of high cavity-angle sites for vapor embryo trapping [78]. Water has a comparatively higher surface tension, and therefore tends to form stable nucleation sites at lower superheats than highly wetting fluids. This translates into measured incipience superheats of ~10 °C from smooth surfaces [78] and less than 1.5 °C for pool boiling of water from sintered porous surfaces [19,80].

Under capillary-feeding conditions, an increased substrate superheat temperature requirement has routinely been observed for incipience of boiling, even for highly porous structures with a wide distribution of cavity radii. Relatively thick wick structures [29,52,53] yielded boiling incipience at superheats ranging from 1 to 6 °C. Li and Peterson [33] reported superheats of up to 10 °C for the range of sintered screen wick geometries tested, and noted that the required superheat increased with decreasing wick thickness. Wong and coworkers [56,57] tested thin heat pipe devices with sintered screen mesh and sintered copper powder structures and found that superheats up to 13.7 °C did not induce boiling up to the capillary-limited heat fluxes investigated. Boiling is also suppressed entirely for 60 μm particle monolayers up to superheats of 15-20 °C [40]. The most extreme example was provided by Altman *et al.* [81], who performed testing of ultra-thin vapor chamber devices containing sintered powder wicks, and observed incipience at superheats of 20 to 70 °C. The increased incipience superheat due to reduced vapor chamber operating saturation pressure can be calculated using a nucleation parameter [82] that predicts the relative required incipience superheat based on thermophysical fluid properties. Clearly, reduced saturation pressure alone does not

account for the large incipience superheat discrepancy between capillary-fed boiling in vapor chambers and pool boiling at atmospheric pressure. Due to the expected mechanistic differences, conventional pool boiling incipience criteria are not suitable for the analysis of capillary-fed boiling.

All of the studies above based their observations on a single trial using different wick structures; however, it has been previously observed that the inherently variable boiling incipience process yields a large standard deviation in measured superheat heat values, even for exacting replication of test conditions [83]. Incipience criteria are therefore more appropriately defined statistically. The required incipience superheat can be characterized by repeated testing of nominally identical surfaces to develop a probabilistic representation. This approach is typically used to predict pool boiling incipience for highly wetting fluids that are prone to similarly large temperature overshoots [77,78].

Weibel *et al.* [50] characterized the probability of incipience versus wall superheat for capillary-fed 200 μm-thick sintered powder wicks. Boiling was expected to be suppressed for this very thin wick structure compared to thicker structures, based on previous experimental observations in the literature [33,40]. Following a specified surface aging protocol, after which there was no discernible change in trend in the measured incipience superheat, a total of 18 boiling curve trials were obtained using six nominally identical samples. Multiple samples were used to account for sample-to-sample variability as well as variation between multiple trials. The measured substrate superheat at incipience ranged from 2.1 to 19.8 °C, and the data set is represented statistically in Figure 17. The plotted relative cumulative frequency depicts the percentage of total test trials for which onset of boiling began below a given superheat. The slope provides insight into the wide distribution and limited predictability of the incipience phenomenon. It is concluded that capillary-fed thin sintered powder structures can sustain evaporation at superheats greater than 10 °C [50].

[Insert Fig17.tif here 1/2-page width]

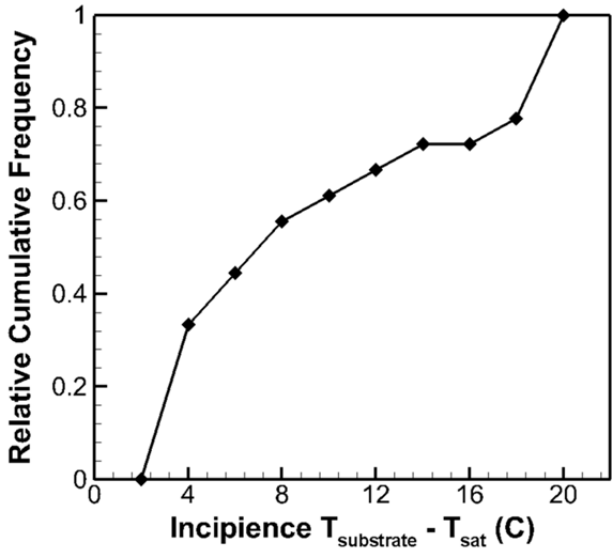

Figure 17. Relative cumulative frequency of superheat-dependent boiling incipience for a 200 µm thick sintered copper powder wick (adapted from [50]).

Several mechanisms that result in sustained evaporation from capillary-fed structures have been proposed. The classical model of Hsu [84]recognizes that the required incipience superheat is based on a limiting thermal boundary layer thickness in the superheated liquid. This model is widely used to understand the nucleation process and agrees with experimental trends for pool boiling. In capillary-fed evaporation/boiling, the liquid menisci recede and form thin liquid films over the particle surfaces with increasing heat input. It was postulated by Weibel *et al.* [50] that these thin liquid films dictate a thin thermal boundary layer that prevents bubble growth and increases the threshold superheat for nucleation compared to pool boiling. This is analogous to the effect of bulk liquid convection that suppresses nucleation in flow boiling. Li and Peterson [33] similarly attributed boiling suppression to the formation of thin liquid films formed in the structure that do not have the necessary superheat to sustain nucleation. Further mechanistic modeling and experimental validation is required to ensure reliable prediction of incipience superheat under capillary-feeding conditions.

2.5 Dryout Mechanisms and Heater Size Dependency

Dryout of the vapor chamber wick at the location of heat input presents a critical limiting condition which results in a rapid surface temperature rise at which the device ceases to operate. Hence, accurate prediction of the dryout conditions is a primary focus for vapor chamber development. For thin vapor chambers intended to operate at a high heat flux but with the heat spread over only a small area, incipience of boiling or formation of vapor columns in the

wick structure is expected to occur before a liquid-phase capillary pressure limitation is reached. Prediction of dryout under these multi-phase flow conditions is critical. Experimental studies of capillary-fed evaporation/boiling often describe dryout mechanisms on a case-by-case basis [29,52], and sometimes as a function of the porous structure [33,36], but an investigation of the sensitivity to heater size has been limited to inferences drawn by comparison between disparate experimental facilities and porous structures.

In pool boiling, the critical heat flux is characterized by transition to film boiling and formation of a vapor layer over the surface, most notably due to instability in the vapor jets leaving the surface and starvation of the liquid at the surface [59]. It has been shown that critical heat flux is partially dependent on the size of the heated surface area due to a change in the proportional perimeter length through which ambient fluid can be drawn to the sites of nucleation. Lienhard *et al.* [85] first proposed that critical heat flux would increase for a finite heater size compared to the assumption of an infinite size for the heated plate. Several subsequent experimental studies [86-89] investigated pool boiling from decreasing heat input areas and confirmed an increase in critical heat flux.

Similar dependence is expected for capillary-fed wick structures due to the distance the liquid must travel to the center of the heat input, especially in the presence of departing vapor. To prevent dryout, the capillary pressure generated under these conditions must overcome the maximum two-phase cross-flow pressure drop for flow to the center of the heated area. Two-phase flow in porous media is generally classified into countercurrent and crosscurrent flow arrangements [90]. Simplified modeling and empirical correlation of two-phase pressure drop is limited to these arrangements [91-94]. Further, pressure drop is highly dependent on the flow regime, and mechanistic predictions cannot be formulated without extensive visualization of the interstitial vapor phase. While comprehensive two-phase pressure drop and flow regime visualization data are not available, several recent studies have focused on studying the influence of heater size on dryout under capillary feeding conditions, as described below.

A strong dependence of the maximum capillary-fed boiling dryout heat flux on heater size was first reported by Nam *et al.* [48]. In common with the testing approaches in all studies discussed in the rest of this section, the wick samples were oriented vertically inside a saturated test chamber. The lower edges of the samples were submerged in a liquid pool below to allow capillary self-feeding. Nam *et al.* [48] fabricated serpentine resistor heaters of two different areas, 4 mm^2 and 25 mm^2, to evaluate the surface superheat response to input heat flux. The wick structures

evaluated were composed of 50 μm-diameter copper microposts with nanoscale surface roughness features. For all samples, boiling was observed in the wick structure after a superheat of ~25 °C was reached. The maximum supported heat flux increased from ~150 W/cm^2 to ~800 W/cm^2 solely due to the heater size area reduction. While a small percentage of this increase is attributable to heat spreading effects in the substrate, the authors ascribe this dependence to capillary supply to the heated area under vigorous boiling conditions [48].

Several studies reported similar findings, and quantified novel dryout mechanisms and heater size dependence metrics. Cai and Chen [47] evaluated the performance of carbon nanotube-based wick structures using heat input areas of 4 mm^2 and 100 mm^2. In the most extreme case, the dryout heat flux increased from 195 W/cm^2 to 938 W/cm^2 due to the reduction in heater area. Due to the high vapor departure velocity at such heat fluxes, a new physical mechanism of liquid loss due to spraying of droplets from the surface was identified [47]. Quantitative measurements revealed that this mechanism accounted for as much as 12% of the total liquid supplied to the hot spot. Coso *et al.* [44] fabricated and tested silicon-pillar wick structures, and observed similar ejection of liquid from the surface at high heat fluxes during nucleate boiling. By testing multiple pillar heights, a critical transition geometry governing the dryout mechanism was observed. For short pillars, the evaporation mode is sustained until dryout; taller pillars produce a higher surface superheat at lower heat fluxes that allows for bubble nucleation [44]. Based on a measured increase in the dryout heat flux from ~160 W/cm^2 to 733 W/cm^2 for a heater size decrease from 100 mm^2 to 6.25 mm^2, the authors proposed a wick-to-heater area ratio metric to capture the qualitative relationship between dryout and heater size [44], but quantitative correlations were not provided.

Weibel [38] proposed a methodology for quantitatively evaluating the effect of heater size. The dryout heat flux was measured for 200 μm-thick sintered copper powder wick structures with heat input areas of 25 mm^2 and 100 mm^2. As shown in Figure 18, a significant reduction in the dryout heat flux was measured for the larger heater area. Vigorous boiling was observed inside the wick structure at dryout. Based on the available capillary pressure head, the approximate two-phase radial pressure drop can be calculated for the superficial vapor/liquid velocities corresponding to the dryout heat flux, and used to extrapolate the dryout limit for intermediate heater sizes. This approach, while limited to a specific wick structure in [38], can be emulated to correlate the two-phase pressure drop at dryout over a wider parametric range.

The dryout heat flux under capillary-fed boiling has been demonstrated to be extremely sensitive to heater size; however, few quantitative prediction methods have been proposed. Additional investigation, and detailed visualization of the vapor-liquid regimes inside the porous structure, is required to develop methodologies for correlating and modeling the complex dryout mechanisms.

[Insert Fig18.tif here 1/2-page width]

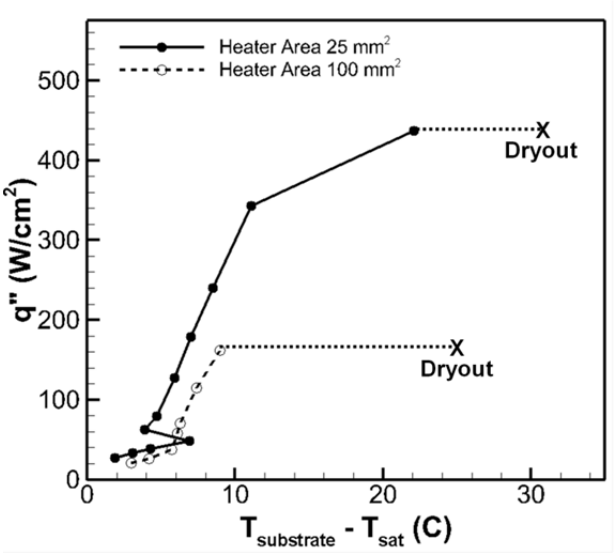

Figure 18. Boiling curve comparing the effect of heat input area for a 200 µm thick sintered copper powder wick (adapted from 38).

3 Device-Level Modeling, Testing, and Design for High Heat Flux Applications

In order to develop vapor chamber heat spreaders with significant enhancements in the maximum heat dissipation and effective thermal conductance within a reduced-thickness package, it is becoming increasingly important to optimize the design of the internal wick and vapor core structures. Optimization via validated device-level models may avoid time-consuming parametric testing approaches, which are confounded by variability due to fabrication, fluid charge, and experimental uncertainties. Modeling of vapor chambers is complicated by the coupled heat, mass, and momentum transport mechanisms prevalent in the device, such as evaporation and condensation at the liquid-vapor interfaces; however, a number of modeling approaches have been developed that approximate transport with various levels of fidelity. Garimella and Sobhan [8] and Faghri [9] provided reviews of the modeling approaches for

a variety of heat pipe device types. Modeling of the transport in thin vapor chambers (*i.e.*, flat heat pipes) is briefly reviewed first, to provide a context for the state-of-the-art advances in modeling approaches discussed in detail in Section 3.2 and Section 3.3.

3.1 Flat Heat Pipe and Vapor Chamber Models

3.1.1 Analytical Modeling Approaches

Simplified one-dimensional thermal resistance network models, such as those presented by Faghri [3] and Prasher [14], account for the dominant conduction and vapor pressure drop resistances in the vapor chamber. While these models only predict steady state performance, and do not capture spatial flow characteristics and operating limits, they enable first-order design for multiple working fluids and different power dissipation levels, and selection of favorable vapor chamber form factors [95], at reasonable accuracy compared to complex, three-dimensional analytical solutions [96]. Additional predictive capabilities can be incorporated into these modeling schemes as necessary. When the vapor core resistance is negligible, Zuo and Faghri [97] predicted one-dimensional transient behavior by assuming that conduction in the wick and wall dominated the thermal response, and showed good agreement with transient, multi-dimensional numerical modeling approaches [98]. Chang *et al.* [99] modified a one-dimensional vapor chamber model to account for the thermal resistance reduction due to liquid meniscus recession at high heat flux inputs. These thermal resistance network models typically assume a given transfer coefficient for the evaporator section of the vapor chamber.

Higher-order analytical models provide additional insight into the vapor and liquid-phase flow profiles and spatial pressure distribution. A series of studies by Vafai and coworkers [100-102] offered detailed analytical models for a specific asymmetric heating profile applied to a flat heat pipe geometry. Vafai and Wang [100] first established the non-dimensional governing equation formulation for pseudo-three dimensional incompressible vapor flow, and solved for device steady-state pressure, temperature, and velocity fields using an integral method. This modeling approach was extended to transient modeling of startup and shut down by Zhu and Vafai [101] and Wang and Vafai [102], respectively. Transient conduction was solved in the saturated wick and wall domains (which govern the overall system time constant), and thermally coupled to a quasi-steady incompressible vapor domain. Analytical modeling results were in good agreement with experimental investigations of the same device [103,104]. An analytical model capable of simulating steady-state vapor chamber operation under a more generalized asymmetric heating profile (having multiple hot spots on one side) was formulated by Lefèvre and Lallemand [105]. To achieve

this, a two-dimensional hydrodynamic model for the liquid and vapor domains was coupled to three-dimensional thermal diffusion in the wall. Most recently, Aghvami and Faghri [106] developed a two-dimensional analytical model that solved mass, momentum, and energy equations in the vapor chamber wall, wick, and vapor domains. A variety of canonical heater/condenser configurations was investigated, and the importance of considering axial variation in the evaporation and condensation rates was noted for high thermal conductivity wall materials. By necessity, each of the individual analytical vapor chamber modeling approaches above represents a tradeoff between simplifying thermal-fluid operating assumptions, limiting investigation to a set or range of external heating/cooling configurations, or reducing temporal/spatial dimensionality.

3.1.2 Numerical Modeling Approaches

Numerical domain-discretization approaches offer the potential for complete description of transient, three-dimensional conjugate heat and mass transfer within the vapor chamber for improved model functionality compared to simplified analytical solutions. Zhu and Vafai [107] expanded their prior analytical model [101] using a numerical approach to solve for three-dimensional vapor flow in the vapor chamber, and revealed the vapor chamber aspect ratios for which a three-dimensional model was necessary to resolve the viscous pressure drop caused by the side walls. Sonan *et al.* [108] implemented a discretized form of the analytical steady-state model developed by Lefèvre and Lallemand [105] to enable transient analysis of a vapor chamber subjected to multiple discrete heat sources.

A number of additional transient, three-dimensional vapor chamber models have been developed independently and are described in the literature. Vadakkan *et al.* [109] developed a three-dimensional numerical model that accounted for vapor core pressurization to study the transient and steady-state response of a vapor chamber with multiple discrete sources. The effects of heat source strength and separation were studied, and the importance of accounting for axial thermal diffusion was noted. Carbajal e*t al.* [110] used a numerical finite volume analysis to obtain the temperature distribution on the back side of a vapor chamber subjected to a non-uniform heating profile. To reduce computational cost, a simplified transient, three-dimensional model intended for implementation into system-level models was developed by Chen *et al.* [111]. The linear model assumed negligible thermal resistance due to vapor convection, and treated the vapor as a common interface between the evaporator and condenser wicks; the utility and accuracy of the model were later demonstrated through analysis of a complete thermal heat sink package with an embedded vapor chamber [112]. Additional detailed, three-dimensional numerical models that solved for flow and heat transport in vapor chambers were presented by Koito *et al.* [113] and Xiao and Faghri [114].

In all of the above studies, the wick-vapor interface was assumed to be flat, and the effect of dynamic meniscus curvature on capillarity was not considered. Tournier and El-Genk [115] developed a two-dimensional axisymmetric model for transient analysis of cylindrical heat pipes. In addition to numerically solving for flow and temperature in the wall, wick, and vapor domains as in the studies above, the analysis approach determined the local radius of curvature of the liquid-vapor interface in the axial direction. Based on experimental observations, a liquid pooling model was incorporated. It was assumed that the equivalent volume of convex menisci formed by transient thermal expansion of working liquid was entrained into the vapor stream and pulled to the condenser section as shown in Figure 19. Rice and Fahgri [116] presented a numerical analysis of the transient operation of a heat pipe with given screen mesh wick structures. This model captured the effects of local evaporative mass flux on the meniscus curvature, and therefore yielded a more accurate approximation of the capillary limit as a function of heat load.

[Insert Fig19.tif here 1/2-page width]

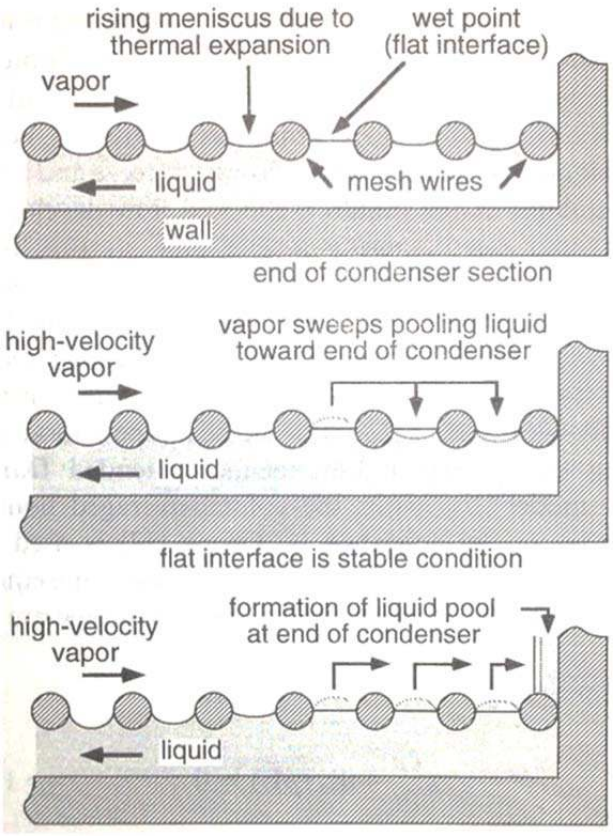

Figure 19. Illustration of liquid pooling at the condenser end of a heat pipe [115].

3.1.3 Summary

Direct representation of the wick structure at a device scale is not computationally tractable, and therefore all modeling approaches assume a representative porous medium domain for the wick structure. While this approach captures device-level transport phenomena, its accuracy hinges upon adequate characterization of the transport properties for realistic wick structures, *viz.* effective thermal conductance, permeability, and capillarity. Furthermore, most modeling approaches do not consider the implications of wick microstructure topology at the liquid-vapor interface on evaporation and heat transfer rates, which become increasingly important in shrinking form factors where surface area-to-volume ratios increase. The numerical models discussed above are also not applicable to high heat flux conditions for which boiling occurs in the wick structure.

Recent advances in the characterization of transport in wick structures are reviewed in Section 3.2, and numerical models that can account for the effects of the wick microstructure at the liquid-vapor interface and boiling are discussed in Section 3.3. Optimization of vapor chambers for high heat flux operation has become possible due to the development of these models. Informed by intensive modeling efforts and subcomponent testing described in Section 2, the recent design, development, and testing of nascent ultra-thin vapor chamber technologies is then described.

3.2 Wick Thermophysical Properties and Pore-Scale Evaporation Characteristics

To enable device-scale analysis of transport in wick materials, pore-scale transport mechanisms are typically averaged over a suitably larger-scale representative elementary volume for which macroscale governing equations can be formulated [117]. To employ this approach, geometry-specific relations are required for estimating the representative transport properties of interest, *viz.* thermal conductivity, permeability, capillary pressure, and evaporation/condensation mass transfer. The effective wick transport properties can then be represented on a simplified basis in device models (see Section 3.1).

3.2.1 Simplified Analytical Prediction

Several approaches commonly employed for prediction of transport properties are based on simplified representations of the wick geometry. The effective thermal conductivity of saturated porous media is often represented as a function of the porosity and solid/liquid-phase thermal conductivities. At a given porosity, commonly suggested expressions [3,4] represent meshes as a square array of uniform cylinders [118] and sintered powder beds as having randomly dispersed liquid-phase spheres [119].

The pressure drop imposed to flow through a porous medium is correlated to the superficial velocity usingthe permeability of the medium in Darcy's law [90], given by

$$\nabla P = -\frac{\mu \vec{V}}{K} \quad (3)$$

For a collection of common wick structures [3], expressions for permeability are derived assuming Hagen-Poiseuille flow through passages in the porous structure having a hydraulic diameter representative of the pore size and geometry. The Carmen-Kozeny theory uses a hydraulic radius to predict the friction factor of a porous matrix [90].

The capillary-pressure difference generated by surface tension across a spherical curved liquid-vapor interface in a capillary tube is given by the Young-Laplace equation as

$$\Delta P = \frac{2\sigma}{R} \quad (4)$$

where R is the radius of curvature. For non-spherical menisci formed in actual wick structures, an effective radius of curvature (or pore radius) is typically defined based on simplifying geometric approximations or empirical observations, as summarized in [3]. The evaporation/condensation resistance from these menisci can be estimated locally based on the interfacial mass flux as described using the kinetic theory of gases by Schrage [120]

$$\dot{m}_i'' = \frac{(2\hat{\sigma})}{(2-\hat{\sigma})}\sqrt{\frac{\bar{M}}{2\pi\bar{R}}}\left(\frac{P_v}{T_v^{1/2}} - \frac{P_i}{T_i^{1/2}}\right) \quad (5)$$

This formulation can be used to predict the detailed evaporation characteristics of an extended liquid film [121] or a meniscus in a simplified geometry [122], but generalized analytical expressions for evaporation from saturated wick structures are not available.

3.2.2 Empirical Characterization

The simplifying assumptions employed in analytical predictive methods prevent accurate portrayal of transport characteristics for realistic wick structures over a broad range of geometries. In order to improve prediction accuracy and enable validation of device-level models, effective transport properties must typically be determined experimentally. Studies that review empirical correlation of heat pipe wick transport properties are briefly summarized below.

Effective thermal conductivity is typically measured by maintaining a one-dimensional temperature gradient across a wick sample at a known heat flux [123]. Atabaki and Baliga [124] reviewed several thermal conductivity models for two-phase mixtures and developed a modified empirical correlation based on experimental data for sintered metal powders [123,124]. Similar testing of biporous and monoporous sintered copper powders performed by Catton and coworkers [64,125] revealed that the effective medium theory model [126] discussed by Carson *et al.* [127], which assumes a random dispersion of both material phases, provides an upper bound on effective thermal conductivity. Li and Peterson [128] reviewed models for predicting the effective conductivity of layers of wire screen, and performed experiments using sintered screen to validate a proposed analytical model as a function of the mesh number and wire diameter. Zhao *et al.* [129] formulated a more generalized screen mesh thermal conductivity model in comparison to previous efforts [128,130] that accounted for arbitrary weave patterns.

The permeability of a wick can be found by forcing liquid through a representative sample at a known flow rate and measuring the resultant pressure drop, either in a linear [131] or radial orientation [132]. Kozai *et al.* [131] investigated the permeability of metal screen wicks as functions of the number of layers, mesh size, and screen compression. An empirical correlation for permeability was developed, and geometries were identified for which accuracy was improved compared to the modified Blake-Kozeny equation [1]. A number of additional comparisons have been drawn against the Carmen-Kozeny theory based on experimental measurement of felt [133], metal screen [134], sintered powder [125], and composite [135] wick permeability.

Several methods are available for evaluating the capillary pressure generated in the pores of a realistic wick structure. In the bubble-point method [136], the capillary pressure is determined based on the minimum pressure required to penetrate gas through the sample; a bubble will first pass through the largest pore, providing a conservative estimate. Conversely, the maximum capillary pressure can be determined by measuring the pressure head sustained by a plug of wick material holding a liquid column against gravity [64,125,137]. An alternative method is to measure the transient rate of rise of liquid in a sample to predict the capillary pressure and permeability based on Washburn's equation [138], as first described with respect to heat pipe wick materials by Adkins and Dykhuizen [132]. Holley and Faghri [139] improved upon the viability of this technique by measuring the liquid mass uptake instead of relying on visualization of a uniform liquid front, and by quantifying mass loss due to evaporation. The technique has been recently utilized to characterize a variety of monoporous [38,140] and biporous

[141] powder, composite [135], foam [142], micropillared [143], and nanostructured copper post wicks (Figure 20) [49].

Simplified analytical correlations relating evaporation characteristics to wick microstructure do not exist, and most modeling approaches assume evaporation from a flat liquid-vapor interface. Numerous experimental efforts [29-31,53-57], as described in Section 2, have measured the combined conduction and evaporation resistances of saturated wick structures; however, direct comparison of local evaporative mass flux predictions against experiments are usually limited to more simplified geometries [144-149150].

[Insert Fig20.tif here 1/2-page width]

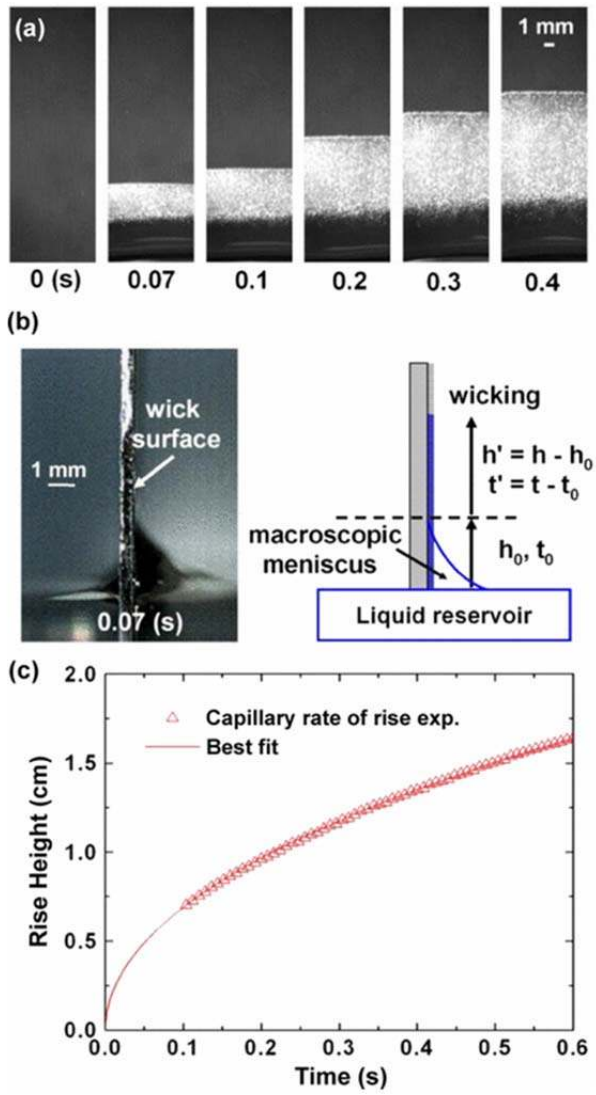

Figure 20. Example capillary rate-of-rise experimental result performed for a nanostructured copper post wick showing (a) selected images of the liquid front, (b) side view of the sample under test, and (c) best-fit Washburn's equation to experimental rise height versus time [49].

3.2.3 Advances in Characterization Methods

Simplified analytical approaches can readily predict transport properties as a function of wick geometry, and are convenient for use in device-scale models, but they lack accuracy. To avoid the need for empirical correlation of transport for each desired wick structure, several numerical prediction approaches have recently been employed, and are reviewed here. These recent advances have enabled the design of novel wick microstructures for ultra-thin vapor chambers.

With the advent of microtomography techniques that provide submicron resolution, it is possible to obtain intricate three-dimensional details of stochastic porous wick structures to enable direct simulation of transport. A review of this characterization approach with respect to sintered powder wicks is reviewed in detail in [151]. Direct simulation of transport yields improved accuracy compared to experimental methods that have practical measurement uncertainties. Bodla *et al.* [152] performed computations to resolve the effective thermal conductivity and permeability of commercial sintered wicks composed of multiple particle sizes. The computations showed that the effective thermal conductivity of sintered wicks was a strong function of sintering conditions and the resulting morphology, *viz.* the inter-particle necking, which could not be captured by available predictive methods [127]. Similarly, simplified analytical expressions for permeability [90] significantly over-predicted the computed values due to non-spherical particle shape. Correlated functions of thermal conductivity and permeability for realistic wick structures were proposed [152].

In order to develop a methodology for reverse-engineering capillary wick structures, multiple recent studies have performed numerical analyses to predict the capillary pressure and evaporation characteristics for three-dimensional representative unit-cells. Ranjan *et al.* [153] investigated the capillary pressure of several idealized geometries, such as hexagonally packed and square-packed spheres, as representations of sintered powder structures. To improve accuracy compared to simplified effective capillary pore size approximations [3], the interstitial three-dimensional static liquid-vapor interface shape was obtained by evolving the free surface toward a minimum energy configuration by a gradient-descent method [154], as shown for parallel horizontal cylinders and hexagonally packed spheres in Figure 21. The maximum capillary pressure along the interface was obtained via the Young-

Laplace equation, and then compared for the different structures (Figure 21c); evaporation characteristics were approximated by determining the percentage meniscus area below a defined thin-film thickness [153]. Nam *et al.* [49] employed a similar approach to determine the capillary pressure within an array of microposts. In addition, the permeability of the micropost array was determined by imposing a pressure gradient across the unit cell and assuming slip conditions at the fixed liquid-vapor interface. A performance parameter, K/R_{eff}, was defined to evaluate permeability versus capillary pressure as a function of micropost diameter and pitch [49].

[Insert Fig21.tif here 1/2-page width]

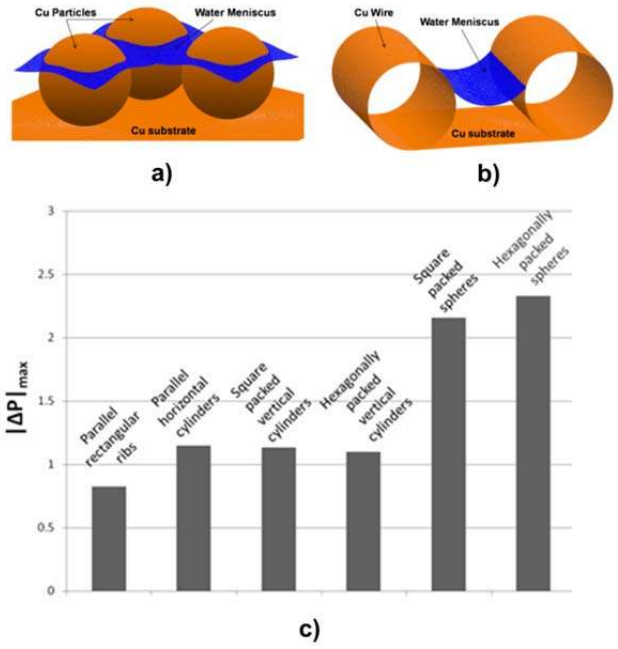

Figure 21. Example liquid-vapor interface shapes in (a) hexagonally packed spheres and (b) parallel horizontal cylinders obtained via surface energy minimization, and (c) an assessment of the maximum non-dimensional capillary pressure achieved in different topologies at any liquid volume for 64% open porosity and a fixed liquid-solid contact angle of 15 degrees [153].

To improve upon the simplified resistance network evaporation models for representative wick pore geometries developed earlier [153], Ranjan *et al.* [155] formulated a numerical approach to solve three-dimensional heat transport and evaporation from the same canonical topologies. Static interface shapes were discretized for finite volume computational analysis under the prescribed boundary conditions shown in Figure 22a. A constant wall superheat was imposed, and fluid was replenished at the base of the wick structure to accommodate evaporative

mass loss at the interface. This model resolves the non-isothermal interface conditions that result in thermocapillary convection and non-uniform evaporative mass flux along the interface (Figure 22). After validation against an analytical model for evaporation from a channel [122], a comprehensive investigation of the local and area-averaged evaporative mass flux was performed as a function of contact angle, surface superheat, pore geometry, and length scale. Similar modeling approaches that account for non-isothermal evaporation from a quasi-static liquid meniscus are presented in the literature. Dhillon *et al.* [156] investigated evaporation from micron-size rectangular channels representative of a micro-columnated porous silicon wick design. Hwang *et al.* [41] employed this local thermal nonequilibrium modeling approach to evaluate the effective thermal resistance of evaporation from a monolayer of spherical particles. Bodla *et al.* [157] described the evaporative resistance imposed by a realistic sintered powder wick via microtomography-based direct simulation.

[Insert Fig22.tif here 1/2-page width]

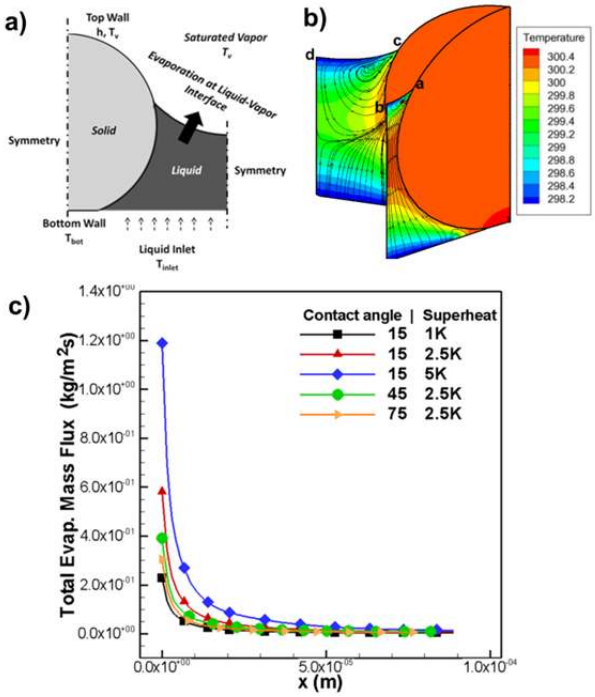

Figure 22. (a) Illustration of boundary conditions imposed for the evaporation model and (b) example temperature contours and particle paths formed between square packed spheres. (c) The evaporative mass flux along the interface is shown for 200 µm spheres at a pitch of 178 µm, 56% porosity, and a saturated vapor temperature of 298 K [155].

Novel structures that enhance performance parameters of interest have been developed using these numerical methodologies for evaluation of wick capillarity, permeability, and evaporative resistance on a unit-cell basis.

Ranjan *et al.* [158] computed correlations for the permeability, capillary pressure, and percentage thin-film meniscus area for cylindrical, conical, and pyramidal pillared wick structures (proposed to increase performance compared to sintered particle monolayers). For cases comparing performance at a fixed permeability, pyramidal topologies were shown to provide the highest evaporation rate due to stretching of the liquid thin-film meniscus (Figure 23). When compared against spherical particle monolayers, an order of magnitude improvement in the estimated capillary limit was calculated, albeit at a moderately reduced evaporation rate [158]. Sharratt *et al.* [159] used the same modeling approach to predict the permeability and effective evaporative heat transfer coefficient for novel pillared geometries as a function of the apparent solid contact angle. Hexagonal arrays of cylindrical pillars served as the baseline for comparison against novel pie-cut cylinders and clusters of cylinders (Figure 24a-c). Due to the increased flow area available in the novel geometries, permeability is increased; however, the baseline structure always had the highest permeability for a constant solid fraction [159]. In regards to the effective evaporation resistance, the pie-cut cylinders provide the most favorable tradeoff between increasing liquid meniscus contact line length and decreasing thermal conductance from the substrate to the liquid meniscus. As shown in Figure 24d, predictions are compared to experimental measurements for silicon pillared wick structures.

[Insert Fig23.tif here 3/4-page width]

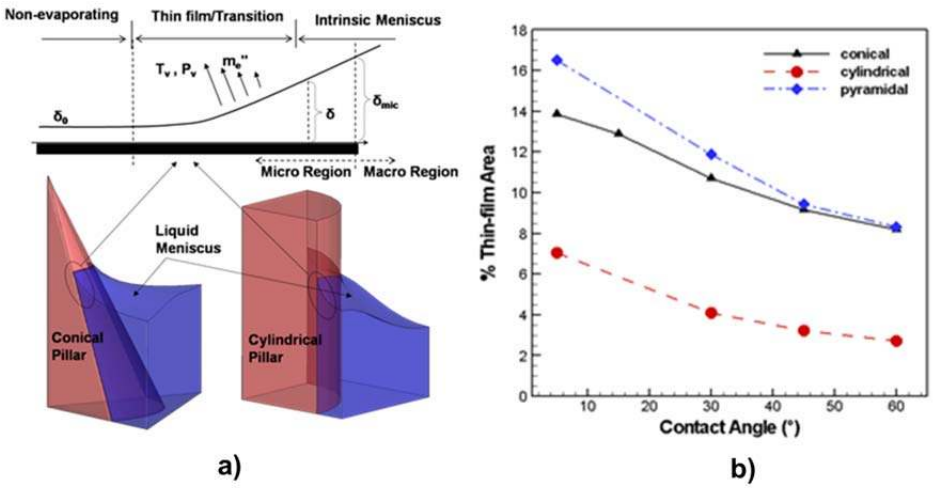

Figure 23. (a) Schematic diagram showing the meniscus profile obtained for conical and cylindrical pillared wick geometries, and (b) comparison of computed percentage thin-film area as a function of apparent contact angle at constant permeability [158].

[Insert Fig24.tif here 3/4-page width]

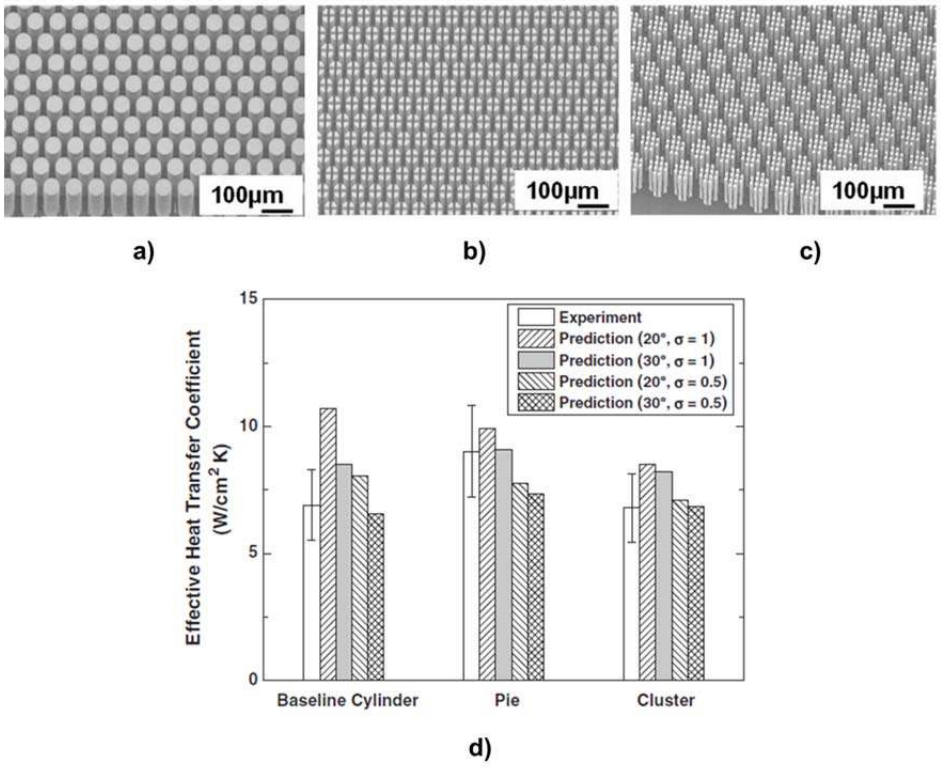

Figure 24. SEM images of (a) cylindrical, (b) pie-cut, and (c) clustered silicon pillared wick structures, and (d) comparison of experimentally measured and predicted effective heat transfer coefficients [159].

3.3 Recent Advances in Ultra-thin Vapor Chamber Modeling

The review of vapor chamber and flat heat pipe modeling approaches in Section 3.1 revealed that a majority of the numerical modeling approaches do not consider the wick microstructure on flow and heat transfer. While several models [115,116] accounted for local meniscus curvature effects on capillarity, the effect of local meniscus shape on evaporation was not considered. While the thermal resistance due to evaporation from the wick structure is typically small compared to conduction resistance through the wick layer, as device dimensions are reduced, and wick structure structures becomes increasingly thin and conductive [158,159], liquid-vapor interface resistance is expected to play an important role in determining overall device thermal resistance. Further, extant numerical models do not account for boiling in the wick structure despite extensive evidence of the prevalence of this heat transfer mechanism in wicks subjected to high heat flux hot spots (see Section 2). Recent advances in modeling approaches that address these limitations, specifically for the design and development of ultra-thin vapor chamber heat spreaders for operation at high heat fluxes, are reviewed in this section.

3.3.1 Wick Microstructure Effects on Evaporation Characteristics

During vapor chamber operation, a gradient in the capillary pressure across the liquid-vapor interface is established along the device. Therefore, local meniscus curvature is highest at the evaporator section of the device, where the largest system pressure head must be sustained by capillary forces, and flattens toward the condenser section. This interface shape dictates the thickness of an extended thin-liquid film formed within the wick pores, and determines the local evaporation/condensation heat transfer characteristics. To capture these effects, Ranjan *et al.* [160] developed a numerical approach wherein a macroscale device-level model was coupled with a sub-device microscale model that predicted meniscus shape and evaporation from a representative unit cell structure.

The device-level model used by Ranjan *et al.* [160] was an adapted version of the flat heat pipe model originally developed by Vadakkan *et al.* [109]. The mass, momentum, and energy equations are solved in the solid, porous, and vapor domains to determine the temperature and pressure fields within the device. To account for phase change by evaporation/condensation, the interface temperature is first obtained from an energy balance that accounts for conduction/convection on the liquid and vapor sides of the interface. The local interface pressure is determined by the Clausius-Clapeyron equation, and the local interface mass flux can be calculated using a kinetic theory-based [120] evaporation formulation. Transient pressurization of the vapor chamber due to net mass flux across the interface is incorporated by changing the vapor density by a concomitant amount. The microscale model for evaporation from a porous unit cell is reviewed in Section 3.2.3 and is described in detail in [155]. The meniscus shape is calculated via a surface energy minimization approach, and conjugate heat transfer and evaporation are computed numerically for the static meniscus shape.

The macroscale device model computes the local interfacial pressure drop along the device; however, it assumes a flat meniscus. Therefore, Ranjan *et al.* [160] developed correction factors to the interfacial area and evaporative mass flux to account for changing liquid-vapor interface shape, thin-film evaporation, and thermocapillary convection effects. In summary, the coupling procedure first computes the flow and temperature fields using the device-level model. The microscale model is then used to develop a correlation for the local contact angle as a function of the capillary pressure difference across the interface, as obtained from the device model. For the computed contact angle, correction factors are introduced to account for the difference in evaporation mass flow from a flat versus curved interface. The mass flux and meniscus area correction ratios are obtained as a function of

wick porosity and interstitial contact angle via best-fit regression of the micromodel outputs. Example correction ratios and temperature contours for a flat interface versus a wick pore are shown in Figure 25.

[Insert Fig25.tif here 3/4-page width]

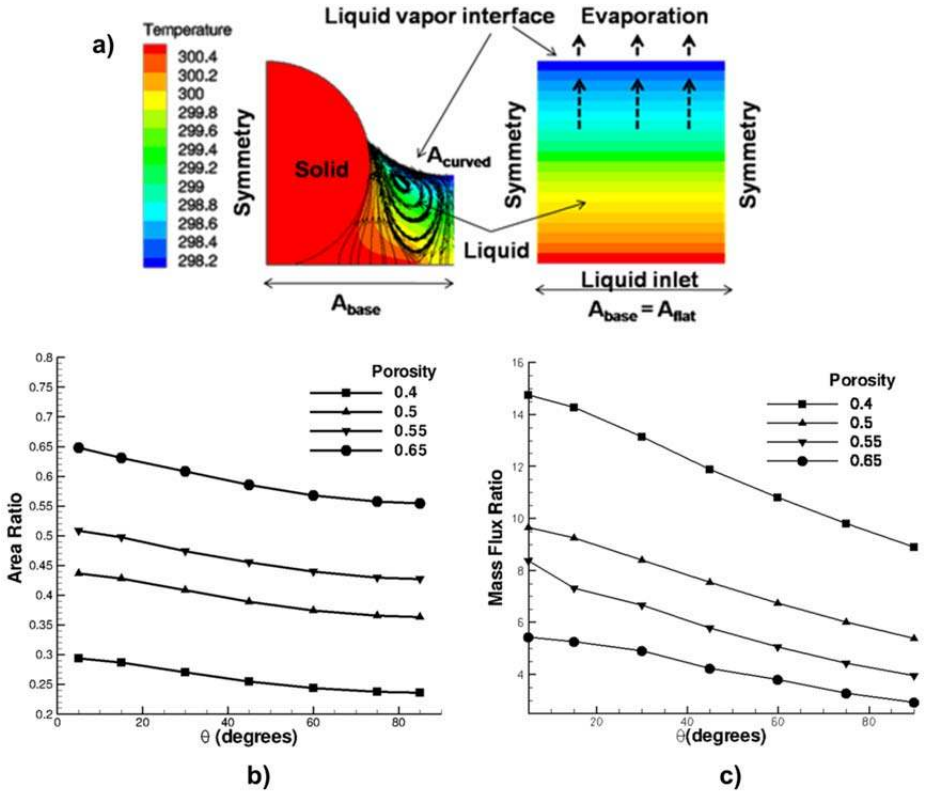

Figure 25. (a) Temperature contours for a liquid meniscus formed in a wick pore and under a flat meniscus with 2.5 K base superheat above the vapor temperature (298 K), and the associated (b) area and (c) mass flux correction ratios corresponding to an accommodation coefficient of 1 [160].

To evaluate the effects of microscale correction ratios on device performance, Ranjan *et al.* [160] investigated the vapor chamber geometry shown in Figure 26, and solved for flow and temperature in the domain using the coupled model. Details of the boundary conditions imposed and the wick, liquid, and vapor thermophysical properties can be found in [160]. As can be observed in Figure 26, the correction factors are maximized at the location of highest interfacial pressure difference at the center of the heat input, and decrease toward the condenser side. The correction ratios were found to be a strong function of the working fluid accommodation coefficient, leading to a maximum temperature correction due to the inclusion of the microscale meniscus effects of 16% among the cases investigated [160]. The investigation concluded that the need for a coupled model is imperative for wick thicknesses on the order

of 100 μm, high wick effective thermal conductivities on the order of 100 W/mK, and low accommodation coefficients [160]. Common to these criteria is an increase in the importance of the thermal interfacial resistance associated with evaporation compared to conduction through the wick layer.

[Insert Fig26.tif here 3/4-page width]

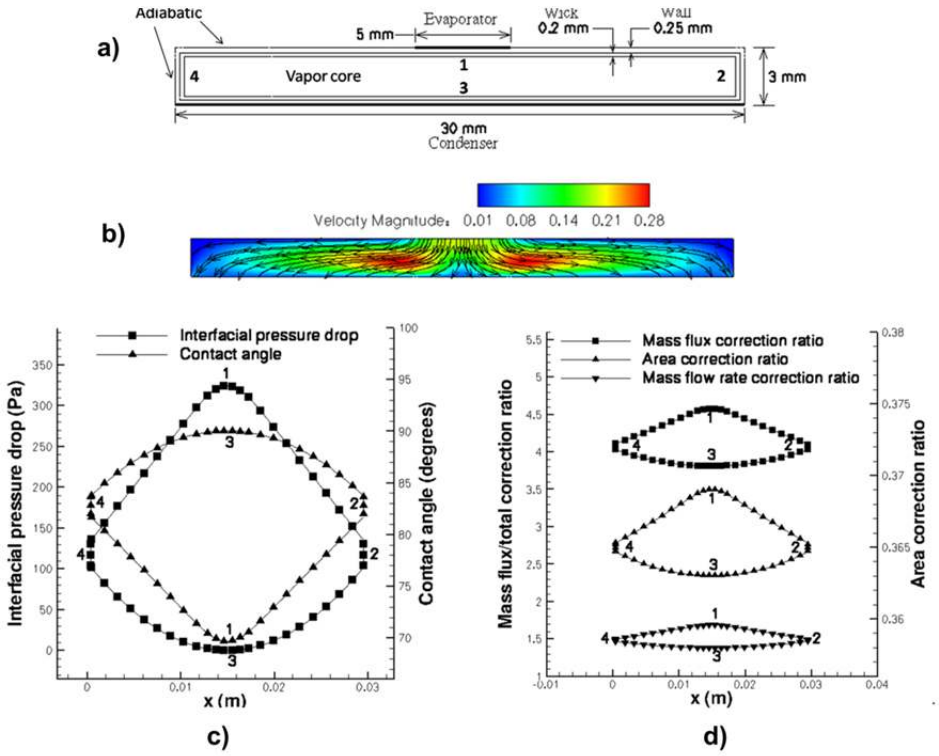

Figure 26. (a) Schematic diagram of the vapor chamber modeled in [160]. (b) Velocity contours are shown for an input heat flux of 10 W/cm^2 and an accommodation coefficient of 1. (c) Interfacial capillary pressure drop and (d) local contact angle mass flux, area, and mass flow rate correction ratios along the liquid–vapor interface are shown for the same case [160].

3.3.2 Boiling In the Wick Structure

For experimental validation, modeling tools must accurately capture the performance of ultra-thin vapor chambers over the full range of operational conditions. Nucleate boiling in the wick structure has been observed at high heat fluxes under simulated conditions [37] and in testing of actual devices [81]; however, extant modeling approaches (Section 3.1) do not capture this behavior.

One potential strategy for capturing boiling effects in a device-scale vapor chamber model is to couple it to a direct simulation of bubble departure from a microporous-coated heated wall (in an analogous manner to the microscale evaporation model coupling described in [160]). As discussed by Dhir [161],measurement difficulties, prediction inaccuracies, and lack of generality associated with the effort to correlate nucleate boiling mechanisms over the last half of the twentieth century, *viz.* nucleation site density, bubble departure diameter, and bubble departure frequency, has spurred recent investigation of direct simulation of vapor bubble growth during nucleate boiling from flat surfaces [162-169]. Reports of similar approaches in the presence of porous structures are limited.

Ranjan *et al.* [170] investigated the formation of two-phase flow structures and vapor growth in a two-dimensional porous matrix using a validated volume of fluid-continuum surface force (VOF-CSF) numerical model. In contrast to boiling from a smooth surface, discrete bubbles do not depart from the porous matrix, and instead form continuous dendritic vapor columns due to the increased wall adhesion area that is not overcome by buoyant forces. Under these conditions, while decreasing porosity increases the phase-change heat transfer rate due to increased thin-liquid film area, the increased vapor flow pressure drop may cause dryout at a lower heat flux [170]. The formation of continuous vapor columns in a high-porosity anisotropic matrix (Figure 27) mimics the mechanistic behavior proposed by the Smirnov correlation [74] evaluated in Section 2.3. A similar conduction-based equivalent fin heat transfer model was proposed by Ranjan *et al.* [170] and used to determine an optimum particle size to wick thickness ratio based on the fin efficiency, which agreed with prior experimental observations by Chien and Chang [60] and Webb [61]. Li *et al.* [171] visualized boiling from close-packed glass and copper spheres and compared the results against a volume-of-fluid numerical model of the same configuration. In both experiments and simulations, similar vapor column structures were observed at medium heat fluxes, which broke apart due to hydrodynamic instability caused by countercurrent liquid flow to the heated surface. The vapor columns only broke apart once liquid flow to the surface was insufficient to maintain new vapor mass flux to support the columns [171].

[Insert Fig27.tif here 1/2-page width]

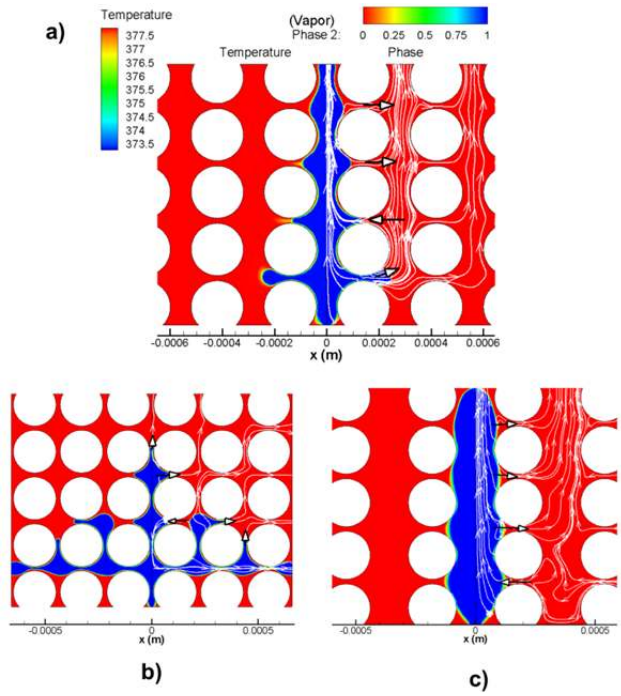

Figure 27. Temperature (K) and phase contours in the fluid domain for vapor generation from a heated surface covered with an anisotropic porous matrix composed of 100 µm particles. Cases shown have particle pitches of (a) 280 µm (b) 220 µm, and (c) 360 µm ($\Delta T_{superheat}$ = 5 K, T_{sat} = 373 K) [170].

The potential for complete numerical modeling of boiling heat transfer is supported by good agreement with data obtained from surfaces with single or multiple controlled nucleation sites [163,172]; however, further computational advancements are required to predict nucleate boiling in complex three-dimensional geometries, particularly at high heat fluxes when vapor-liquid interfaces evolve rapidly. To obtain reasonable comparison against experimental vapor chamber performance data for conditions that result in boiling in the wick structure, Ranjan *et al.* [173] adopted a semi-empirical approach to model boiling conditions at high heat flux inputs. The foundational numerical model was adapted from [160], as described in Section 3.3.1. In the model, nucleate boiling was assumed to occur over the spatial extent where the local wick temperature exceeded a prescribed incipience superheat. Based on the experimental observations of Weibel *et al.* [37], the conduction thermal resistance was bypassed over this area, and an empirical boiling heat transfer coefficient was instead imposed. As shown in Figure 28, this approach yielded good agreement with experimental thermal resistance data obtained for a vapor chamber heat spreader [81] at heat fluxes up to 500 W/cm^2.

[Insert Fig28.tif here 1/2-page width]

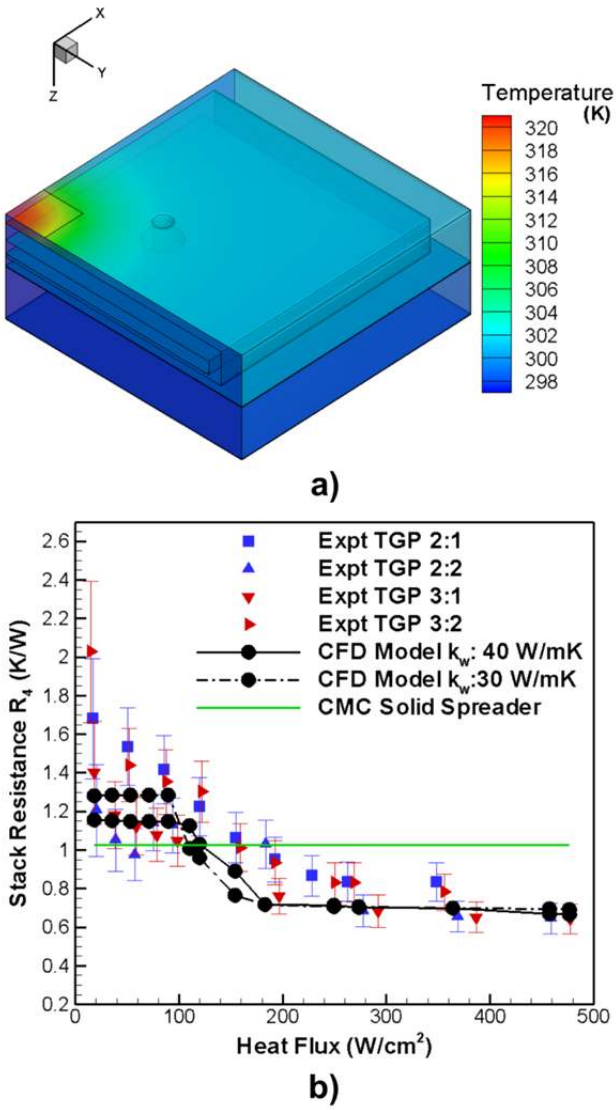

Figure 28. (a) Temperature contours on the outer surfaces of the thermal ground plane (TGP) vapor chamber model for an evaporator heat flux of 89 W/cm^2 and two different values of wick thermal conductivity, and (b) comparison against experimental data up to 500 W/cm^2 for vapor chamber devices and a CuMoCu (CMC) solid heat spreader [173].

3.4 Design and Development of Ultra-thin Vapor Chamber Devices

Advances in experimental and computational wick structure characterization and device-modeling approaches have enabled the recent design, development, and optimization of ultra-thin vapor chamber heat spreader devices. The need for flat, thin (~1 mm) vapor chambers with low coefficient of thermal expansion (CTE) (5-7 ppm/K) and high effective conductivity (> 1000 W/mK) has recently emerged for effective proximate heat spreading from emerging high power (> 100 W/cm^2) microelectronics devices. In current state-of-the-art electronics packages, the microelectronic components are directly mounted on low-CTE solid heat spreaders. Direct mounting of

microelectronic components to vapor chamber heat spreaders composed of CTE-matched materials could serve as a comparatively higher effective conductivity 'thermal ground plane' (TGP) without compromising the package form factor or functionality. This section reviews recent developments in ultra-thin vapor chamber heat spreaders with these functional performance targets set by the Defence Advanced Projects Research Agency (DARPA) and supported through significant grant funding.

3.4.1 Radio Frequency Thermal Ground Plane (RFTGP)

A collaborative research effort led by Raytheon Company pursued the development of a Radio Frequency Thermal Ground Plane [174] composed of a copper-molybdenum-copper casing with micro/nanostructured sintered copper powder wick structures, as depicted in Figure 29a. Altman *et al.* [81] developed an experimental facility to test RFTGP devices with monolithic [37], micropatterned [43], and CNT-coated [51] sintered powder evaporator wick structures. Performance of the 30 mm × 30 mm × 3 mm vapor chamber was directly compared to a solid copper-molybdenum heat spreader of equivalent external dimensions for a hot spot heat input area of 5 mm × 5 mm (up to 500 W/cm^2). Incipience of boiling in the vapor chamber was shown to be the critical transition at which boiling-dominated heat transfer realized improved relative performance. Based on comparisons to direct measurement of the thermal resistance associated with boiling from monolithic sintered powder wick structures [37], it was concluded that the evaporator thermal resistance governed the overall vapor chamber thermal resistance, and hydrophobic nanostructures on the internal condenser surface did not alter the overall performance. Of the various enhancement features explored, hydrophilic copper-functionalized carbon nanotubes displayed an ability to shift the critical boiling incipience transition to a lower wall superheat [81] (as further discussed in Section 4.2.2).

The measured overall vapor chamber thermal resistance was observed to be a strong function of the input heat flux and internal saturation pressure/temperature [81]. This correlation was further explored by Ranjan *et al.* [173] using the numerical vapor chamber model as described in Section 3.3.2, which was calibrated to the RFTGP experimental test data from [81]. The numerical model was used to explore the design of a 1 mm overall thickness vapor chamber device. It was observed that the thermal resistance of the vapor core (due to the saturation pressure/temperature gradient) becomes increasingly important at reduced thicknesses. Thereby, water vapor thermophysical property variations lead to non-linear device thermal resistance behavior with linearly varying input heat flux and external condenser temperatures [173]. A parametric variation of the relative wick and vapor core thicknesses concluded that

the minimum wick thickness should be selected such that a capillary limit is not reached at the desired operating heat flux in order to reduce the evaporator and vapor core thermal resistances.

3.4.2 Micro/Nanostructured Thermal Ground Plane (TGP)

A 30 mm × 30 mm × 3 mm vapor chamber thermal ground plane (Figure 29b) was recently designed, fabricated, and tested in an effort led by researchers at GE Global Research [175,176]. Device performance is extremely sensitive to small variations in the amount of initial fluid charge at this form factor; over-filling floods the condenser and under-filling may lead to premature dryout. Hence, a fluid charging station with demonstrated accuracy of ± 2 μl was developed to evacuate and backfill prototype vapor chambers using a series of graded resolution burettes [175]. A thermal characterization facility was designed to generate 30 mm × 10 mm heat source and heat sink areas on opposite ends of the vapor chamber. An effective thermal conductivity metric was defined based on the temperature drop associated with equivalent two-dimensional heat spreading in a solid material of known conductivity, and an uncertainty analysis was used to determine the required temperature measurement accuracy [175].

To ensure device performance under adverse gravitational forces, de Bock *et al.* [176] developed device thermal performance and capillary limitation models based on an effective thermal resistance network and simplified expressions for liquid/vapor-phase pressure drop, respectively. In order to ensure dissipation of the desired heat load against an exerted body force 10 times normal gravity, it was found that the properties of a sintered powder wick with 75 μm particle diameters [136,140] would avoid the capillary limitation [176]. The effective thermal conductivity of 3 prototype vapor chambers was measured as a function of the gravitational body force by mounting on a centrifuge spin table. The thermal resistance change was negligible due to the minimal additional vapor pressure drop imposed at the maximum gravitational loading. The same prototype devices were tested as a function of input heat flux, and under certain operating conditions exceeded the effective thermal conductivity of copper at an adverse body force 10 times gravity [176].

[Insert Fig29.tif here full-page width]

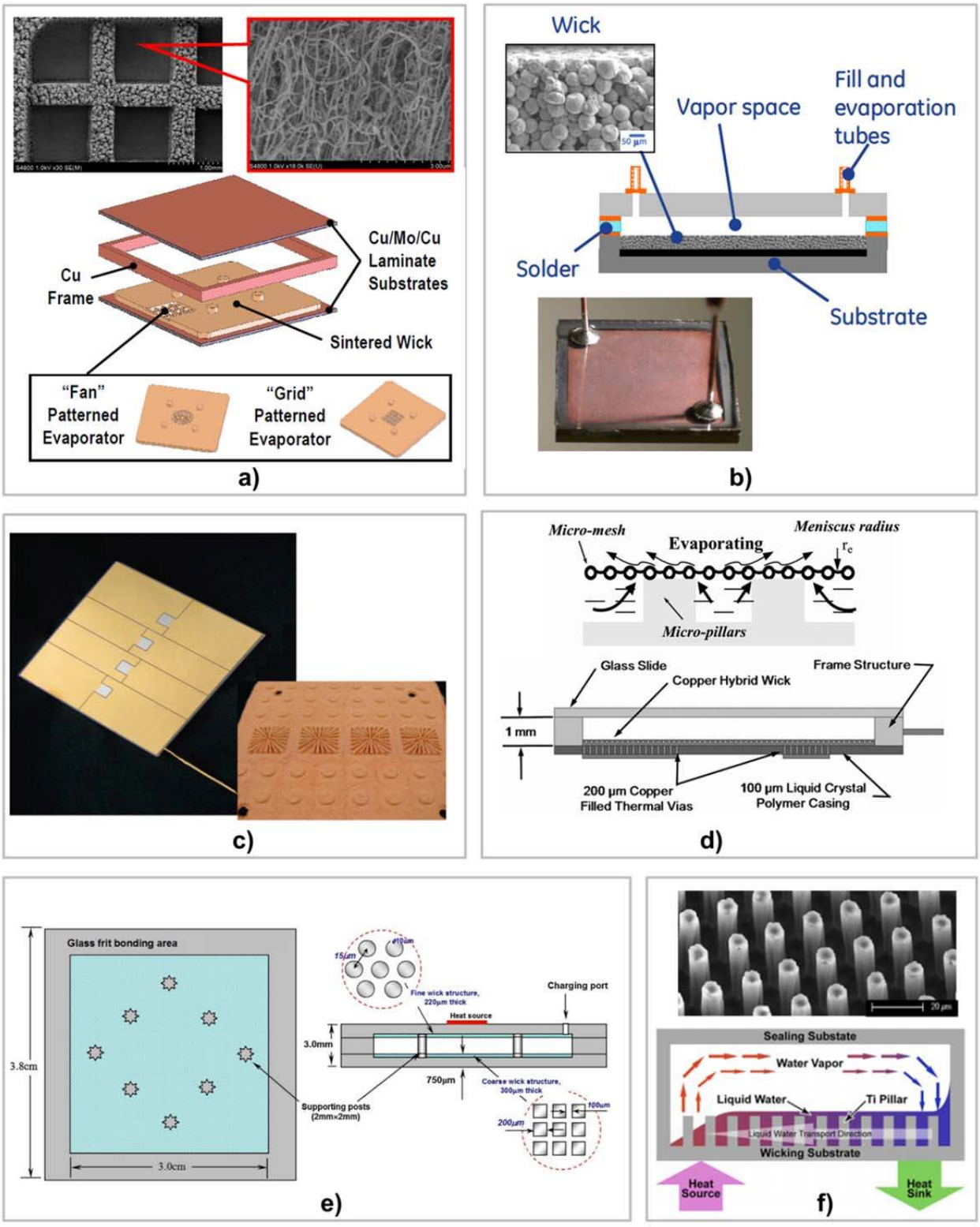

Figure 29. Diagrams and images of several recently developed low coefficient of thermal expansion vapor chamber thermal ground planes for direct mounting of microelectronic devices including (a) a Radio Frequency Thermal Ground Plane [81], (b) a micro/nano thermal ground plane with sintered powder [175], (c) an aluminum nitride vapor chamber

[42], (d) a Polymer-based Flat Heat Pipe [181], (e) a silicon thermal ground plane [188], and (f) a small-scale Titanium Thermal Ground Plane [189].

3.4.3 Planar Vapor Chambers with Hybrid Evaporator Wicks

Thin vapor chamber prototypes have been recently developed based on the design and testing of biporous wick structures and arterially fed evaporators as previously discussed in Section 2.1.3 and Section 2.2, respectively. Prior testing of biporous sintered powder wick structures [35,36] simulated saturated vapor conditions, but unlike realistic devices, left a large open vapor space above the wick structure during boiling. Recent investigations by Catton and coworkers [177-179] attempted to reconcile this difference by testing biporous wick structures with a vapor restriction plate placed directly over the sample. In this way, the test facility provided an improved representation of vapor chamber performance based on the device thickness and lateral vapor pressure drop. Experimental results were compared directly to the thermal resistance incurred in prototype vapor chamber thermal ground planes having the same internal wick structure and heat input area. The thermal resistance due to vapor pressure drop was significant for thin vapor chambers, and use of a vapor restriction plate in a capillary-fed evaporation/boiling test facility provided excellent agreement with vapor chamber device testing [179].

Ju *et al.* [42] explored a low-CTE vapor chamber envelope composed of aluminum nitride ceramic plates (with direct-bonded copper layers for water compatibility) spaced apart by a Kovar ring. Several wick structures were considered based on preliminary sub-device testing, *viz.* biporous sintered powder [36], lateral converging liquid return arteries [41], and vertical columnar arteries [67], but lateral arteries were ultimately chosen for their mechanical robustness [42]. A 100 mm × 100 mm prototype vapor chamber was constructed to accommodate an array of four 10 mm × 10 mm heat input areas for the potential thermal management of vertical cavity surface emitting laser (VCSEL) arrays, as shown in Figure 29c. The vapor chamber prototype was demonstrated to dissipate a total of 1500 W prior to dryout, and capable of supplanting lower-reliability microchannel heat sinks currently used for this application [42].

3.4.4 Polymer-based Flat Heat Pipe (PFHP)

A collaborative research effort led by the University of Colorado Boulder aimed to develop ultra-thin polymer-based flat heat pipes (PFHP) amenable to fabrication via high volume manufacturing technologies. A hybrid (biporous) structure served as the capillary wick in a series of prototype heat pipe devices; design of this wick structure is described in [180]. The hybrid wick was composed of a fine copper mesh (intended to enhance local

evaporation/condensation) that was sintered to a grooved copper surface (intended to provide liquid return at minimal flow resistance). Modeling efforts showed that this structure could provide a significant improvement in maximum heat transport capability compared to a homogeneous copper mesh [180]. A first generation 100 mm × 30 mm × 2.5 mm all-copper flat heat pipe was fabricated to demonstrate the effectiveness of the hybrid wick structure. Based on the evaporator-to-condenser temperature difference, and the device cross-sectional area, testing demonstrated that an effective thermal conductivity greater than 10,000 W/mK could be achieved for a heat input of 91.3 W over a 25 mm × 25 mm area (14.6 W/cm^2) [180].

Subsequent investigations by Oshman *et al.* [181,182] focused on development of flexible polymer-based heat pipes. A liquid-crystal-polymer (LCP) casing material was chosen for chemical resistance, customizable low CTE, hermeticity, and compatibility with flexible printed circuit board manufacturing processes. In order to increase the inherently low polymer thermal conductivity, copper thermal vias were inserted into the LCP at the heat input and condenser locations. A detailed description of thermal via insertion and fabrication of the copper hybrid wick structure for LCP heat pipe walls is provided in [181]. A prototype PFHP (60 × 30 × 1 mm^3) was fabricated using these techniques (Figure 29d). Using the same definition above, the maximum effective thermal conductivity was measured to be 830 W/mK over an input power range of ~3-12 W/cm^2 [181]. Using the same fabrication approaches, a 40 × 40 × 1 mm^3 PFHP was later fabricated with different heat input and condenser configurations [182]. For heat fluxes above ~30 W/cm^2, testing showed a favorable reduction in thermal resistance compared to pure copper.

3.4.5 Silicon Thermal Ground Plane (TGP) Vapor Chamber

Silicon micro heat pipes generally are described by an embedded array of discrete parallel non-circular channels that each behave as a two-phase evaporation/condensation loop to increase the inherent thermal conductivity of silicon [183-185]. Several investigations have also developed planar vapor chambers composed entirely of silicon with axially-grooved wick structures [186]. Recently, researchers at Teledyne Scientific & Imaging Company developed and tested all-silicon planar vapor chambers with micropillared wick structures for spreading heat from high flux hot spots [187,188].

Cai *et al.* [187] fabricated a flat hexagonal vapor chamber based entirely on silicon photolithography, dry etch, and wafer bonding processes. The 2 mm thick vapor chamber had a hexagon edge length of 10 mm (total surface area of ~ 2 cm^2). The hexagonal shape was motivated by the ability to link together multiple 'hexcell' chambers for both

bulk fabrication throughput and improved spreading from an array of heat sources. A parametric optimization of the structural design was performed to ensure mechanical integrity at the internal vapor pressures encountered at 135 °C. A tradeoff between reduced vapor flow area and maximum operating pressure resulted in the placement of six posts along lines bisecting the hexagon edges [187]. Operating pressure tolerance and hermitic sealing was demonstrated after bonding the upper and lower silicon chamber walls. While thermal spreading performance of a sealed device was not tested, separate capillary-fed boiling testing of the pillared silicon wick was shown to dissipate 300 W/cm^2 from a heat source area of 2 mm × 2 mm at 35 °C superheat [187].

In a later study, Cai *et al.* [188] developed a square 38 mm × 38 mm × 3 mm thermal ground plane vapor chamber (Figure 29e) using several similar fabrication procedures. On the internal condenser side, a coarse-pillared silicon wick was used to facilitate liquid return to the evaporator via posts that also provided structural integrity. A finer silicon pillared wick (10 μm diameter, 15 μm pitch) was used on the evaporator side to provide the necessary capillary pressure to sustain operation under adverse gravitational loading. A novel three-layer silicon wafer-stacking fabrication process was employed to increase device yield by reducing the required silicon wick etch depth on each wall compared to a two-wafer stack. Thermal testing of the vapor chamber was performed with heater (30 mm × 4 mm) and condenser (30 mm × 5 mm) areas at opposite ends of the vapor chamber. Performance of initial prototype devices was highly sensitive to liquid charge and noncondensible gases, leading to a large range of measured effective thermal conductivities (~900-2500 W/mK). Charge optimization led to a maximum measured device effective thermal conductivity of ~2700 W/mK [188].

3.4.6 Titanium Thermal Ground Plane (Ti-TGP)

Researchers at the University of California Santa Barbara explored fabrication of all-titanium vapor chambers [189,190]. Relative to other potential materials, titanium offers excellent corrosion resistance, light weight, high fracture toughness, and can be used as the substrate for microfabrication of high-aspect-ratio wick features [191].

Ding *et al.* [189] fabricated a proof-of-concept device having external dimensions of 30 mm × 30 mm × 0.6 mm for thermal ground plane applications (Figure 29f). The internal wick structures were titanium pillars (10 μm diameter, 15 μm pitch) oxidized to form secondary nanostructured titania (NST) surface features (fabrication details in [189]). Transient wetting behavior of the wick structure was shown to behave in accordance with Washburn dynamics [192], and the NST surface increased the wetting velocity. The vapor chamber was sealed along the edge by local laser welding to avoid heating the entire device to the necessary processing temperatures. By applying a fixed

temperature difference between evaporator and condenser sections, the fabrication proof-of-concept device achieved a maximum effective thermal conductivity of ~350 W/mK at this form factor [189].

A large-scale titanium thermal ground plane (300 mm × 76 mm × 4.5 mm) with 24 individual heat source mounting locations was later fabricated using the same fabrication techniques [190]. Unlike the small-scale Ti-TGP, which used an array of microfabricated pillars, the large-scale device consisted of a groove wick with nanostructured titania. The groove structure was optimized to maximize the heat transport capability (by equating the capillary pressure with pressure losses) and for a device in a vertical reflux orientation. Effective device thermal conductivities of 5000-8000 W/mK were measured based on the effective working length during simulated testing of the large-scale Ti-TGP using 8 independent heat sources; total heat dissipation was 500 W and 1000 W at evaporator temperatures of 100 °C and 150 °C, respectively [190].

4 Nanostructured Capillary Wicks for Vapor Chamber Applications

Advances in controllable synthesis techniques continue to further enable the use of nanostructures in numerous engineering applications that exploit their tunable geometric, thermal, and mechanical properties. Nanostructures such as carbon nanotubes (CNT) and metal nanowires (NW) have been evaluated for use as vapor chamber capillary wick structures owing to a number of potentially advantageous characteristics.

Conduction through the wick layer often imposes a significant thermal resistance during vapor chamber operation. The intrinsically high thermal conductivity of CNTs determined both theoretically [193,194] and experimentally [195-198] may be exploited, and has previously led to a reduction in the resistance to heat flow at interfaces between components [199-202] and a development of novel composite materials with increased thermal conductivity [202-204]. The pores of nanowire arrays also have a high capillary pressure; however, their relative impermeability compared to microscale wick structures must be carefully assessed in the design process. Further, while the hydrophilicity of NWs and CNTs with water has been reported in the literature [205,206], aligned arrays of nanotubes have also been shown to behave as superhydrophobic surfaces [207]. Hence, surfactants may be used for liquid conveying applications [208], or nanostructures may be functionalized for heat transfer applications via metallization [51], hydrochloric acid treatment [209], or ultraviolet excitation [210]. Nanostructures have a high number of pores per unit substrate area, and thereby may also offer an increase in the thin-film area for evaporation.

Nanostructures have been reported to improve differing aspects of the boiling process (*e.g.*, incipience, nucleation boiling, and critical heat flux) via CNT-coating of silicon [211-213] and copper substrates [80,213], and copper nanowire [214-216] and silicon nanowire [215-217] surface coatings.

It is important to distinguish and evaluate the potential enhancement provided by nanostructured wicks during capillary-fed evaporation/boiling processes. Recent studies on the design and testing of nanostructured wicks for use in vapor chambers are discussed in this section. Two potential configurations are evaluated: (1) use of nanowire arrays as the primary wicking and evaporation structure, and (2) nanostructured coating of conventional microscale wick structures.

4.1 Assessment and Design of Nanostructured Wicks

In order to determine the viability of nanowick structures for use in vapor chambers, the morphology dependence of capillarity, permeability, and thermal resistance must be determined. Ranjan *et al.* [218] developed theoretical and numerical models to approximate these quantities for representative aligned vertical cylinders in hexagonal and square packing arrangements.

The capillary pressure was determined by obtaining the mean curvature of the liquid meniscus formed in a nanowick (as in [153]), while permeability was estimated by simulating the pressure drop associated with flow through a two-dimensional unit cell (Figure 30a,b). For this analysis, wetting contact angles were assumed based on the observations of Rossi *et al.* [219] and Kim *et al.* [220], and continuum approximations for capillary dynamics [220], surface tension [221], and viscous drag [222] were shown to be justified. Properties were obtained as a function of nanowire diameters and number densities consistent with typical fabrication processes [223-225].

[Insert Fig30.tif here 3/4-page width]

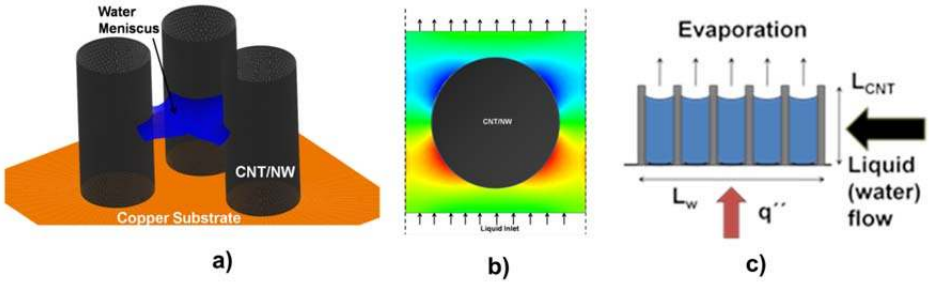

Figure 30. (a) Shape of the water meniscus in the nanopore formed between square-packed vertically aligned cylinders and (b) pressure contours shown in the liquid region around a cylinder (which are used to compute the nanowick permeability). (c) Two-dimensional representation of wicking length, L_w, across the nanowire array with input heat flux q'' [218].

4.1.1 Nanowire Array Wicks

Ranjan *et al.* [218] considered evaporation from a uniform nanowire array fed by capillary action. The evaporative resistance of the liquid meniscus formed in the array was computed numerically using the previously developed model discussed in Section 3.2.3 [155]. The thermal resistance of the nanowick, which is governed primarily by conduction resistance through the height of the saturated porous structure, is potentially orders of magnitude lower than typical sintered copper powder or screen wicks.

While it is clear that nanowicks may outperform conventional wick materials purely on the basis of thermal resistance, the capillary pressure generated must sustain liquid flow to the meniscus at the desired heat load. A wicking length was used to assess the feasibility of nanowick structures in this regard, and was defined as the maximum length over which a given mass flow rate (*i.e.*, heat load) can be transported through the wick structure via capillary action [218], as shown in Figure 30c. Analysis as a function of nanowire density found that the maximum wicking length occurred at a non-dimensional pitch of 5 due to the tradeoff between capillary pressure and permeability; however, the maximum wicking lengths were only on the order of 1 cm even for modest heat loads due to the low permeability of the structure. This suggested that use of nanowick arrays over a large area on a heated smooth substrate would perform poorly [218].

Due to these inherent capillary transport limitations, Weibel *et al.* [226] proposed evaporator surfaces composed of nanowire arrays fed by interspersed conventional microscale wick structures. Design of such wicks required a study of the trade-offs between the greater permeability offered by conventional wick structures and the reduced thermal resistance offered by a nanowire array. The geometry selected for parametric investigation was a series of alternating wedges of microscale and nanoscale wick layers (Figure 31). A numerical model was developed to analyze fluid flow and regions of dryout in the evaporator using estimated inputs for the capillarity, permeability, and effective thermal resistance of each region. The proposed evaporator structure was compared to a conventional homogeneous microscale wick, and thermal resistance was found to be significantly reduced when sufficiently short wicking lengths within the nanostructured regions were ensured by geometric design [226].

[Insert Fig31.tif here 1/2-page width]

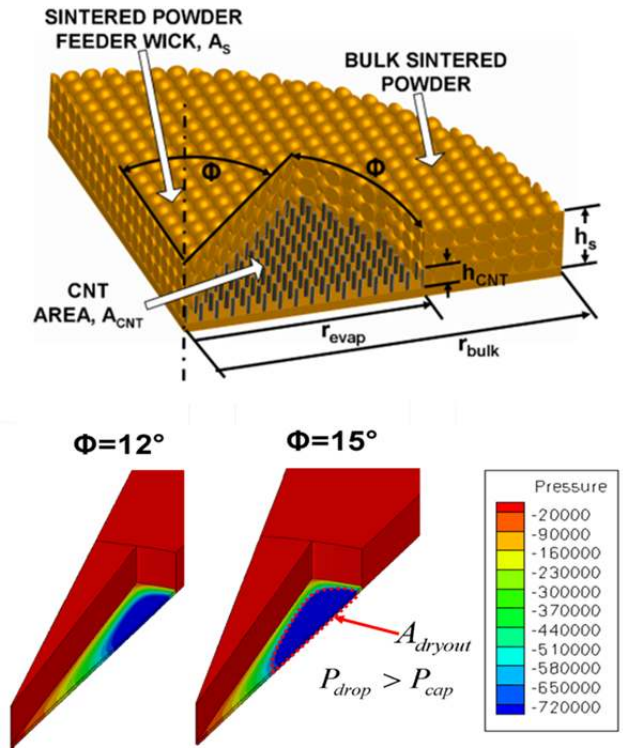

Figure 31. Schematic diagram of the wedge geometry chosen for the integrated evaporator wick structure and example pressure contours (in Pa) in the nanowire domain with respect to a zero pressure inlet condition for varying wedge angle, *Φ*.

4.1.2 Nanostructured Coatings

An alternative wick design is to directly coat conventional wick microstructures with nanostructures in order to increase wettability and total thin-film area for enhanced evaporation heat transfer. This approach has been previously used to increase the capillarity of titanium [189] and copper [48] micropost wick structures.

Ranjan *et al.* [218] studied the case of a high-permeability sintered copper powder wick coated with nanowires, and employed simplified theoretical and numerical models to estimate the potential thermal performance enhancement via nanostructuring. Two extreme cases are presented in Figure 32a: (1) completely non-wetting nanowires that only serve to alter the local meniscus shape near the liquid-solid contact line formed in the microstructure, and (2) nanowires with a sufficient wicking length to coat the entire microscale particle with a thin liquid layer. An increase in the thin-film meniscus area due to the presence of nanowires is estimated based on the resolved 3D meniscus shape, and the thermal resistance is computed using a simplified network model. Figure 32b shows the reduction in

wick thermal resistance for multiple liquid fill heights in the pore. Both wetting and non-wetting nanowires are predicted to reduce the thermal resistance (by a maximum of 14% for the most optimal configuration) [218].

[Insert Fig32.tif here 1/2-page width]

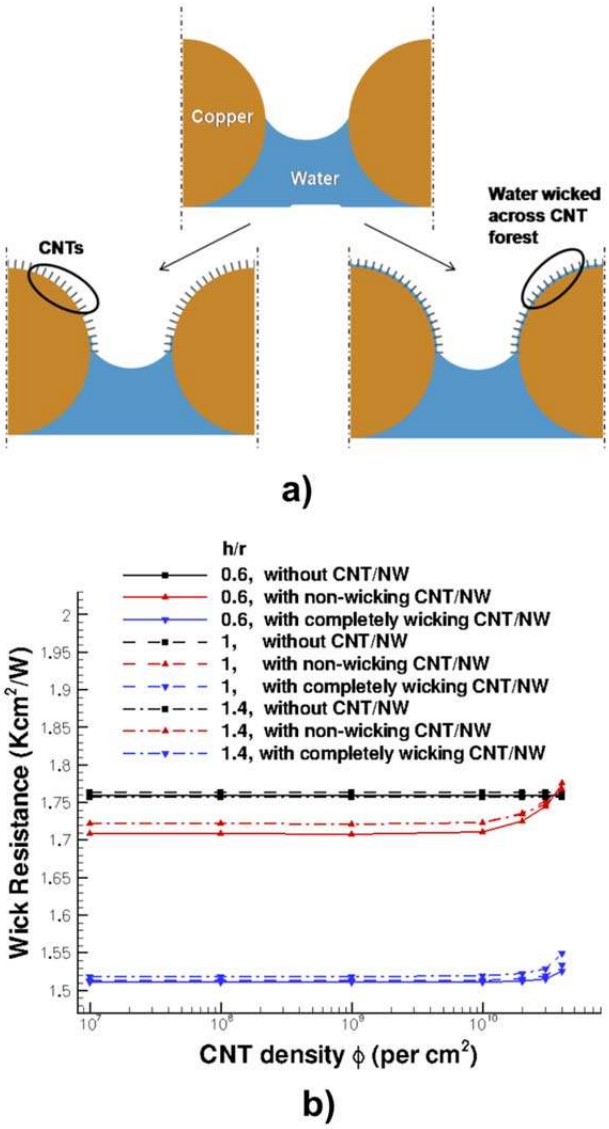

Figure 32. (a) Illustration of nanowire-coated spherical particle (2D representation of 3D model; not to scale) for extreme cases of completely wetting and non-wetting nanostructures, and (b) thermal resistance network model results plotted versus nanowire number density for multiple liquid levels in the microscale pore [218]

4.2 Experimental Evaluation of Nanostructured Wicks

Informed by the expected wetting behavior of low-permeability nanostructures, several novel evaporator structures composed of patterned nanowire arrays and nanostructure-coated wicks have been fabricated in the literature. In this section, several experimental studies are reviewed that evaluate the potential thermal performance enhancement provided by nanostructured wicks.

4.2.1 Nanowire Array Wicks

In a pair of studies conducted by Weibel *et al.* [50,227] sintered powder wick structures with an array of interspersed 1 mm × 1 mm square regions of carbon nanotubes (CNT) were investigated. The sintered powder structure was composed of 100 μm copper particles, and two different wick thicknesses were evaluated, 1 mm and 200 μm. The CNTs were grown in a microwave plasma chemical vapor deposition (MPCVD) system following deposition of metal catalyst layers (Ti/Al/Fe), where Fe provided active growth sites for the CNTs. Details of the CNT growth procedure are provided in [228]. The samples were functionalized by coating the CNTs with a thin layer of evaporated copper via physical vapor deposition, making the CNT surface hydrophilic. Images of the copper-coated CNT structures interspersed within a 200 μm-thick sintered powder sample are shown in Figure 33. Samples without CNT structures were also prepared as a baseline for comparison.

[Insert Fig33.tif here 1/2-page width]

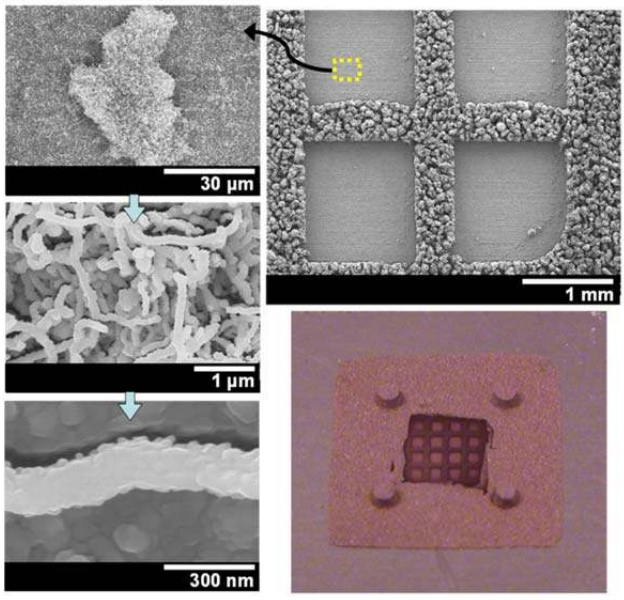

Figure 33. Images of a 200 μm-thick sintered copper powder wick with interspersed CNT array regions [50]. Low-magnification images on the right show the complete sample (bottom) and macroscale patterned features (top). The series of increasing magnification SEM images on the left show the CNT growth morphology that occurs in the patterned recesses.

Experimental evaluation of capillary-fed evaporation/boiling was performed in the experimental facility described in Section 2.1.1. For the 1 mm-thick sintered powder sample, an array of 1 mm × 1 mm square recesses improved performance in the boiling regime due to the reduced resistance to vapor exiting the wick structure, as described in Section 2.2; however, addition of the CNT array did not alter performance in the boiling regime because the square regions remained largely flooded during operation [227]. Conversely, for the 200 μm-thick sintered powder wicks, the CNT regions were observed to form a thin-liquid film that receded at high heat fluxes during intense evaporation. The CNT array extended the dryout heat flux compared to the baseline samples [50].

Cai *et al.* [45] investigated a CNT 'biwick' structure composed of a uniform 250 μm-thick CNT array with parallel interspersed microgrooves. It was postulated that the nanoscale pores of the CNT array would provide a large increase in the area for thin-film evaporation and boiling heat transfer, while the groove spacing would provide area for bulk liquid supply and vapor removal. The wick structure was fabricated by using lithography processes to define the catalyst deposition area and resulting CNT growth pattern. An acid-treatment process was used to make the CNTs hydrophilic [45]. The structures tested had 100 μm-wide CNT strips with 50 μm-wide microgrooves. A 2 mm × 2 mm platinum heater was fabricated on the back side of the silicon growth substrate, and the capillary-fed evaporation/boiling performance was evaluated in open and saturated vapor environments. A maximum heat flux of ~600 W/cm^2 was measured at surface superheats of only 35-45°C [45].

Subsequent studies by Cai *et al.* [46,47] investigated additional CNT biwick morphologies with parallel CNT stripes, zig-zag CNT stripes, and hexagonally packed CNT clusters, as shown in Figure 34. Thermal testing was performed in a saturated environment using two different heat input areas, 4 mm^2 and 100 mm^2. The CNT biwick morphologies performed similarly, and a larger dependence on the heater size was noted: While maximum heat fluxes approached 1000 W/cm^2 for the 4 mm^2 heat input area, this was reduced to under 200 W/cm^2 for the 100 mm^2 heat input area across all sample morphologies tested (see Section 2.5 for additional discussion) [46,47].

[Insert Fig34.tif here 3/4-page width]

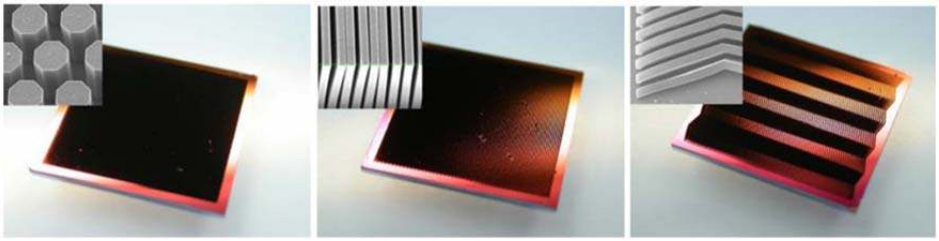

Figure 34. CNT biwick composed of cylindrical CNT clusters, straight CNT stripes, and zig-zag CNT stripes (from left to right) [47].

4.2.2 Nanostructured Coatings

Nanostructured coatings can improve the capillary-fed thermal performance of wicks by potentially increasing the wettability and surface area for evaporation. Nam *et al.* [48] evaluated the thermal performance of a nanostructured copper wick by submerging the lower edge of a sample into a pool of water, and allowing liquid replenishment by capillary action to a 5 mm × 5 mm heated area located above the pool. A controlled oxidation process was used to create needle-like CuO nanostructures on top of copper microposts. The fabrication details and demonstration of superhydrophilic wetting characteristics after oxidation are described in [49]. Samples with and without CuO nanostructures were directly compared. The nanostructures provided little improvement below 25 W/cm^2, but improved capillary performance provided by the nanostructure prevented local dryout of the post surfaces, and reduced the surface superheat at higher heat fluxes relative to the uncoated case. This improved capillary performance outweighed any conduction resistance added by the nanostructure layer. A 70% increase in the maximum dryout heat flux was shown for the nanostructured wick samples [48].

Kousalya *et al.* [51] explored a means of increasing the dryout heat flux by fabricating carbon nanotubes (CNT) on a 200-μm thick sintered copper powder wick. A physical vapor deposition process was used to coat the CNTs with copper to promote their wettability to water. Three different increasing nominal thicknesses of copper were investigated (Figure 35). Unlike aligned CNT growth on a flat substrate, the randomly oriented CNTs grown on sintered powder lend themselves to a more conformal copper coating by physical vapor deposition. The nanostructured samples were compared to a bare sintered powder wick using the capillary-fed evaporation/boiling facility described in [37].

[Insert Fig35.tif here 3/4-page width]

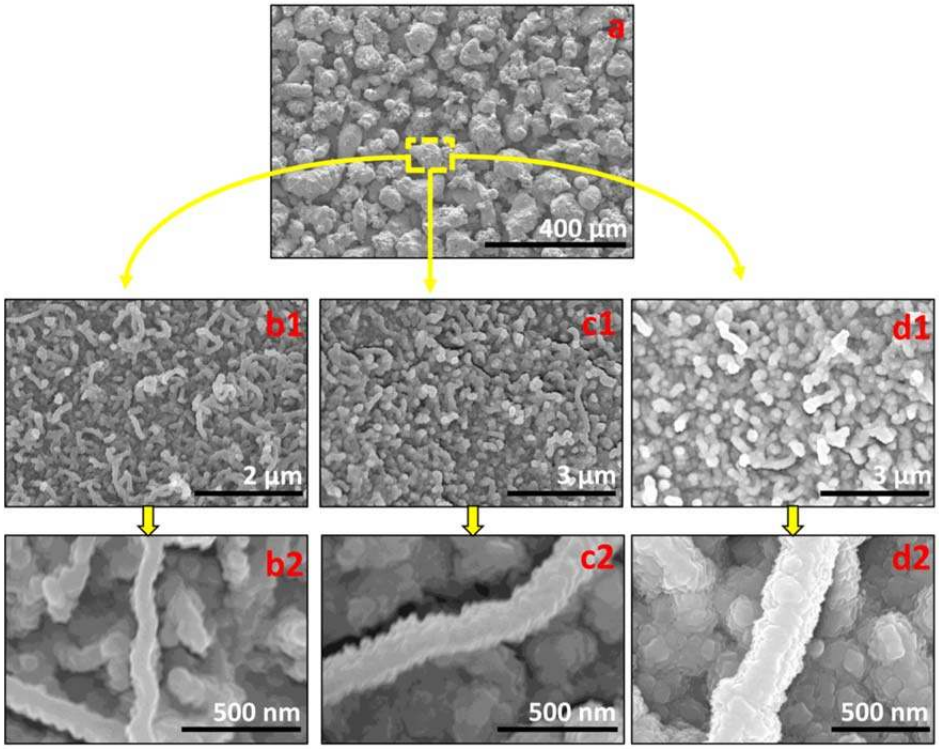

Figure 35. (a) A low-magnification SEM image of CNT-coated sintered powder, and (b-d) medium- and high-magnification SEM images (middle and bottom row, respectively) of CNT-coated sintered powder functionalized with increasing nominal copper coating thickness (from left to right) [51].

As discussed in Section 2.4, an abrupt transition from evaporation to boiling occurs at relatively large surface superheats (~10 °C) for bare sintered copper samples, resulting in a noticeable transient substrate temperature drop; however, Kousalya *et al.* [51] observed that the CNT-coated samples exhibited an earlier transition to the boiling regime. Weibel *et al.* [50] drew comparisons between the incipience behavior of bare and CNT-coated samples (fabricated using the same techniques as in [51]) using a more extensive set of 25 boiling curves. The CNT coating was able to reduce the mean surface superheat at incipience by 5.6 °C compared to uncoated samples [50]. Despite this observed behavior, conventional nucleation theory suggests that cavities formed by nanoscale pores would require very large superheats to become active due to the inverse relationship between cavity radius and required activation superheat [59]. Therefore, the mechanism by which CNTs reduce the incipience superheat for capillary wicks may be attributed to: 1) an increase in the microscale thermal boundary layer as occurs in flow boiling [229], or 2) changes to the wetting characteristics of the existing microscale cavities in a manner that reduces the required

superheat. For example, Li *et al.* [214] proposed that a nanorod coating increases the stability of a microcavity vapor embryo during pool boiling by feeding it with vapor trapped in the nanoscale pores.

Following boiling incipience, Kousalya *et al.* [51] observed a dryout heat flux of 437 W/cm^2 at a surface superheat of 23.3 °C for the bare sintered powder sample. For the CNT-coated samples, an increasing copper coating thickness consistently diminished the area of partial dryout visualized during testing; the maximum dryout heat flux was increased compared to the baseline for the thickest coating [51]. The authors concluded that dryout occurred due to a capillary limit because the estimated value of the maximum critical heat flux constrained by hydrodynamical instabilities was predicted to be much higher than experimental observations. It was proposed that the CNTs functionalized with a thicker copper coating enhanced the surface wettability, and thereby increased the dryout heat flux. Since a static macroscopic contact angle cannot be obtained for a porous sintered copper powder structure, a transient measurement of the dynamic contact angle during droplet imbibition was used to assess the relative wettability of the samples [51]. The surface wettability trends matched the trends in the dryout heat flux, as would be expected for a capillary-limited dryout mechanism.

5 Closure

There is an immediate need for high-reliability passive heat spreading away from high-flux hot spots, which currently impose thermal limitations on a number of microelectronics systems. This need has spurred recent advances in fundamental understanding of evaporation and boiling from porous microstructures, and in modeling, design, and manufacture of ultra-thin vapor chamber spreaders. The major advances/developments and critical areas for further study reviewed in the foregoing are summarized here.

The thermal performance of a variety of wick microstructures has been evaluated in terms of their ability to cool a substrate by evaporation/boiling while replenishing liquid to the heat source via capillary action. This has been achieved through novel experimental facilities, and has led to the identification of critical evaporation/boiling regimes and visualization of vapor formation characteristics. It is found that regimes and wick structures that increase interstitial liquid-vapor interface area for heat exchange (*e.g.*, via discrete bubble nucleation with a high departure frequency, or evaporation from continuous vapor columns) provide a significant enhancement compared to evaporation from the top of a wick structure saturated with liquid. Hence, novel heterogeneous wicks having

multiple length-scale pores are proposed and shown to enhance performance by favoring such vapor removal mechanisms. A number of common trends are identified with respect to characteristic wick properties, and approximate models are developed for prediction of thermal performance; however, more knowledge of the vapor flow structures and interstitial liquid film thickness during intense evaporation/boiling is required to enable more generalized and accurate predictive methods.

Due to the severe implications on device performance, many recent investigations focused on studying the critical regime transitions during capillary-fed evaporation/boiling, *viz.* boiling incipience (or lack thereof) and dryout of the wick at high heat fluxes. Compared to pool boiling, even for irregular porous surface morphologies, it is observed that nucleation may be suppressed during evaporation up to a high surface superheat; this is often attributed to meniscus recession and formation of thin liquid films in the porous structure that cannot sustain nucleation. Unfortunately, while suppression of boiling under capillary-fed conditions is observed on an anecdotal basis, prediction of inherently variable incipience criteria requires further statistically significant characterization as a function of wick parameters. Separate investigation of the maximum dissipated heat flux has revealed a strong dependence of capillary dryout on the heater size. While this general trend is anticipated, quantitative predictive methods are nonexistent. Additional investigation is required to develop methodologies for correlating and modeling the complex capillary dryout mechanisms associated with aggressive boiling in the wick structure. Generally, incorporation of nanostructures that behave as superhydrophilic coatings extend the maximum heat flux by increasing the surface wettability and reducing areas of local dryout.

From a device-modeling perspective, the importance of an accurate description of the wick properties as a function of microstructure morphology cannot be overstated. A number of novel direct numerical simulation characterization approaches have been recently developed, and provide higher levels of accuracy/fidelity compared to simplified analytical approximations that are ubiquitously employed in the literature to predict effectively thermal conductivity, permeability, and capillarity as a function of wick morphology. While these approaches provide tools for characterization of both idealized and realistic structures, there is still need for process-based characterization approaches that consider the influence of actual microstructure fabrication techniques in the wick design. Transient, three-dimensional device-level models have also evolved to accommodate drastic alterations in liquid-vapor interface shape as observed during high heat flux operation of vapor chambers. While the potential for direct numerical simulation of vapor departure from a porous wick structure within these models is promising, further

computational advancements are required to predict these phenomena in stochastic wick structures; current approaches still rely on empirical inputs to account for film evaporation or boiling behavior.

The combination of multi-scale design, testing, and modeling advances have informed critical thermal transport limits in passive vapor chamber heat spreaders, which has spawned multiple strategies to break through performance barriers. A set of ultra-thin vapor chambers have been demonstrated for thermal management of high power electronic devices. Device performance trends are accurately captured by companion experimental and numerical modeling efforts, which suggest that passive cooling of millimeter-scale hot spots generating beyond 500 W/cm^2 is feasible. Further characterization and development of methodologies that accurately predict high heat flux operating limits as a function of wick morphology will push performance further.

Acknowledgement

The authors gratefully acknowledge support for this work from industry members of the Cooling Technologies Research Center (CTRC), a National Science Foundation (NSF) Industry/University Cooperative Research Center (IUCRC) at Purdue University, and the Defense Advanced Research Project Agency (DARPA). Special thanks are extended to collaborators David Altman, Timothy Fisher, Arun Kousalya, Jayathi Murthy, Mark North, Ram Ranjan, and Kazuaki Yazawa.

Nomenclature

A	area
$A_{c,p}$	characteristic pore area $(\pi D_p^2/4)$
C	constant
D	particle diameter
D_p	pore diameter $(0.42D)$
h	height
h_{lv}	latent heat of vaporization
k	thermal conductivity
k_{eff}	effective thermal conductivity
K	permeability
$\dot{m}_i''$	mass flux
$\bar{M}$	molecular weight
P	pressure
ΔP	capillary pressure
P_p	characteristic pore perimeter (πD_p)
q''	heat flux
R	thermal resistance, radius of curvature
$\bar{R}$	universal gas constant
t	time
T	temperature
T_{ref}	vapor reference temperature
T_{sat}	saturation temperature
$T_{substrate}$	substrate temperature
ΔT_{sl}	surface to liquid/vapor saturation temperature drop
ΔT^*	nucleation temperature drop $(4\sigma T_{sat}/\rho_g h_{lg} D_p)$

L_e characteristic length $[(D_p(\mathrm{A}_{c,p}/\mathrm{P}_p)^4)^{0.2}]$

Greek Symbols

δ thickness

ε porosity

μ dynamic viscosity

ρ density

θ contact angle

Φ wedge angle

σ surface tension

$\hat{\sigma}$ accommodation coefficient

υ kinematic viscosity

Subscripts

Cu copper

i interface

l liquid

v vapor

References

[1] S.W. Chi, Heat Pipe Theory and Practice: A Sourcebook, Hemisphere Publishing Corporation, Washington, DC, USA, 1976.

[2] G.P. Peterson, Heat Pipes: Modeling, Testing, and Applications, John Wiley & Sons, New York, NY, USA, 1994.

[3] A. Faghri, Heat Pipe Science and Technology, Taylor & Francis, Washington, DC, USA, 1995.

[4] D. Reay, P. Kew, Heat Pipes: Theory, Design, and Applications, fifth ed., Butterworth-Heinemann, Burlington, MA, USA, 2006.

[5] Y.H. Yau, M. Ahmadzadehtalatapeh, A review on the application of horizontal heat pipe heat exchangers in air conditioning systems in the tropics, Applied Thermal Engineering 30 (2010) 77–84.

[6] H.N. Chaudhry, B.R. Hughes, S.A. Ghani, A review of heat pipe systems for heat recovery and renewable energy applications, Renewable and Sustainable Energy Reviews 16 (2012) 2249–2259.

[7] R. Sureshkumar, S.T. Mohideen, N. Nethaji, Heat transfer characteristics of nanofluids in heat pipes: A review, Renewable and Sustainable Energy Reviews 20 (2013) 397–410.

[8] S.V. Garimella, C.B. Sobhan, Recent advances in the modeling and applications of nonconventional heat pipes, Advances in Heat Transfer, Elsevier, 2001: pp. 249–308.

[9] A. Faghri, Review and advances in heat pipe science and technology, Journal of Heat Transfer 134 (2012) 123001.

[10] S. Launay, V. Sartre, J. Bonjour, Parametric analysis of loop heat pipe operation: a literature review, International Journal of Thermal Sciences, 46 (2007) 621–636.

[11] A. Ambirajan, A.A. Adoni, J.S. Vaidya, A.A. Rajendran, D. Kumar, P. Dutta, Loop heat pipes: a review of fundamentals, operation, and design, Heat Transfer Engineering 33 (2012) 387–405.

[12] C.B. Sobhan, R.L. Rag, G.P. Peterson, A review and comparative study of the investigations on micro heat pipes, International Journal of Energy Research 31 (2007) 664–688.

[13] Y. Zhang, A. Faghri, Advances and unsolved issues in pulsating heat pipes, Heat Transfer Engineering 29 (2008) 20–44.

[14] R.S. Prasher, A simplified conduction based modeling scheme for design sensitivity study of thermal solution utilizing heat pipe and vapor chamber technology, Journal of Electronic Packaging 125 (2003) 378–385.

[15] A. Abhat, R.A. Seban, Boiling and evaporation from heat pipe wicks with water and acetone, Journal of Heat Transfer 96 Ser C (1974) 331–337.

[16] K. Nishikawa, T. Ito, K. Tanaka, Enhanced heat transfer by nucleate boiling on a sintered metal layer, Heat Transfer - Japanese Research 8 (1979) 65–81.

[17] W. Nakayama, T. Daikoku, H. Kuwahara, T. Nakajima, Dynamic model of enhanced boiling heat transfer on porous surfaces - part I: Experimental investigation, Journal of Heat Transfer 102 (1980) 445.

[18] A.E. Bergles, M.C. Chyu, Characteristics of nucleate pool boiling from porous metallic coatings, Journal of Heat Transfer 104 (1982) 279–285.

[19] N.H. Afgan, L.A. Jovic, S.A. Kovalev, V.A. Lenykov, Boiling heat transfer from surfaces with porous layers, International Journal of Heat and Mass Transfer 28 (1985) 415–422.

[20] J.Y. Tsay, Y.Y. Yan, T.F. Lin, Enhancement of pool boiling heat transfer in a horizontal water layer through surface roughness and screen coverage, Heat and Mass Transfer 32 (1996) 17–26.

[21] J.Y. Chang, S.M. You, Enhanced boiling heat transfer from microporous surfaces: effects of a coating composition and method, International Journal of Heat and Mass Transfer 40 (1997) 4449–4460.

[22] J.W. Liu, D.J. Lee, A. Su, Boiling of methanol and HFE-7100 on heated surface covered with a layer of mesh, International Journal of Heat and Mass Transfer 44 (2001) 241–246.

[23] S.G. Liter, M. Kaviany, Pool-boiling CHF enhancement by modulated porous-layer coating: theory and experiment, International Journal of Heat and Mass Transfer 44 (2001) 4287–4311.

[24] K.N. Rainey, S.M. You, S. Lee, Effect of pressure, subcooling, and dissolved gas on pool boiling heat transfer from microporous surfaces in FC-72, Journal of Heat Transfer, 125 (2003) 75–83.

[25] M.S. El-Genk, J.L. Parker, Enhanced boiling of HFE-7100 dielectric liquid on porous graphite, Energy Conversion and Management 46 (2005) 2455–2481.

[26] J.L. Parker, M.S. El-Genk, Effect of surface orientation on nucleate boiling of FC-72 on porous graphite, Journal of Heat Transfer 128 (2006) 1159.

[27] C. Li, G.P. Peterson, Parametric Study of pool boiling on horizontal highly conductive microporous coated surfaces, Journal of Heat Transfer 129 (2007) 1465.

[28] M.E. Poniewski, J.R. Thome, Nucleate Boiling on Micro-structured Surfaces, Lausanne–Warsaw: Heat Transfer Research Inc., College Station, TX, USA, 2008.

[29] A. Brautsch, P.A. Kew, Examination and visualisation of heat transfer processes during evaporation in capillary porous structures, Applied Thermal Engineering 22 (2002) 815–824.

[30] M.A. Hanlon, H.B. Ma, Evaporation heat transfer in sintered porous media, Journal of Heat Transfer 125 (2003) 644–652.

[31] T.W. Davis, S.V. Garimella, Thermal resistance measurement across a wick structure using a novel thermosyphon test chamber, Experimental Heat Transfer 21 (2008) 143–154.

[32] C. Li, G.P. Peterson, Y. Wang, Evaporation/boiling in thin capillary wicks (I) - wick thickness effects, Journal of Heat Transfer 128 (2006) 1312–1319.

[33] C. Li, G.P. Peterson, Evaporation/boiling in thin capillary wicks (II) - effects of volumetric porosity and mesh size, Journal of Heat Transfer 128 (2006) 1320–1328.

[34] M.T. North, J.H. Rosenfeld, R.M. Shaubach, Liquid film evaporation from bidisperse capillary wicks in heat pipe evaporators, in: Proceedings of the 9th International Heat Pipe Conference, 1995, Albuquerque, NM, USA.

[35] T. Semenic, Y.Y. Lin, I. Catton, D.B. Sarraf, Use of biporous wicks to remove high heat fluxes, Applied Thermal Engineering 28 (2008) 278–283.

[36] T. Semenic, I. Catton, Experimental study of biporous wicks for high heat flux applications, International Journal of Heat and Mass Transfer 52 (2009) 5113–5121.

[37] J.A. Weibel, S.V. Garimella, M.T. North, Characterization of evaporation and boiling from sintered powder wicks fed by capillary action, International Journal of Heat and Mass Transfer 53 (2010) 4204–4215.

[38] J.A. Weibel, Characterization of Fluid-Thermal Transport and Boiling in Micro/Nano-Engineered Porous Structures, PhD Thesis, Purdue University, 2012.

[39] Y. Zhao, C.-I. Chen, An investigation of evaporation heat transfer in sintered copper wicks with microgrooves, in: ASME International Mechanical Engineering Congress and Exposition, November 5-10, 2006, Chicago, IL, USA.

[40] G.S. Hwang, Y. Nam, E. Fleming, P. Dussinger, Y.S. Ju, M. Kaviany, Multi-artery heat pipe spreader: Experiment, International Journal of Heat and Mass Transfer 53 (2010) 2662–2669.

[41] G.S. Hwang, E. Fleming, B. Carne, S. Sharratt, Y. Nam, P. Dussinger, *et al.*, Multi-artery heat-pipe spreader: Lateral liquid supply, International Journal of Heat and Mass Transfer 54 (2011) 2334–2340.

[42] Y.S. Ju, M. Kaviany, Y. Nam, S. Sharratt, G.S. Hwang, I. Catton, *et al.*, Planar vapor chamber with hybrid evaporator wicks for the thermal management of high-heat-flux and high-power optoelectronic devices, International Journal of Heat and Mass Transfer 60 (2013) 163–169.

[43] J.A. Weibel, S.V. Garimella, Visualization of vapor formation regimes during capillary-fed boiling in sintered-powder heat pipe wicks, International Journal of Heat and Mass Transfer 55 (2012) 3498–3510.

[44] D. Ćoso, V. Srinivasan, M.-C. Lu, J.-Y. Chang, A. Majumdar, Enhanced heat transfer in biporous wicks in the thin liquid film evaporation and boiling regimes, Journal of Heat Transfer 134 (2012) 101501.

[45] Q. Cai, C.-L. Chen, Design and test of carbon nanotube biwick structure for high-heat-flux phase change heat transfer, Journal of Heat Transfer 132 (2010) 052403.

[46] Q. Cai, A. Bhunia, High heat flux phase change on porous carbon nanotube structures, International Journal of Heat and Mass Transfer 55 (2012) 5544–5551.

[47] Q. Cai, Y.-C. Chen, Investigations of biporous wick structure dryout, Journal of Heat Transfer 134 (2012) 021503.

[48] Y. Nam, S. Sharratt, G. Cha, Y.S. Ju, Characterization and modeling of the heat transfer performance of nanostructured Cu micropost wicks, Journal of Heat Transfer 133 (2011) 101502.

[49] Y. Nam, S. Sharratt, C. Byon, S.-J. Kim, Y.S. Ju, Fabrication and characterization of the capillary performance of superhydrophilic Cu micropost arrays, Journal of Microelectromechanical Systems 19 (2010) 581–588.

[50] J.A. Weibel, A.S. Kousalya, T.S. Fisher, S.V. Garimella, Characterization and nanostructured enhancement of boiling incipience in capillary-fed, ultra-thin sintered powder wicks, in: 13th IEEE Intersociety Conference on Thermal and Thermomechanical Phenomena in Electronic Systems, 2012, San Diego, CA, USA.

[51] A.S. Kousalya, J.A. Weibel, S.V. Garimella, T.S. Fisher, Metal functionalization of carbon nanotubes for enhanced sintered powder wicks, International Journal of Heat and Mass Transfer 59 (2013) 372–383.

[52] M.P. Mughal, O.A. Plumb, An experimental study of boiling on a wicked surface, International Journal of Heat and Mass Transfer 39 (1996) 771–777.

[53] R.R. Williams, D.K. Harris, A device and technique to measure the heat transfer limit of a planar heat pipe wick, Experimental Thermal and Fluid Science 30 (2006) 277–284.

[54] B.D. Iverson, T.W. Davis, S.V. Garimella, M.T. North, S.S. Kang, Heat and mass transport in heat pipe wick structures, Journal of Thermophysics and Heat Transfer 21 (2007) 392–404.

[55] S.-C. Wong, Y.-H. Kao, Visualization and performance measurement of operating mesh-wicked heat pipes, International Journal of Heat and Mass Transfer 51 (2008) 4249–4259.

[56] J.-H. Liou, C.-W. Chang, C. Chao, S.-C. Wong, Visualization and thermal resistance measurement for the sintered mesh-wick evaporator in operating flat-plate heat pipes, International Journal of Heat and Mass Transfer 53 (2010) 1498–506.

[57] S.-C. Wong, J.-H. Liou, C.-W. Chang, Evaporation resistance measurement with visualization for sintered copper-powder evaporator in operating flat-plate heat pipes, International Journal of Heat and Mass Transfer 53 (2010) 3792–8.

[58] C. Li, G.P. Peterson, J. Li, N. Koratkar, The visualization of thin film evaporation on thin micro sintered copper mesh screen, in: ASME Summer Heat Transfer Conference, August 10-14, 2008, Jacksonville, FL, USA.

[59] V.P. Carey, Liquid-Vapor Phase-Change Phenomena, Taylor & Francis, 1992.

[60] L.-H. Chien, C.-C. Chang, Experimental study of evaporation resistance on porous surfaces in flat heat pipes, in: 8th IEEE Intersociety Conference on Thermal and Thermomechanical Phenomena in Electronic Systems, 2002, San Diego, CA, USA.

[61] R.L. Webb, Nucleate boiling on porous coated surfaces, Heat Transfer Engineering 4 (1981) 71–82.

[62] X.L. Cao, P. Cheng, T.S. Zhao, Experimental study of evaporative heat transfer in sintered copper bidispersed wick structures, Journal of Thermophysics and Heat Transfer 16 (2002) 547–552.

[63] S.W. Reilly, I. Catton, Utilization of advanced working fluids with biporous evaporators, Journal of Thermal Science and Engineering Applications 3 (2011) 021006.

[64] T. Semenic, Y.-Y. Lin, I. Catton, Thermophysical properties of biporous heat pipe evaporators, Journal of Heat Transfer 130 (2008) 022602.

[65] J. Wang, I. Catton, Evaporation heat transfer in thin biporous media, Heat and Mass Transfer 37 (2001) 275–281.

[66] E.G. Merilo, Experimental investigation of boiling heat transfer in bidispersed porous media, Master's Thesis, University of California, Los Angeles, CA, USA, 2002.

[67] D.H. Min, G.S. Hwang, M. Kaviany, Multi-artery, heat-pipe spreader, International Journal of Heat and Mass Transfer. 52 (2009) 629–635.

[68] W.M. Rohsenow, Method of correlating heat-transfer data for surface boiling of liquids, American Society of Mechanical Engineers - Transactions 74 (1952) 969–975.

[69] I.L. Mostinski, Application of the rule of corresponding states for calculation of heat transfer and critical heat flux, Teploenergetika 4 (1963).

[70] M.G. Cooper, Saturation nucleate pool boiling - a simple correlation, in: Institution of Chemical Engineers Symposium Series, 1984, Leeds, England, pp. 785–793.

[71] D. Gorenflo, Pool Boiling, VDI-Verlag GmbH, Dusseldorf, 1993.

[72] R.L. Webb, Nucleate boiling on porous coated surfaces, Heat Transfer Engineering. 4 (1981) 71–82.

[73] S. Madhusudana Rao, A.R. Balakrishnan, Analysis of pool boiling heat transfer over porous surfaces, Heat and Mass Transfer 32 (1997) 463–469.

[74] G.F. Smirnov, Approximate theory of heat transfer with boiling on surfaces covered with capillary-porous structures, Thermal Engineering (Teploenergetika) 24 (1977) 55–58.

[75] B.A. Afanas'ev, G.F. Smirnov, Investigation of heat transfer and of maximum heat fluxes with boiling in capillary-porous structures, Thermal Engineering 26 (1979) 311–313.

[76] B.A. Afanas'yev, V.V. Zrodnikov, A.L. Koba, T.F. Smirnov, A.K. Pimenov, Boiling heat transfer in slots, capillaries and in capillary-porous (wick) structures, Heat Transfer - Soviet Research 12 (1980) 70–78.

[77] S.M. You, A. Bar-Cohen, T.W. Simon, Boiling incipience and nucleate boiling heat transfer of highly wetting dielectric fluids from electronic materials, IEEE Transactions on Components, Hybrids, and Manufacturing Technology 13 (1990) 1032–1039.

[78] B.J. Jones, J.P. McHale, S.V. Garimella, The influence of surface roughness on nucleate pool boiling heat transfer, Journal of Heat Transfer 131 (2009) 1–14.

[79] S.J. Reed, I. Mudawar, Elimination of boiling incipience temperature drop in highly wetting fluids using spherical contact with a flat surface, International Journal of Heat and Mass Transfer 42 (1999) 2439–2454.

[80] J.P. McHale, S.V. Garimella, T.S. Fisher, G.A. Powell, Pool boiling performance comparison of smooth and sintered copper surfaces with and without carbon nanotubes, Nanoscale and Microscale Thermophysical Engineering 15 (2011) 133–150.

[81] D.H. Altman, J.R. Wasniewski, M.T. North, S.S. Kim, T.S. Fisher, Development of micro/nano engineered wick-based passive heat spreaders for thermal management of high power electronic devices, in: ASME InterPACK, Portland, OR, USA, 2011, 52122.

[82] P.J. Marto, V.J. Lepere, Pool boiling heat transfer from enhanced surfaces to dielectric fluids, Journal of Heat Transfer 104 (1982) 292–299.

[83] S.M. You, T.W. Simon, A. Bar-Cohen, W. Tong, Experimental investigation of nucleate boiling incipience with a highly-wetting dielectric fluid (R-113), International Journal of Heat and Mass Transfer 33 (1990) 105–117.

[84] Y.Y. Hsu, On the size range of active nucleation cavities on a heating surface, Journal of Heat Transfer 84 (1962) 207–213.

[85] J.H. Lienhard, V.K. Dhir, D.M. Riherd, Peak pool boiling heat-flux measurements on finite horizontal flat plates, Journal of Heat Transfer 95 (1973) 477–482.

[86] I.I. Gogonin, S.S. Kutateladze, Critical heat flux as a function of heater size for a liquid boiling in a large enclosure, Journal of Engineering Physics 33 (1977) 1286–1289.

[87] K.-A. Park, A.E. Bergles, Effects of size of simulated microelectronic chips on boiling and critical heat flux, Journal of Heat Transfer 110 (1988) 728.

[88] S.H. Yang, W.-P. Baek, S.H. Chang, Pool-boiling critical heat flux of water on small plates: Effects of surface orientation and size, International Communications in Heat and Mass Transfer 24 (1997) 1093–1102.

[89] T. Chen, J.N. Chung, An experimental study of miniature-scale pool boiling, Journal of Heat Transfer 125 (2003) 1074–1086.

[90] M. Kaviany, Principles of Heat Transfer in Porous Media, 2nd ed., Springer, 1995.

[91] D.E. Sweeney, Correlation for pressure drop in two-phase cocurrent flow in packed beds, AlChE Journal 13 (1967) 663–669.

[92] V.X. Tung, V.K. Dhir, Hydrodynamic model for two-phase flow through porous media, International Journal of Multiphase Flow 14 (1988) 47–65.

[93] T. Murugesan, V. Sivakumar, Pressure drop and flow regimes in cocurrent gas-liquid upflow through packed beds, Chemical Engineering Journal 88 (2002) 233–43.

[94] H. Muller-Steinhagen, M. Jamialahmadi, M.R. Izadpanah, Pressure drop, gas hold-up and heat transfer during single and two-phase flow through porous media, International Journal of Heat and Fluid Flow 26 (2005) 156–72.

[95] I. Sauciuc, G. Chrysler, R. Mahajan, R. Prasher, Spreading in the heat sink base: phase change systems or solid metals??, IEEE Transactions on Components and Packaging Technologies 25 (2002) 621 – 628.

[96] S.-S. Hsieh, R.-Y. Lee, J.-C. Shyu, S.-W. Chen, Analytical solution of thermal resistance of vapor chamber heat sink with and without pillar, Energy Conversion and Management 48 (2007) 2708–2717.

[97] Z.J. Zuo, A. Faghri, A network thermodynamic analysis of the heat pipe, International Journal of Heat and Mass Transfer 41 (1998) 1473–1484.

[98] Y. Cao, A. Faghri, Transient two-dimensional compressible analysis for high-temperature heat pipes with pulsed heat input, Numerical Heat Transfer, Part A: Applications 18 (1991) 483–502.

[99] J.-Y. Chang, R.S. Prasher, S. Prstic, P. Cheng, H.B. Ma, Evaporative thermal performance of vapor chambers under nonuniform heating conditions, Journal Heat Transfer 130 (2008) 121501–121501.

[100] K. Vafai, W. Wang, Analysis of flow and heat transfer characteristics of an asymmetrical flat plate heat pipe, International Journal of Heat and Mass Transfer 35 (1992) 2087–2099.

[101] N. Zhu, K. Vafai, Analytical modeling of the startup characteristics of asymmetrical flat-plate and disk-shaped heat pipes, International Journal of Heat and Mass Transfer 41 (1998) 2619–2637.

[102] Y. Wang, K. Vafai, Transient characterization of flat plate heat pipes during startup and shutdown operations, International Journal of Heat and Mass Transfer 43 (2000) 2641–2655.

[103] Y. Wang, K. Vafai, An experimental investigation of the thermal performance of an asymmetrical flat plate heat pipe, International Journal of Heat and Mass Transfer 43 (2000) 2657–2668.

[104] Y. Wang, K. Vafai, An experimental investigation of the transient characteristics on a flat-plate heat pipe during startup and shutdown operations, Journal of Heat Transfer 122 (2000) 525–535.

[105] F. Lefèvre, M. Lallemand, Coupled thermal and hydrodynamic models of flat micro heat pipes for the cooling of multiple electronic components, International Journal of Heat and Mass Transfer 49 (2006) 1375–1383.

[106] M. Aghvami, A. Faghri, Analysis of flat heat pipes with various heating and cooling configurations, Applied Thermal Engineering 31 (2011) 2645–2655.

[107] N. Zhu, K. Vafai, Vapor and liquid flow in an asymmetrical flat plate heat pipe: a three-dimensional analytical and numerical investigation, International Journal of Heat and Mass Transfer 41 (1998) 159–174.

[108] R. Sonan, S. Harmand, J. Pellé, D. Leger, M. Fakès, Transient thermal and hydrodynamic model of flat heat pipe for the cooling of electronics components, International Journal of Heat and Mass Transfer 51 (2008) 6006–6017.

[109] U. Vadakkan, S.V. Garimella, J.Y. Murthy, Transport in flat heat pipes at high heat fluxes from multiple discrete sources, Journal of Heat Transfer 126 (2004) 347–354.

[110] G. Carbajal, C.B. Sobhan, G.P. Peterson, D.T. Queheillalt, H.N.G. Wadley, Thermal response of a flat heat pipe sandwich structure to a localized heat flux, International Journal of Heat and Mass Transfer 49 (2006) 4070–4081.

[111] Y.-S. Chen, K.-H. Chien, C.-C. Wang, T.-C. Hung, B.-S. Pei, A simplified transient three-dimensional model for estimating the thermal performance of the vapor chambers, Applied Thermal Engineering 26 (2006) 2087–2094.

[112] Y.-S. Chen, K.-H. Chien, T.-C. Hung, C.-C. Wang, Y.-M. Ferng, B.-S. Pei, Numerical simulation of a heat sink embedded with a vapor chamber and calculation of effective thermal conductivity of a vapor chamber, Applied Thermal Engineering 29 (2009) 2655–2664.

[113] Y. Koito, H. Imura, M. Mochizuki, Y. Saito, S. Torii, Numerical analysis and experimental verification on thermal fluid phenomena in a vapor chamber, Applied Thermal Engineering 26 (2006) 1669–1676.

[114] B. Xiao, A. Faghri, A three-dimensional thermal-fluid analysis of flat heat pipes, International Journal of Heat and Mass Transfer 51 (2008) 3113–3126.

[115] J.-M. Tournier, M.S. El-Genk, Heat pipe transient analysis model, International Journal of Heat and Mass Transfer 37 (1994) 753–762.

[116] J.A. Rice, A. Faghri, Analysis of screen wick heat pipes, including capillary dry-out limitations, Journal of Thermophysics and Heat Transfer 21 (2007) 475–486.

[117] K. Vafai, Handbook of Porous Media, Second Edition, CRC Press, Boca Raton, FL, USA, 2005.

[118] R.L. Gorring, S.W. Churchill, Thermal conductivity of heterogeneous materials, Chemical Engineering Progress 57 (1961) 53–59.

[119] J.C. Maxwell, A Treatise on Electricity and Magnetism, Vol. 1, 3rd ed., Dover Publications, 1954.

[120] R.W. Schrage, A Theoretical Study of Interface Mass Transfer, Columbia University Press, New York, NY, USA 1953.

[121] M. Potash Jr., P. Wayner Jr., Evaporation from a two-dimensional extended meniscus, International Journal of Heat and Mass Transfer 15 (1972) 1851–1863.

[122] H. Wang, S.V. Garimella, J.Y. Murthy, Characteristics of an evaporating thin film in a microchannel, International Journal of Heat and Mass Transfer 50 (2007) 3933–3942.

[123] G.P. Peterson, L.S. Fletcher, Effective thermal conductivity of sintered heat pipe wicks, Journal of Thermophysics 1 (1986) 343–347.

[124] N. Atabaki, B.R. Baliga, Effective thermal conductivity of water-saturated sintered powder-metal plates, Heat and Mass Transfer 44 (2007) 85–99.

[125] Y.-Y. Lin, T. Semenic, I. Catton, Thermophysical properties of monoporous sintered copper, in: ASME Summer Heat Transfer Conference, San Francisco, CA, USA, 2005, pp. 17–23.

[126] S. Kirkpatrick, Percolation and Conduction, Reviews of Modern Physics 45 (1973) 574–588.

[127] J.K. Carson, S.J. Lovatt, D.J. Tanner, A.C. Cleland, Thermal conductivity bounds for isotropic, porous materials, International Journal of Heat and Mass Transfer 48 (2005) 2150–2158.

[128] C. Li, G.P. Peterson, The effective thermal conductivity of wire screen, International Journal of Heat and Mass Transfer 49 (2006) 4095–4105.

[129] Z. Zhao, Y. Peles, M.K. Jensen, Properties of plain weave metallic wire mesh screens, International Journal of Heat and Mass Transfer 57 (2013) 690–697.

[130] J. Xu, R.A. Wirtz, In-plane effective thermal conductivity of plain-weave screen laminates, IEEE Transactions on Components and Packaging Technologies 25 (2002) 615–620.

[131] H. Kozai, H. Imura, Y. Ikeda, Permeability of screen wicks, JSME International Journal, Series 2: Fluids Engineering, Heat Transfer, Power, Combustion, Thermophysical Properties 34 (1991) 212–219.

[132] D.R. Adkins, R.C. Dykhuizen, Procedures for measuring the properties of heat-pipe wick materials, in: ACS Proceedings of the 28th Intersociety Energy Conversion Engineering Conference, Washington, DC, USA, 1993, pp. 911–18.

[133] R.R. Williams, D.K. Harris, Cross-plane and in-plane porous properties measurements of thin metal felts: applications in heat pipes, Experimental Thermal and Fluid Science 27 (2003) 227–235.

[134] H. Noda, K. Yoshioka, T. Hamatake, Experimental study on the permeability of screen wicks, JSME International Journal, Series B: Fluids and Thermal Engineering 36 (1993) 357–363.

[135] D. Deng, Y. Tang, G. Huang, L. Lu, D. Yuan, Characterization of capillary performance of composite wicks for two-phase heat transfer devices, International Journal of Heat and Mass Transfer 56 (2013) 283–293.

[136] H.P.J. de Bock, K. Varanasi, P. Chamarthy, T. Deng, A. Kulkarni, B.M. Rush, et al., Experimental investigation of micro/nano heat pipe wick structures, in: ASME International Mechanical Engineering Congress and Exposition, 2008, Boston, MA, USA, pp. 991–996.

[137] H. Imura, H. Kozai, Y. Ikeda, Effective pore radius of screen wicks, Heat Transfer Engineering 15 (1994) 24–32.

[138] E.W. Washburn, The dynamics of capillary flow, Physical Review 17 (1921) 273–283.

[139] B. Holley, A. Faghri, Permeability and effective pore radius measurements for heat pipe and fuel cell applications, Applied Thermal Engineering 26 (2006) 448–462.

[140] P. Chamarthy, H.P.J. de Bock, B. Russ, S. Chauhan, B. Rush, S.E. Weaver, *et al.*, Novel fluorescent visualization method to characterize transport properties in micro/nano heat pipe wick structures, in: ASME International Technical Conference and Exhibition on Packaging and Integration of Electronic and Photonic Microsystems, San Francisco, CA, USA, 2009, pp. 419–25.

[141] C. Byon, S.J. Kim, Capillary performance of bi-porous sintered metal wicks, International Journal of Heat and Mass Transfer 55 (2012) 4096–4103.

[142] M.R.S. Shirazy, L.G. Fréchette, Capillary and wetting properties of copper metal foams in the presence of evaporation and sintered walls, International Journal of Heat and Mass Transfer 58 (2013) 282–291.

[143] R. Xiao, R. Enright, E.N. Wang, Prediction and optimization of liquid propagation in micropillar arrays, Langmuir 26 (2010) 15070–15075.

[144] H.K. Dhavaleswarapu, P. Chamarthy, S.V. Garimella, J.Y. Murthy, Experimental investigation of steady buoyant-thermocapillary convection near an evaporating meniscus, Physics of Fluids 19 (2007).

[145] H. Wang, S.V. Garimella, J.Y. Murthy, An analytical solution for the total heat transfer in the thin-film region of an evaporating meniscus, International Journal of Heat and Mass Transfer 51 (2008) 6317–6322.

[146] H.K. Dhavaleswarapu, S.V. Garimella, J.Y. Murthy, Microscale temperature measurements near the triple line of an evaporating thin liquid film, Journal of Heat Transfer 131 (2009) 1–7.

[147] H.K. Dhavaleswarapu, J.Y. Murthy, S.V. Garimella, Numerical investigation of an evaporating meniscus in a channel, International Journal of Heat and Mass Transfer 55 (2012) 915–924.

[148] C.P. Migliaccio, H.K. Dhavaleswarapu, S.V. Garimella, Temperature measurements near the contact line of an evaporating meniscus V-groove, International Journal of Heat and Mass Transfer 54 (2011) 1520–1526.

[149] H. Wang, Z. Pan, S.V. Garimella, Numerical investigation of heat and mass transfer from an evaporating meniscus in a heated open groove, International Journal of Heat and Mass Transfer 54 (2011) 3015–3023.

[150] C.P. Migliaccio, S.V. Garimella, Evaporative heat and mass transfer from the free surface of a liquid wicked into a bed of spheres, International Journal of Heat and Mass Transfer 54 (2011) 3440–3447.

[151] K.K. Bodla, J.A. Weibel, S.V. Garimella, Advances in fluid and thermal transport property analysis and design of sintered porous wick microstructures, Journal of Heat Transfer (In Press).

[152] K.K. Bodla, J.Y. Murthy, S.V. Garimella, Direct simulation of thermal transport through sintered wick microstructures, Journal of Heat Transfer 134 (2011) 012602.

[153] R. Ranjan, J.Y. Murthy, S.V. Garimella, Analysis of the wicking and thin-film evaporation characteristics of microstructures, Journal of Heat Transfer 131 (2009) 1–11.

[154] K.A. Brakke, The surface evolver, Experimental Mathematics 1 (1992) 141–165.

[155] R. Ranjan, J.Y. Murthy, S.V. Garimella, A microscale model for thin-film evaporation in capillary wick structures, International Journal of Heat and Mass Transfer 54 (2011) 169–179.

[156] N.S. Dhillon, J.C. Cheng, A.P. Pisano, Heat transfer due to microscale thin film evaporation from the steady state meniscus in a coherent porous silicon based micro-columnated wicking structure, in: ASME International Mechanical Engineering Congress and Exposition, 2011, Denver, CO, USA.

[157] K.K. Bodla, J.Y. Murthy, S.V. Garimella, Evaporation analysis in sintered wick microstructures, International Journal of Heat and Mass Transfer 61 (2013) 729–741.

[158] R. Ranjan, A. Patel, S.V. Garimella, J.Y. Murthy, Wicking and thermal characteristics of micropillared structures for use in passive heat spreaders, International Journal of Heat and Mass Transfer 55 (2012) 586–596.

[159] S. Sharratt, C. Peng, Y.S. Ju, Micro-post evaporator wicks with improved phase change heat transfer performance, International Journal of Heat and Mass Transfer 55 (2012) 6163–6169.

[160] R. Ranjan, J.Y. Murthy, S.V. Garimella, U. Vadakkan, A numerical model for transport in flat heat pipes considering wick microstructure effects, International Journal of Heat and Mass Transfer 54 (2011) 153–168.

[161] V.K. Dhir, Mechanistic prediction of nucleate boiling heat transfer–achievable or a hopeless task?, Journal of Heat Transfer 128 (2006) 1.

[162] G. Son, V.K. Dhir, N. Ramanujapu, Dynamics and heat transfer associated with a single bubble during nucleate boiling on a horizontal surface, Journal of Heat Transfer 121 (1999) 623–631.

[163] G. Son, N. Ramanujapu, V.K. Dhir, Numerical simulation of bubble merger process on a single nucleation site during pool nucleate boiling, Journal of Heat Transfer 124 (2001) 51–62.

[164] D. Gerlach, G. Tomar, G. Biswas, F. Durst, Comparison of volume-of-fluid methods for surface tension-dominant two-phase flows, International Journal of Heat and Mass Transfer 49 (2006) 740–754.

[165] A. Mukherjee, S.G. Kandlikar, Numerical study of single bubbles with dynamic contact angle during nucleate pool boiling, International Journal of Heat and Mass Transfer 50 (2007) 127–138.

[166] C. Kunkelmann, P. Stephan, CFD simulation of boiling flows using the volume-of-fluid method within OpenFOAM, Numerical Heat Transfer, Part A: Applications 56 (2009) 631–646.

[167] C. Kunkelmann, P. Stephan, Numerical simulation of the transient heat transfer during nucleate boiling of refrigerant HFE-7100, International Journal of Refrigeration 33 (2010) 1221–1228.

[168] W. Lee, G. Son, J.J. Jeong, Numerical analysis of bubble growth and departure from a microcavity, Numerical Heat Transfer, Part B: Fundamentals 58 (2010) 323–342.

[169] B.A. Nichita, I. Zun, J.R. Thome, A level set method coupled with a volume of fluid method for modeling of gas-liquid interface in bubbly flow, Journal of Fluids Engineering 132 (2010) 081302.

[170] R. Ranjan, J.Y. Murthy, S.V. Garimella, Bubble dynamics during capillary-fed nucleate boiling in porous media, in: 13th IEEE Intersociety Conference on Thermal and Thermomechanical Phenomena in Electronic Systems, 2012, San Diego, CA, USA, pp. 1114-1126.

[171] C.H. Li, T. Li, P. Hodgins, G.P. Peterson, Characteristics of pool boiling bubble dynamics in bead packed porous structures, Journal of Heat Transfer 133 (2011) 031004.

[172] A. Mukherjee, V.K. Dhir, Study of lateral merger of vapor bubbles during nucleate pool boiling, Journal of Heat Transfer 126 (2005) 1023–1039.

[173] R. Ranjan, J.Y. Murthy, S.V. Garimella, D.H. Altman, M.T. North, Modeling and design optimization of ultrathin vapor chambers for high heat flux applications, IEEE Transactions on Components, Packaging and Manufacturing Technology 2 (2012) 1465–1479.

[174] D.H. Altman, J.A. Weibel, S.V. Garimella, T.S. Fisher, J.H. Nadler, M. North, Thermal ground plane vapor chamber heat spreaders for high power packaging density electronic systems, Electronics Cooling (2012) 20–27.

[175] H.P.J. de Bock, S. Chauhan, P. Chamarthy, S.E. Weaver, T. Deng, F.M. Gerner, et al., On the charging and thermal characterization of a micro/nano structured thermal ground plane, in: 12th IEEE Intersociety Conference on Thermal and Thermomechanical Phenomena in Electronic Systems, 2010, Las Vegas, NV, USA.

[176] H.P.J. de Bock, S. Chauhan, P. Chamarthy, C. Eastman, S. Weaver, B.P. Whalen, et al., Development and experimental validation of a micro/nano thermal ground plane, in: Proceedings of the ASME/JSME 8th Thermal Engineering Joint Conference, 2011, Honolulu, HI, USA.

[177] S.W. Reilly, I. Catton, Characterization of vapor escape restriction in biporous wicks with monolayers for thermal ground plane optimization, in: Proceedings of the ASME International Mechanical Engineering Congress & Exposition, November 13-19, 2009, Lake Buena Vista, FL, USA.

[178] S.W. Reilly, L. Amouzegar, I. Catton, Comparison of vacuum chamber tested biporous wicks with thermal ground plane testing, in: Proceeding of the ASME International Heat Transfer Conference, August 8-13, 2010, Washington, DC, USA.

[179] I. Catton, S. Reilly, L. Amouzegar, Advances in biporous wick design and testing for thermal ground planes, Frontiers in Heat Pipes 1 (2010) 013001.

[180] X. Dai, L. Tran, F. Yang, B. Shi, R. Yang, Y.C. Lee, et al., Characterization of hybrid-wicked copper heat pipe, in: Proceedings of the ASME/JSME 8th Thermal Engineering Joint Conference, 2011, Honolulu, HI, USA.

[181] C. Oshman, B. Shi, C. Li, R. Yang, Y.C. Lee, G.P. Peterson, et al., The development of polymer-based flat heat pipes, Journal of Microelectromechanical Systems 20 (2011) 410–417.

[182] C. Oshman, Q. Li, L.-A. Liew, R. Yang, Y.C. Lee, V.M. Bright, Flat polymer heat spreader with high aspect ratio micro hybrid wick operating under adverse gravity, Proceedings of the ASME International Mechanical Engineering Congress and Exposition, 2011, Denver, CO, USA.

[183] G.P. Peterson, A.B. Duncan, M.H. Weichold, Experimental investigation of micro heat pipes fabricated in silicon wafers, Journal of Heat Transfer 115 (1993) 751–756.

[184] M.L. Berre, S. Launay, V. Sartre, M. Lallemand, Fabrication and experimental investigation of silicon micro heat pipes for cooling electronics, Journal of Micromechanics and Microengineering 13 (2003) 436.

[185] S. Launay, V. Sartre, M. Lallemand, Experimental study on silicon micro-heat pipe arrays, Applied Thermal Engineering 24 (2004) 233–243.

[186] C. Gillot, Y. Avenas, N. Cezac, G. Poupon, C. Schaeffer, E. Fournier, Silicon heat pipes used as thermal spreaders, IEEE Transactions on Components and Packaging Technologies 26 (2003) 332–339.

[187] Q. Cai, B.-C. Chen, C. Tsai, C. Chen, Development of scalable silicon heat spreader for high power electronic devices, Journal of Thermal Science and Engineering Applications 1 (2010) 041009.

[188] Q. Cai, B.-C. Chen, C. Tsai, Design, development and tests of high-performance silicon vapor chamber, Journal of Micromechanics and Microengineering 22 (2012) 035009.

[189] C. Ding, G. Soni, P. Bozorgi, B.D. Piorek, C.D. Meinhart, N.C. MacDonald, A flat heat pipe architecture based on nanostructured titania, Journal of Microelectromechanical Systems 19 (2010) 878–884.

[190] M. Sigurdson, Y. Liu, P. Bozorgi, D. Bothman, N. MacDonald, C. Meinhart, A large scale titanium thermal ground plane, International Journal of Heat and Mass Transfer 62 (2013) 178–183.

[191] M.F. Aimi, M.P. Rao, N.C. MacDonald, A.S. Zuruzi, D.P. Bothman, High-aspect-ratio bulk micromachining of titanium, Nature Materials 3 (2004) 103–105.

[192] N. Srivastava, C. Din, A. Judson, N.C. MacDonald, C.D. Meinhart, A unified scaling model for flow through a lattice of microfabricated posts, Lab on a Chip 10 (2010) 1148–1152.

[193] S. Berber, Y.-K. Kwon, D. Tomanek, Unusually high thermal conductivity of carbon nanotubes, Physical Review Letters 84 (2000) 4613–4616.

[194] J. Che, T. Cagin, W.A. Goddard III, Thermal conductivity of carbon nanotubes, Nanotechnology 11 (2000) 65–69.

[195] P. Kim, L. Shi, A. Majumdar, P.L. McEuen, Thermal transport measurements of individual multiwalled nanotubes, Physical Review Letters 87 (2001) 215502 1–4.

[196] A.E. Aliev, M.H. Lima, E.M. Silverman, R.H. Baughman, Thermal conductivity of multi-walled carbon nanotube sheets: radiation losses and quenching of phonon modes, Nanotechnology 21 (2010) 035709 1–11.

[197] E. Pop, D. Mann, Q. Wang, K. Goodson, H. Dai, Thermal conductance of an individual single-wall carbon nanotube above room temperature, Nano Letters 6 (2006) 96–100.

[198] M.S. Dresselhaus, P.C. Eklund, Phonons in carbon nanotubes, Advances in Physics 49 (2000) 705–814.

[199] P.B. Amama, B.A. Cola, T.D. Sands, X. Xu, T.S. Fisher, Dendrimer-assisted controlled growth of carbon nanotubes for enhanced thermal interface conductance, Nanotechnology 18 (2007).

[200] B.A. Cola, J. Xu, C. Cheng, X. Xu, T.S. Fisher, H. Hu, Photoacoustic characterization of carbon nanotube array thermal interfaces, Journal of Applied Physics 101 (2007) 054313–054313–9.

[201] H. Wang, J. Feng, X. Hu, K.M. Ng, Synthesis of aligned carbon nanotubes on double-sided metallic substrate by chemical vapor deposition, The Journal of Physical Chemistry C 111 (2007) 12617–12624.

[202] Q. Ngo, B.A. Cruden, A.M. Cassell, G. Sims, M. Meyyappan, J. Li, et al., Thermal interface properties of Cu-filled vertically aligned carbon nanofiber arrays, Nano Letters 4 (2004) 2403–2407.

[203] M.J. Biercuk, M.C. Llaguno, M. Radosavljevic, J.K. Hyun, A.T. Johnson, J.E. Fischer, Carbon nanotube composites for thermal management, Applied Physics Letters 80 (2002) 2767–2769.

[204] C.H. Liu, H. Huang, Y. Wu, S.S. Fan, Thermal conductivity improvement of silicone elastomer with carbon nanotube loading, Applied Physics Letters 84 (2004) 4248–4250.

[205] Y. Gogotsi, J.A. Libera, A. Güvenç-Yazicioglu, C.M. Megaridis, In situ multiphase fluid experiments in hydrothermal carbon nanotubes, Applied Physics Letters 79 (2001) 1021–1023.

[206] J.-G. Fan, D. Dyer, G. Zhang, Y.-P. Zhao, Nanocarpet effect: Pattern formation during the wetting of vertically aligned nanorod arrays, Nano Letters 4 (2004) 2133–2138.

[207] L. Feng, S. Li, Y. Li, H. Li, L. Zhang, J. Zhai, et al., Super-hydrophobic surfaces: from natural to artificial, Advanced Materials 14 (2002) 1857–1860.

[208] J.J. Zhou, F. Noca, M. Gharib, Flow conveying and diagnosis with carbon nanotube arrays, Nanotechnology 17 (2006) 4845–4853.

[209] Q. Cai, C.-L. Chen, Design and test of carbon nanotube biwick structure for high-heat-flux phase change heat transfer, Journal of Heat Transfer 132 (2010) 1–8.

[210] A.S. Kousalya, C.N. Hunter, S.A. Putnam, T. Miller, T.S. Fisher, Photonically enhanced flow boiling in a channel coated with carbon nanotubes, Applied Physics Letters 100 (2012) 071601–071601–4.

[211] H.S. Ahn, N. Sinha, M. Zhang, D. Banerjee, S. Fang, R.H. Baughman, Pool boiling experiments on multiwalled carbon nanotube (MWCNT) forests, Journal of Heat Transfer 128 (2006) 1335–1342.

[212] S. Launay, A.G. Fedorov, Y. Joshi, A. Cao, P.M. Ajayan, Hybrid micro-nano structured thermal interfaces for pool boiling heat transfer enhancement, Microelectronics Journal 37 (2006) 1158–1164.

[213] S. Ujereh, T. Fisher, I. Mudawar, Effects of carbon nanotube arrays on nucleate pool boiling, International Journal of Heat and Mass Transfer 50 (2007) 4023–4038.

[214] C. Li, Z. Wang, P.-I. Wang, Y. Peles, N. Koratkar, G.P. Peterson, Nanostructured copper interfaces for enhanced boiling, Small 4 (2008) 1084–1088.

[215] R. Chen, M.-C. Lu, V. Srinivasan, Z. Wang, H.H. Cho, A. Majumdar, Nanowires for enhanced boiling heat transfer, Nano Letters 9 (2009) 548–553.

[216] Z. Yao, Y.-W. Lu, S.G. Kandlikar, Effects of nanowire height on pool boiling performance of water on silicon chips, International Journal of Thermal Sciences 50 (2011) 2084–2090.

[217] M.-C. Lu, R. Chen, V. Srinivasan, V.P. Carey, A. Majumdar, Critical heat flux of pool boiling on Si nanowire array-coated surfaces, International Journal of Heat and Mass Transfer 54 (2011) 5359–5367.

[218] R. Ranjan, S.V. Garimella, J.Y. Murthy, K. Yazawa, Assessment of nanostructured capillary wicks for passive two-phase heat transport, Nanoscale and Microscale Thermophysical Engineering 15 (2011) 179–194.

[219] M.P. Rossi, H. Ye, Y. Gogotsi, S. Babu, P. Ndungu, J.-C. Bradley, Environmental scanning electron microscopy study of water in carbon nanopipes, Nano Letters 4 (2004) 989–993.

[220] B.M. Kim, S. Sinha, H.H. Bau, Optical microscope study of liquid transport in carbon nanotubes, Nano Letters 4 (2004) 2203–2208.

[221] C. Fradin, A. Braslau, D. Luzet, D. Smilgies, M. Alba, N. Boudet, et al., Reduction in the surface energy of liquid interfaces at short length scales, Nature 403 (2000) 871–874.

[222] J.H. Walther, T. Werder, R.L. Jaffe, P. Koumoutsakos, Hydrodynamic properties of carbon nanotubes, Physical Review E - Statistical, Nonlinear, and Soft Matter Physics 69 (2004) 062201.

[223] Z.P. Huang, J.W. Xu, Z.F. Ren, J.H. Wang, M.P. Siegal, P.N. Provencio, Growth of highly oriented carbon nanotubes by plasma-enhanced hot filament chemical vapor deposition, Applied Physics Letters 73 (1998) 3845–3847.

[224] J. Li, C. Papadopoulos, J.M. Xu, M. Moskovits, Highly-ordered carbon nanotube arrays for electronics applications, Applied Physics Letters 75 (1999) 367–369.

[225] Y. Tu, Z.P. Huang, D.Z. Wang, J.G. Wen, Z.F. Ren, Growth of aligned carbon nanotubes with controlled site density, Applied Physics Letters 80 (2002) 4018–4020.

[226] J.A. Weibel, S.V. Garimella, J.Y. Murthy, D.H. Altman, Design of integrated nanostructured wicks for high-performance vapor chambers, IEEE Transactions on Components, Packaging and Manufacturing Technology 1 (2011) 859–867.

[227] J.A. Weibel, S.S. Kim, T.S. Fisher, S.V. Garimella, Carbon nanotube coatings for enhanced capillary-fed boiling from porous microstructures, Nanoscale and Microscale Thermophysical Engineering 16 (2012) 1–17.

[228] R.K. Garg, S.S. Kim, D.B. Hash, J.P. Gore, T.S. Fisher, Effects of feed gas composition and catalyst thickness on carbon nanotube and nanofiber synthesis by plasma enhanced chemical vapor deposition, Journal of Nanoscience and Nanotechnology 8 (2008) 3068–3076.

[229] N. Singh, V. Sathyamurthy, W. Peterson, J. Arendt, D. Banerjee, Flow boiling enhancement on a horizontal heater using carbon nanotube coatings, International Journal of Heat and Fluid Flow 31 (2010) 201–207.